GEOMATERIALS SUBJECTED TO REPETITIVE LOADING:

IMPLICATIONS ON ENERGY SYSTEMS

A Thesis
Presented to
The Academic Faculty

by

Cesar Pasten

In Partial Fulfillment
of the Requirements for the Degree
Doctor of Philosophy in the
School of Civil and Environmental Engineering

Georgia Institute of Technology
May 2013

GEOMATERIALS SUBJECTED TO REPETITIVE LOADING:

IMPLICATIONS ON ENERGY SYSTEMS

Approved by:

Dr. J. Carlos Santamarina, Advisor
School of Civil and Environmental Engineering
Georgia Institute of Technology

Dr. Dominic Assimaki
School of Civil and Environmental Engineering
Georgia Institute of Technology

Dr. J. David Frost
School of Civil and Environmental Engineering
Georgia Institute of Technology

Dr. Christian Huber
School of Earth and Atmospheric Sciences
Georgia Institute of Technology

Dr. Glenn Rix
School of Civil and Environmental Engineering
Georgia Institute of Technology

Date Approved: December 11, 2012

ACKNOWLEDGEMENTS

I am deeply thankful to my family for their unconditional support and Paola for her love and company throughout these years of ups and downs. I am also very grateful to my friends in Atlanta for the wonderful moments we spent together.

I would like to express my sincere gratitude to Dr. Santamarina for being an extraordinary advisor and showing me that dreams can come true with passion and committed work. Thanks to all the past and current members of the PMRL who I had the chance to share with. It has been a delightful experience to be part of this research group. To all of you, I am certain that this is the beginning of long-lasting friendships.

I would like to thank the insightful contributions of the committee members Dr. J. David Frost, Dr. Glenn Rix, Dr. Dominic Assimaki, and Dr. Christian Huber. I also acknowledge Dr. Hosung Shin (University of Ulsan, South Korea) for his crucial contributions to the numerical implementation in Chapter 4.

This doctoral thesis was supported by the Fulbright U.S.-Chile Equal Opportunities Scholarship Program, the U.S. Department of Energy, and the Goizueta Foundation.

TABLE OF CONTENTS

LIST OF TABLES

LIST OF FIGURES

Page

SUMMARY

Improvements in quality of life, population growth, and environmental restrictions associated with the burning of fossil fuels will accentuate the need for renewable energy and energy geo-storage. A salient characteristic of these systems is that they impose numerous cycles of effective stress, temperature, and humidity on the surrounding geomaterials. This thesis quantifies future energy consumption based on realizable scenarios and explores the behavior of geomaterials subjected to mechanical and thermal cycles in view of energy-related applications. The long-term behavior of geotechnical systems subjected to a large number of mechanical load cycles is studied with a new numerical scheme based on a hybrid finite element formulation. The numerical scheme satisfies initial conditions as well as fundamental characteristics of soil behavior, such as threshold strain, terminal density, and long-term ratcheting. Numerical results show that shallow foundations subjected to repetitive loading experience strain accumulation and stress redistribution. On the other hand, the long-term behavior of energy piles, exposed geomembranes on slopes, and jointed rock masses subjected to cyclic thermal changes is studied using a combination of numerical, analytical, and experimental methods. Results show that thermal cycles lead to the gradual accumulation of plastic displacements, which may be amplified by thermally-induced wedging in jointed rock masses. In general, cumulative effects caused by repetitive loads increase with the number of cycles, the static factor of safety, the amplitude of the cyclic excitation, and the magnitude of the cyclically-induced displacement with respect to the critical elastic displacement.

CHAPTER 1

INTRODUCTION

Population growth and improvements in quality of life will increase global energy demand. Environmental implications associated with the burning of fossil fuels will accentuate the need for renewable energy and energy geo-storage (Figure 1.1). A salient characteristic of many energy systems is periodic thermal, chemical, or mechanical loading; hence, geomaterials involved in these systems are subjected to numerous cycles of effective stress, temperature, and humidity. This thesis addresses these topics in six independent chapters (organization is shown in Figure 1.2).

Chapter 2 presents a human-centered analysis of the worldwide energy situation in terms of quality of life-related variables that are affected, but not directly determined, by energy consumption. Historical data are used to predict various plausible energy consumption scenarios that optimally steer future energy demands. The scenarios consider the coupling between energy consumption rate per capita, quality of life, population growth, social inequality, and governments' energy-for-life efficiency.

Chapter 3 analyzes the geomechanical implications of thermal energy storage and large mechanical energy storage systems, such as compressed air energy storage (CAES) and pumped hydro storage (PHS). The power and energy capacity, the energy density, and the cost of various alternatives are compared; and the effects of effective stress, temperature, wet-dry, and freeze-thaw cycles on long-term cyclic response of energy geo-storage systems are examined.

The repetitive variation of boundary conditions in a soil mass causes strain accumulation. Conventional numerical methods fail to track strain accumulation when thousands of loading cycles are involved. *Chapter 4* advances a numerical scheme using the finite element method to solve long-term problems with repetitive mechanical

boundary conditions. A mechanical constitutive model is used to analyze the static load and first load cycle, and empirical accumulation functions are utilized to track the deformation accumulation during repetitive loading. This hybrid numerical scheme captures fundamental characteristics of soil behavior under repetitive loading, such as threshold strains, terminal density, as well as ratcheting, and predicts volumetric and shear strains as a function of the static stress obliquity, the number of load cycles, and the plastic strain during the first load cycle. The proposed numerical scheme is used to analyze a shallow foundation subjected to repetitive vertical and oblique loads, and a rigid footing subjected to an eccentric cyclic vertical force.

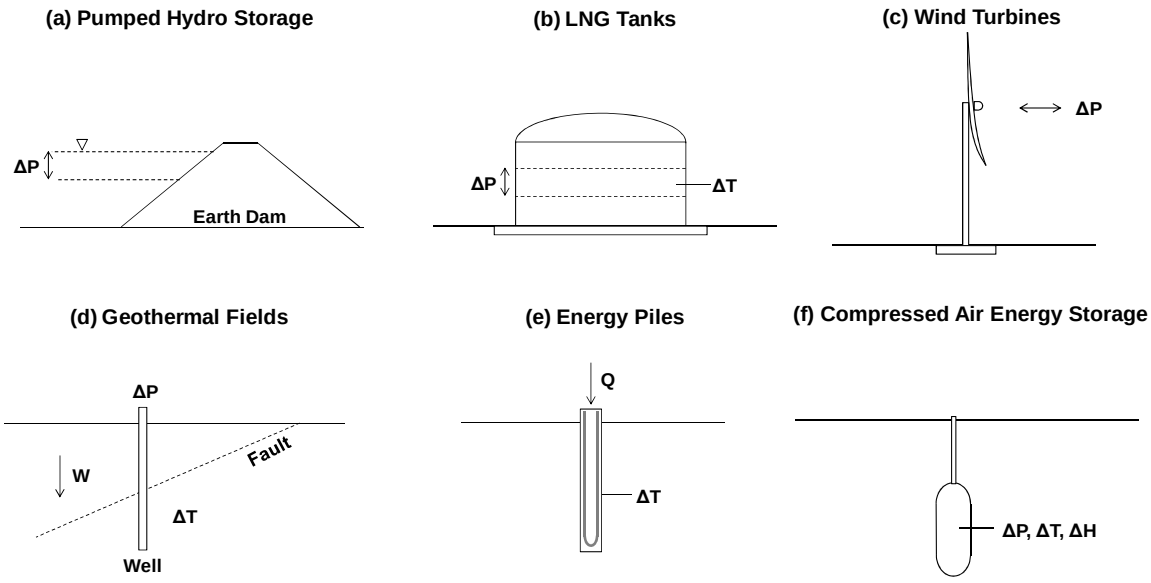

Figure 1.1 Energy systems involving geomaterials. (a) Pumped-hydro storage: changes in water level cause changes in effective stress in the earth dam. (b) LNG tanks: filling and withdrawing of natural gas change the tank weight ΔP and temperature Δ*T*, affecting the foundation soil. (c) Wind turbines: cyclic wind action Δ*P* exerts repetitive loading on the foundation. (d) Geothermal fields: changes in injection pressure Δ*P*, cooling of the rock formation Δ*T*, and self-weight *W* may trigger fault activation. (e) Energy piles: temperature change Δ*T* and static load *Q* can induce permanent downward displacement. (f) Compressed air energy storage: changes in internal air pressure Δ*P*, temperature Δ*T*, and humidity Δ*H* causes effective stress changes in the surrounding rock formation.

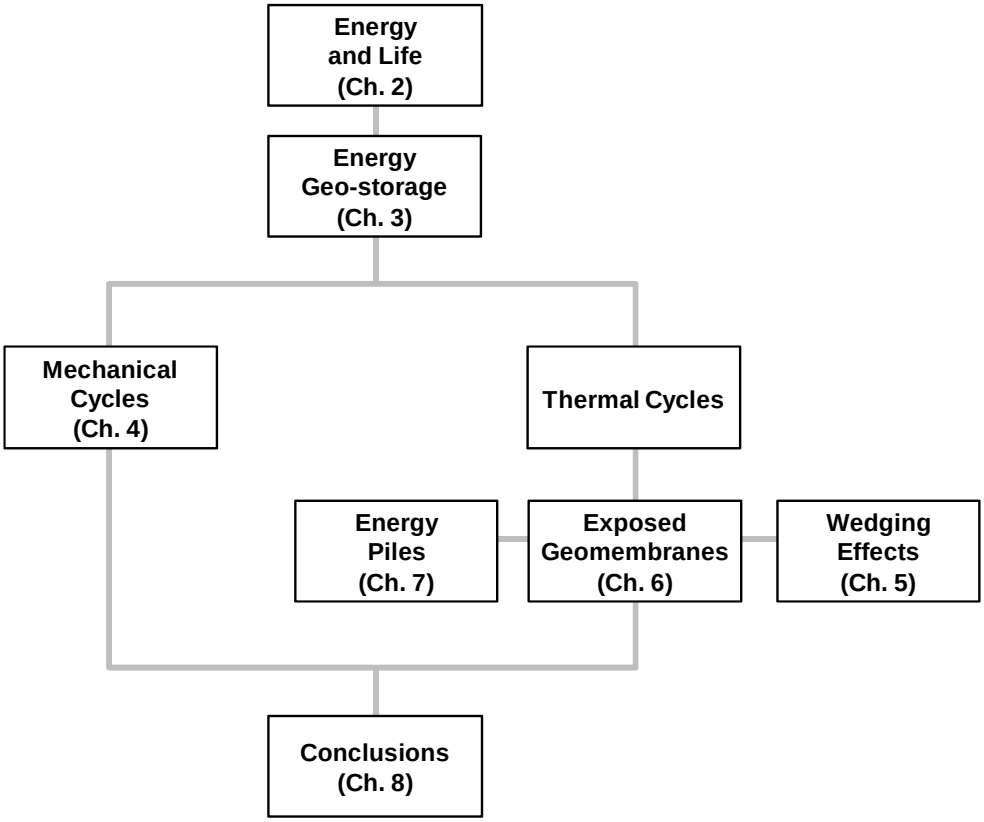

Figure 1.2 Thesis organization.

The repetitive action of temperature changes may cause the gradual accumulation of plastic displacements and compromise the long-term performance of geosystems from slopes and energy piles to the behavior of geomembranes.

Chapter 5 proposes a thermally-induced wedging and ratcheting mechanism to explain observed incremental cliff displacements that correlate with temperature changes and cannot be explained with conventional failure mechanisms, such as sliding, toppling, seismically-induced instability, and water accumulation. The proposed mechanism is captured in an analytical model that accounts for the system geometry, intact rock thermo-mechanical properties, and joint mechanical properties. An experimental study is performed to corroborate the proposed mechanism.

Chapter 6 studies the behavior of geomembranes on inclined planes subjected to thermal cycles. The numerical method considers the thermo-elastic membrane properties, constant amplitude thermal cycles, and an elastic-perfectly plastic constitutive model with constant critical displacements for the membrane-soil interface. Numerical results are experimentally validated. Implications extend to natural rock slopes subjected to temperature cycles.

Chapter 7 examines the influence of temperature cycles on the long-term displacement of energy piles. A numerical method based on the one-dimensional load-transfer method, modified to account for thermo-elastic effects, is proposed in order to quantify the pile long-term displacement response. The numerical method considers the thermo-elastic pile properties, the applied vertical load, the amplitude of thermal cycles, and the shaft and base strength and stiffness. The effects of the working load, the shaft and tip capacity, and the temperature amplitude are studied.

Finally, *Chapter 8* summarizes the most relevant conclusions from this thesis.

CHAPTER 2

ENERGY AND QUALITY OF LIFE

2.1 Introduction

Energy is required to sustain and improve quality of life. The dramatic societal changes and the six-fold population growth since the industrial revolution have required vast amounts of energy provided mainly by coal and petroleum (Hall et al. 2003). In the near future, further population growth and improvements in quality of life will increase the demand for non-renewable fossil fuels and intensify the associated environmental implications (IPCC 2007; Lee 2011).

In the meantime, the high rate of fossil fuel consumption accelerates their depletion (Bentley et al. 2007 - note: two-thirds of the world's oil-producing countries are already past their production peak), technological readiness and economic return on investment hinders the development of non-conventional fossil fuel sources (Arent et al. 2011; Resch et al. 2008), the hydroelectric capacity is almost saturated (EIA 2010), renewed concerns affects investment in nuclear energy (Glaser 2011), and renewables grow fast but starting from a small base (REN21 2011). In this context, improvements in efficiency and conservation must remain important components in the global energy strategy (Herring 2006).

Other aggravating conditions add further concerns to the present situation. The spatial mismatch between resource and demand strains international affairs (Colgan 2010). Trade balance and technological differences imply disparities in energy and carbon dioxide embodied in global transactions (Machado et al. 2001; Peters and Hertwich 2008). Finally, the contrast in the time scale between the political cycle (~4

years), industrial investments (~40 years), and natural processes (millennia) delays determined decision-making.

The purpose of this study is to anticipate energy needs and to explore alternative scenarios from a quality of life perspective. First, the most meaningful quality of life-related indicators were identified and combined to define the simplest quality of life index *QL* that best predicts the energy consumption rate per capita. Then, the new index was used to trace global energy consumption trends and to explore the relationship between quality of life and population growth. Finally, future energy demands are anticipated based on current trends and the effects of various realizable scenarios are explored.

2.2 New Quality of Life Index in View of Energy Needs

Several indices, such as the human development index of the United Nations (UNDP 2010), the human welfare index of Meadows and Randers (Meadows et al. 2004), and the quality of life index of the Economist Intelligence Unit (EIU 2007) have been proposed to compare societies and to quantify their improvements. All these indices consider income, which inherently biases the indices to show a high correlation with energy consumption, as will be discussed later on.

2.2.1 Quality of life Variables

An alternative quality of life indicator is explored herein in terms of quantifiable quality of life-related variables that are not directly determined by energy consumption. Emphasis is placed on variables that are available for most countries over several decades. Based on these considerations, the following four variables are identified:

- Improved Water Access *WA* [-]: Proportion of the population using improved drinking-water sources, such as public tap, tube well, and protected springs (UN 2011c).

- Life Expectancy at Birth *LE* [yrs]: The number of years a newborn infant would live if the mortality patterns at the time of birth prevail throughout the individual's life (WB 2011c).
- Infant Mortality Rate *IM* [deaths/1000 live births]: The number of infants that die before reaching one year of age, per 1,000 live births in a given year (WB 2011d).
- Mean Years of Schooling *MYS* [yrs]: Lifetime number of years of education received by individuals ages 25 and older (Barro and Lee 2010; UN 2011b; WB 2011b).

Two additional variables, electrification level and income, are compared in this section. They are defined as follows:

- Electrification Level *EL* [-]: Proportion of the population with access to electricity (DM 2011; Elvidge et al. 2011; IEA 2010).
- Gross National Income per Capita *GNI* [US$/person]: Sum of value added by all resident producers in the economy divided by the mid-year population. It is expressed in purchasing power parity in US$ (UN 2011a).

However, these two variables are not included in the definition of the new quality of life index because they would systematically bias the correlation between the index and the energy consumption: electrification, a critical infrastructure to quality of life, is inherently correlated with primary energy use, and income is the monetary dimension of energy.

Figure 2.1 shows a plot of the selected variables for 118 countries versus the energy consumption rate per capita *ECR* [kW/person], which is computed as the annual rate of primary energy use divided by the country's population (EIA 2011). Primary energy includes petroleum, natural gas, coal, hydroelectricity, and renewable energy (i.e., wind, solar, and geothermal). Embodied energy in food, the direct use of biomass, and other renewable energy sources, such as solar energy for heating, are not considered.

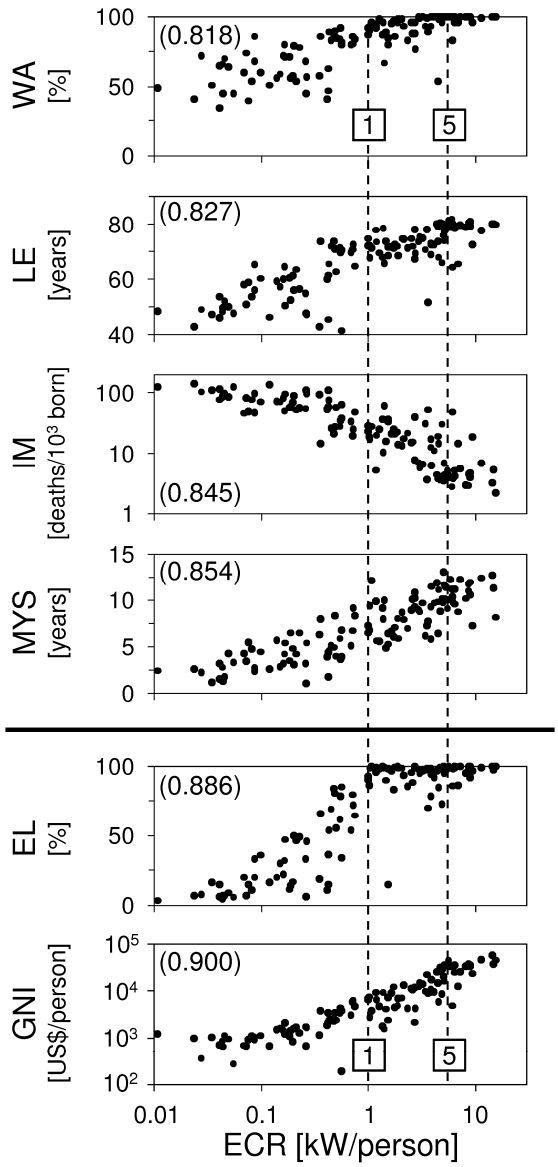

Figure 2.1 Quality-of-life-related variables and energy consumption rate per capita *ECR*: Improved water access *WA*, life expectancy *LE*, infant mortality *IM*, mean years of schooling *MYS*, electrification level *EL*, and gross national income *GNI*. Correlation coefficient in parentheses (infant mortality and gross national income are considered in logarithmic scale). Note: Data for 118 countries with populations larger than four million in 2005.

Although countries with high energy consumption rates collapse in the figure, the logarithmic scale helps us to differentiate countries with low consumption and highlights the three orders of magnitude difference between countries with low and high energy

consumption. Water access, life expectancy, mean years of schooling, electrification level, and gross national income increase with the energy consumption rate, whereas infant mortality decreases. Indices are sorted by the correlation coefficient shown in parentheses; the range in infant mortality and gross national income exceeds two orders of magnitude, so the correlation coefficient is calculated with the logarithm of the indices.

Two threshold values can be identified in the figure. First, an energy consumption rate of 1 kW/person can ensure access to drinking water and electricity, a high life expectancy, and low infant mortality. Second, consumption in excess of ~5 kW/person is not needed to attain the highest values of the quality of life indicators. These energy thresholds reflect today's technology and will decrease with the development of new energy-oriented technology.

2.2.2 Quality of Life Index

Let's identify the quality of life index *QL* that both combines quality of life-related variables, *WA*, *LE*, *IM*, and *MYS*, and exhibits the strongest correlation with the measured energy consumption rate per capita. Since consumption ranges over more than three orders of magnitude between countries, the sought index is the best predictor of the logarithm of the energy consumption rate. Linear and factorial combinations are explored:

$$QL = \alpha \cdot WA + \beta \cdot \left(\frac{LE}{yrs} \right) + \gamma \cdot \log\left(\frac{IM}{deaths/1000born} \right) + \delta \cdot \left(\frac{MYS}{yrs} \right) + \varepsilon \qquad (2.1)$$

and

$$QL = \left[WA \cdot \left(\frac{LE}{yrs} \right) \cdot log\left(\frac{IM}{deaths/1000born} \right) \cdot \left(\frac{MYS}{yrs} \right) \right]^{\frac{1}{4}} + \varphi \ . \qquad (2.2)$$

The constants α, β, γ, δ, ε, and φ are determined by error minimization (note: L_1, L_2, and L_∞ norms were considered; results presented here are based on the least squares L_2 norm).

Following Ockham's criterion, the smallest variable set that does not compromise predictability is identified. The linear combination of life expectancy *LE* and mean years of schooling *MYS* correlates with the logarithm of the measured energy consumption rate per capita almost as highly as any other combination of the four variables (in part due to correlations among the variables). Due to simplicity and historical data availability, these two variables are adopted to define the new quality of life index

$$QL = 0.072\left(\frac{LE}{yrs}\right) + 0.310\left(\frac{MYS}{yrs}\right) - 2.16\,. \tag{2.3}$$

The coefficients are adopted such that the maximum quality of life index QL_{max} = 10 corresponds to a life expectancy LE_{max} = 100 years and mean years of schooling MYS_{max} = 16 years, and the minimum quality of life index QL_{min} = 0 corresponds to LE_{min} = 30 years and MYS_{min} = 0 years (note that this quality of life index can be computed for an individual or group). The best and worst life expectancy and education statistics can be used to estimate the maximum and minimum quality of life attained in 2010: $LE_{\max}$ = 83.2 years (Japan) and $MYS_{\max}$ = 12.6 years (Norway) gives $QL_{\max}$ = 7.7, whereas $LE_{\min}$ = 44.6 years (Afghanistan) and $MYS_{\min}$ = 1.2 years (Mozambique) combine to produce $QL_{\min}$ = 1.4.

2.2.3 Correlation between Quality of life Index and Energy Consumption Rate

Figure 2.2 shows the quality of life index plotted as a function of the logarithm of the energy consumption rate per capita. The *QL* index has a correlation coefficient *cc* = 0.902 with the logarithm of the 2005 energy consumption rate per capita in 118 countries with populations larger than four million. For a given consumption, Eq. (2.3) suggests that a 4.3 year increase in life expectancy requires the same increase in energy consumption as an additional year of schooling.

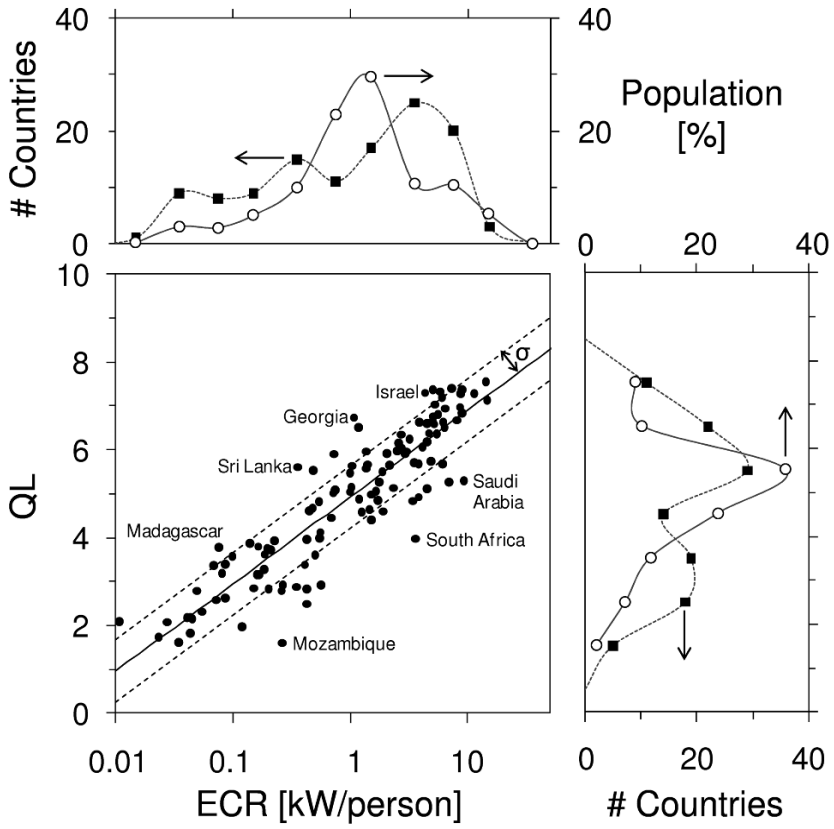

Figure 2.2 Quality of life index *QL* and energy consumption rate per capita *ECR*. Data for 118 countries with populations larger than four million in 2005. The continuous line is the mean trend; dashed lines show the plus and minus one standard deviation lines. Note: Distance is defined as $d^2 = \Delta QL^2 + [\Delta\log(ECR/[\text{kW/person}])]^2$.

Histograms in the figure show two groups. The first group of 30 countries with low energy consumption rates between 0.03 and 0.3 kW/person corresponds mainly to African and Asian countries; their *QL* index ranges between 1.5 and 4.0. The second group of 62 countries between 1 and 11 kW/person includes Latin American countries in the lower end, and European and North American countries towards the upper end; their *QL* index ranges between 4.0 and 7.5.

Figure 2.2 includes the mean plus-and-minus one standard deviation trends. Countries that plot below the mean minus one standard deviation exhibit particularly

inefficient energy use from a quality of life perspective. This group includes high-energy-consumption countries, such as Saudi Arabia, Russia, Libya, Belarus, Iran, and South Africa, and low-energy-consumption countries, such as Zimbabwe, Yemen, Angola, and Mozambique. In contrast, countries that plot above the mean plus one standard deviation reflect their ability to attain high quality of life standards for a given energy consumption rate. This group includes Israel and the Czech Republic (both with $QL > 7$), and Sri Lanka, the Philippines, Peru, Cuba, and Georgia (all with $ECR < 1.2$ kW/person).

Currently, 15% of the world's population consumes more than 5 kW/person and accounts for 49% of the world's total energy consumption. This excess consumption above that needed to attain the highest levels of quality of life reflects prevailing lifestyles and cultural patterns. In contrast, 6% of the world's population lives under very precarious conditions and without basic services, consuming less than 100 W/person (equivalent to a healthy diet of 2000 kcal/day). These people rely on hunting, agriculture, and wood for fuel and construction, all of which are sustained by solar energy and natural processes.

2.3 Historical Trends – Analysis

The quality of life index computed with Eq. (2.3), using data available for several decades, allows us to assess global trends and to trace the evolution of selected countries. The mean trends for 1980 and 2010 plotted in Figure 2.3 show a global increase in quality of life of about $\Delta QL = 1.2$; this is the compounded effect of a 7 years increase in life expectancy and 2.5 years increase in mean years of schooling. Several countries have followed more decisive growth than the global trend. Complex trajectories in Figure 2.3 typically reflect political conflicts and social turmoil experienced during this 30-year period. For example, the civil war in Rwanda from 1990 to 1994 corresponds to a sharp decrease in its *QL* index.

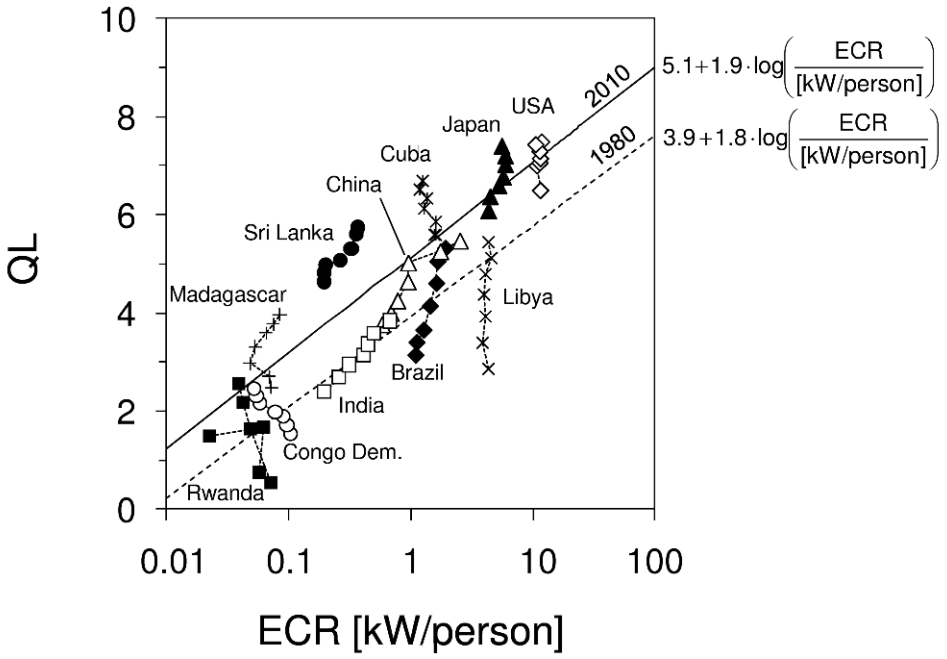

Figure 2.3 Evolution of quality of life index *QL* and energy consumption rate per capita *ECR*. The evolution of selected countries from 1980 to 2010 is shown in five-year intervals. Lines show the mean trends in 1980 (calculated with 100 countries) and in 2010 (calculated with 119 countries).

2.3.1 Energy Efficient Growth

The increase in the quality of life index ΔQL normalized by the change in energy consumption rate ΔECR [kW/person] is a measure of life-oriented energy efficient growth. Based on this concept, the efficiency angle α is defined as

$$\alpha = \tan^{-1}\left[\frac{\Delta QL}{\Delta ECR/(kW/pers)}\right]. \qquad (2.4)$$

An increase in quality of life without an increase in energy consumption corresponds to $\alpha = 90°$. Countries with low efficiency angles use more energy per capita to attain similar improvements in quality of life. Figure 2.4 shows the efficiency angle calculated using increments of the energy consumption rate and the quality of life index

in the 30-year period from 1980 to 2010. Values of α are plotted versus the *QL* index and energy consumption rate in 2010. Countries with $\alpha > 90°$, such as Mozambique, the Democratic Republic of the Congo, Libya, Cuba, and the United States, have increased their quality of life while decreasing their energy consumption during these 30 years.

Mathematically, the linear trend in Figure 2.3 $QL = a_{EC} + b_{EC} \log(ECR/[\text{kW/person}])$ can be used to compute the angle as $\alpha = \tan^{-1}(dQL/dECR)$; which is superimposed on Figure 2.4b. Results show that the energy required to raise the quality of life increases with the energy consumption rate per capita. In other words, a small increase in energy use in countries with low energy consumption can result in a large increase in their *QL* index.

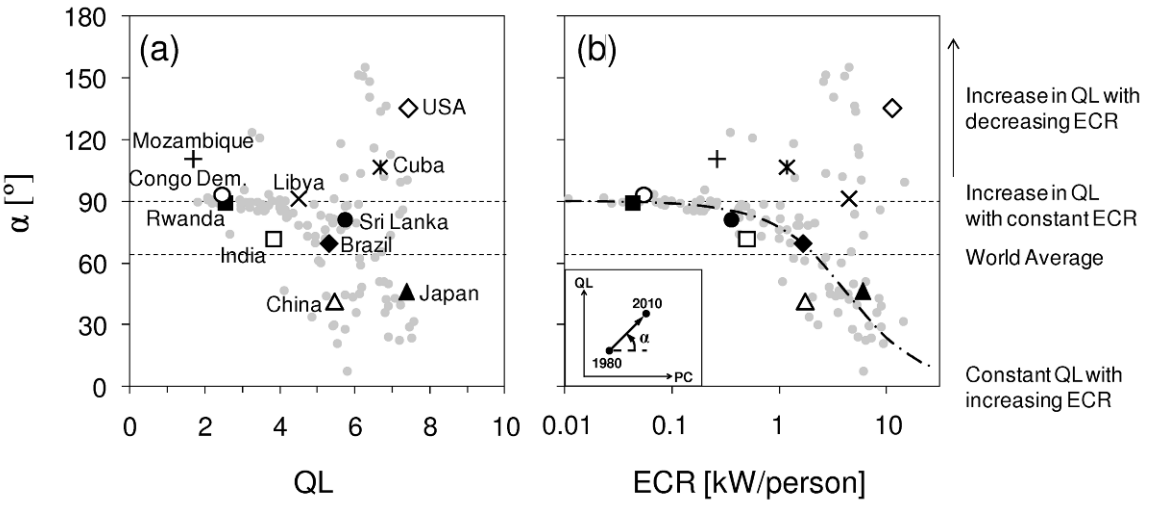

Figure 2.4 Efficiency angle α versus (a) quality of life index *QL* and (b) energy consumption rate per capita *ECR*. The efficiency angle corresponds to the 30-year period between 1980 and 2010 (definition in the right pane insert). Values of the quality-of-life index and the energy consumption are for 2010. The 100 countries plotted have populations larger than four million in 2010. The dashed trend corresponds to $\alpha = \tan^{-1}(dQL/dECR)$ where $QL = a_{EC} + b_{EC} \log(ECR/[\text{kW/person}])$.

2.3.2 Population Growth

Population growth rates calculated in five-year intervals PG_5 [%] are plotted against the quality of life index corresponding to the first year of the interval in Figure 2.5. Results show that population growth rate is inversely correlated with the *QL* index adopted in this study (Eq. 2.3),

$$PG_5 \approx 20 - 2.5\,QL \tag{2.5}$$

In general, the evolution of the population growth rate in individual countries in the 1980-2010 period has followed the global trend (Figure 2.5). For instance, Brazil, India, and Japan have experienced a steady decrease in population growth rate as the quality of life increased since 1980. Several countries with a low *QL* index, such as the Democratic Republic of the Congo, experienced instability during this period and exhibited an inconsistent population growth pattern. The inverse correlation between population growth and quality of life aggravates predictions of energy demands since a high increase in energy consumption is expected in the developing world. Countries that manage to improve their quality of life with a constant energy consumption rate per capita (i.e., α = 90^o) will eventually lower their total energy consumption as their populations stabilize.

2.4. Scenarios: Quality of Life-Centered Energy Consumption Predictions

Predictions of energy consumption must consider the coupling between consumption, quality of life, and population growth. Given the time delay in data availability, the year 2010 is selected as the base year.

A country's rate of energy consumption is the product between its population *P* and its energy consumption rate per capita *ECR*; the global energy consumption rate is computed as a summation for all countries

$$ECR_{global} = \sum_k ECR_k \cdot P_k \,. \tag{2.6}$$

For the base year 2010, the global energy consumption rate was ECR_{global} = 17 TW. Similarly, the global quality of life index is calculated as

$$QL_{global} = \frac{\sum_k QL_k \cdot P_k}{\sum_k P_k} . \quad (2.7)$$

The summation is extended to all countries where data is available to calculate the quality of life index QL_k. The global quality of life index in 2010 was QL_{global} = 5.0. Finally, 5-year changes in population growth rate ΔPG_5 [%] are related to changes in the quality of life index ΔQL (see Eq. 2.5 and Figure 2.5 – note: restrictions may apply):

$$\Delta PG_5 = -2.5 \cdot \Delta QL \ . \quad (2.8)$$

Several scenarios are explored to identify strategies that maximize global quality of life in terms of energy demands. The computation algorithms and assumptions for all scenarios are summarized in Table 2.1. Equations listed above and the additional constraints imposed in these scenarios combine to render non-linear predictions; in all cases, 30-year predictions are computed by updating all variables every five years.

2.4.1 Scenario 1: Status Quo

This scenario predicts the global energy consumption rate, based on historical increments of energy consumption rate per capita and the quality of life index. Since increments are very sensitive to short-term transients, both the change in energy consumption rate ΔECR_5 and the change in quality of life index ΔQL_5 are considered as the average of the five-year increments from 1980 to 2010. Extrapolation leads to unreasonable predictions for a few countries. Although such anomalous predictions do not affect the global result, two limits are imposed: the maximum quality of life index is limited to $QL \leq 10$ and the minimum energy consumption rate is restricted to $ECR_{min} \geq$ 0.1 kW/person.

Table 2.1 Algorithms for Energy Consumption Scenarios

Variable	Scenario 1 Limiting Energy Overspending	Scenario 2 Stimulating Growth in the Developing World	Scenario 3 Improving Energy-for-Life Efficiency	Scenario 4 Restricting Population Growth
α	α_{curr} (a)		α_{curr} *if* $\alpha_{min} < \alpha_{curr} < 180°$ α_{min} *if* $\alpha_{curr} \leq \alpha_{min}$	α_{curr}
ΔECR_5	$(ECR_{2010} - ECR_{1980})/6$			
ΔQL_5	$(QL_{2010} - QL_{1980})/6$		$\Delta ECR_5 \cdot \tan \alpha$	$(QL_{2010} - QL_{1980})/6$
ECR_{j+1} (b)	$ECR_j + \Delta ECR_5$			
Constraint at year 2040	$ECR_{2040} \leq ECR_{\max}$	$EC_{2040} \geq ECR_{min}$ $QL_{2040} \geq QL(ECR_{min})$ (c)	Not applicable	Not applicable
QL_{j+1} (d)	$QL_j + \Delta QL_5$			
PG_{j+1}	$PG_j - b_{PG} \cdot (QL_j - QL_{j-1})$ (e)			$PG_j - b_{PG} \cdot (QL_j - QL_{j-1}) \leq PG_{max}$
P_{j+1}	$P_j \cdot (1 + PG_{j+1})$			

Notes: (a) $\alpha_{curr} = \tan^{-1} [(QL_{2010} - QL_{1980})/(ECR_{2010} - ECR_{1980})]$
(b) $ECR_{j+1} \geq 0.1$ kW/person in scenarios 1 and 3
(c) $QL(ECR_{min}) = a_{EC} + b_{EC} \cdot \log(ECR_{min}) + 2\sigma b_{EC}/(b^2+1)^{1/2}$; a_{EC} is the intercept, b_{EC} is the slope, and σ is the standard deviation of the perpendicular distance to the mean log(*ECR*) – *QL* trend in the status-quo scenario for 2040.
(d) $QL_{max} = 10$
(e) $b_{PG} = 2.5$ is the slope of the $QL - PG_5$ trend in Figure 2.5.
(f) *j* to *j+1* is a 5-year period.

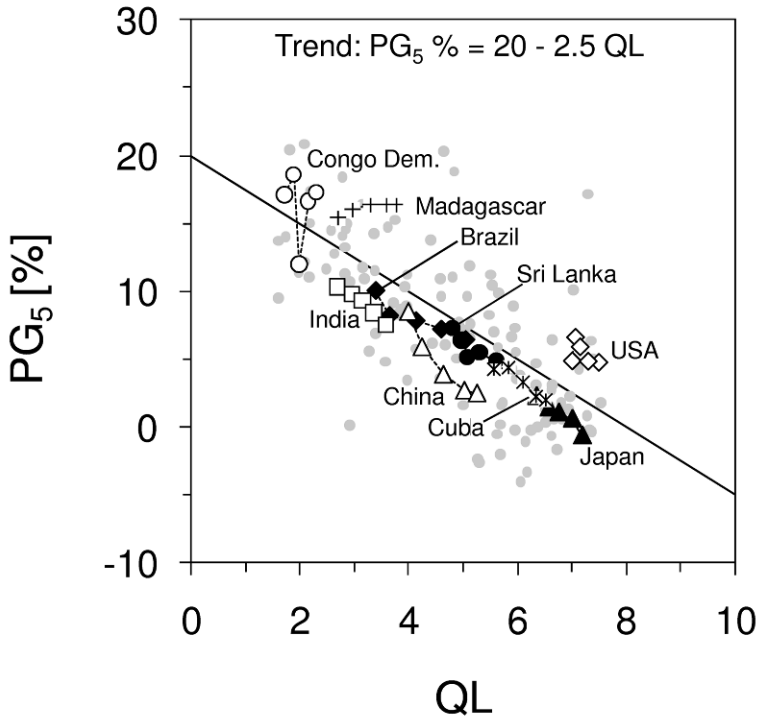

Figure 2.5 Five-year population growth rate PG_5 and quality of life index QL. The evolution of selected countries from 1980 to 2010 is shown in five-year intervals. The corresponding quality-of-life index is the one at the beginning of the period. Dots represent 119 countries with populations larger than four million in the period 2005-2010. The line captures the global trend in the 30-year period from 1980 to 2010.

Figure 2.6 shows the historical evolution and predictions of global energy consumption rate, quality of life index, and population for the status-quo scenario. Predictions by the International Energy Agency (IEA 2009), the U.S. Energy Information Administration (EIA 2010), the United Nations (UN 2011d), and the U.S. Census Bureau (USCB 2011) are superimposed on the figure and are in close agreement with the values predicted under the status-quo scenario in this study. The global energy consumption rate increases to ECR_{global} = 25.5 TW (50% increase), the associated global quality of life index increases to QL_{global} = 6.3 (26% increase), and the population rises to P_{global} = 8.9 billion (30% increase) in 30 years.

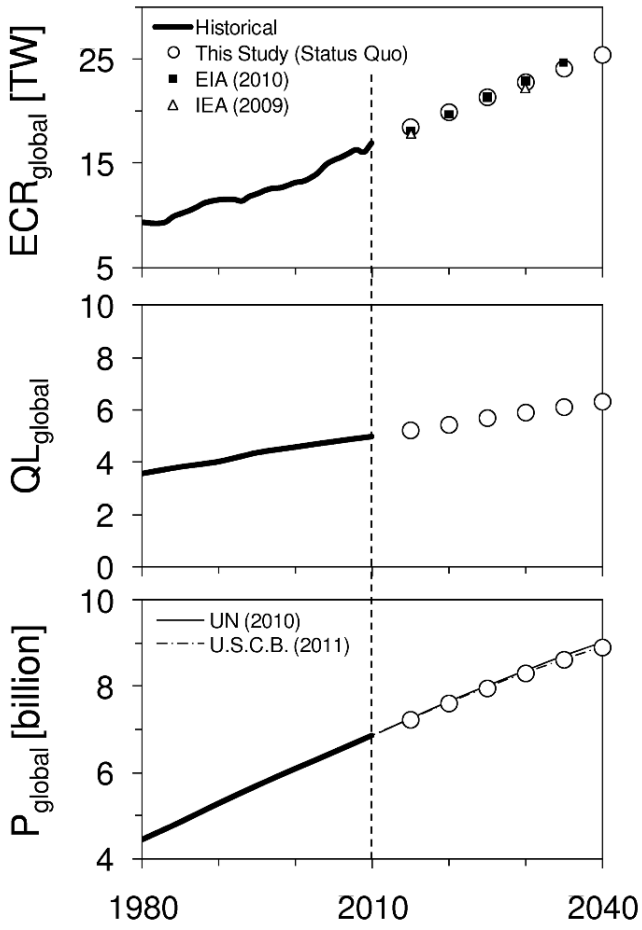

Figure 2.6 Historical evolution and status-quo predictions (scenario 1) of the global energy consumption rate ECR_{global}, global quality of life index QL_{global}, and world population P_{global}. Historical energy consumption and world population data from the U.S. Energy Information Administration EIA (EIA, 2011). Energy consumption projections by EIA (EIA, 2010) and the International Energy Agency IEA (IEA, 2009) are the reference scenarios in the International Energy Outlook 2010 and the World Energy Outlook 2009, respectively. The 2010 United Nations' projection UN (UN, 2011c) is scaled to coincide with the historical population in 2010.

2.4.2 Scenario 2: Limiting Energy Overspending

This scenario limits the maximum energy consumption rate per capita to ECR_{max} in high-consumption countries. As demonstrated in previous sections, the energy consumption rate can be reduced to ~5 kW/person without affecting the quality of life

index, and consequently the population growth rate. In this scenario, all countries change their energy consumption and quality of life index according to the status-quo scenario, but they are not allowed to exceed the selected ECR_{max} value in the 30-year horizon. Figure 2.7 shows that the predicted global energy consumption rate in 2040 decreases sharply as ECR_{max} is lowered, and it could be similar to 2010 global consumption if ECR_{max} is limited to 3.7 kW/person in all countries. Given the assumptions in this scenario, the global quality of life index and the world population evolve as in the status-quo scenario.

2.4.3 Scenario 3: Stimulating Growth in the Developing World

This scenario considers that the minimum energy consumption rate per capita in developing nations will increase to reach a target value of ECR_{min} in the 30-year horizon. If a country's energy consumption rate is lower than ECR_{min} by 2040, its consumption is set to ECR_{min}. In addition, its quality of life index is set to the value given by the status quo mean plus one standard deviation trend in 2040 at ECR_{min}. For all other countries, energy consumption and quality of life index change according to the status-quo scenario. Results in Figure 2.7 show that raising the minimum energy consumption rate $ECR_{min} = 1$ kW/person increases the global energy consumption rate by 7% and the global quality of life index by 11% above the status-quo scenario, whereas the world population is the same as in the status quo prediction.

2.4.4 Scenario 4: Improving Energy-for-Life Efficiency

This scenario imposes a minimum energy use efficiency from a quality of life standpoint, i.e., "energy-for-life efficiency." Countries develop as in the status-quo scenario only if their efficiency angles are larger than α_{min} (Eq. 2.4); otherwise, they are forced to evolve with α_{min}. The 5-year increment in energy consumption rate per capita ΔECR_5 is the same as in the status-quo scenario whereas the 5-year increment of the

quality of life index ΔQL_5 is given by the efficiency angle and the consumption increment, $\Delta QL_5 = \Delta ECR_5 \tan\alpha$. Figure 2.7 shows that the global energy consumption rate decreases from the status quo value as the efficiency angle increases. Eventually, efficiencies larger than $\alpha = 81^o$ lead to energy savings when compared to 2010 global consumption. The global quality of life index has a pronounced increase and the global population a drastic decrease with efficiency angles larger than $\alpha = 50^o$. Note that 21 out of 100 countries considered in Figure 2.4 had efficiencies lower than $\alpha = 50°$ in the 1980-2010 period.

2.4.5 Scenario 5: Restricting population growth

This scenario restricts the maximum population growth rate in any 5-year period to a value $PG_{5\text{-}max}$: if the status-quo scenario predicts a population growth rate larger than $PG_{5\text{-}max}$ in any 5-year interval between 2010 and 2040, the population growth rate for the period is set to $PG_{5\text{-}max}$. The energy consumption rate per capita and the quality of life index evolve as in the status-quo scenario, so only population growth affects the global energy consumption rate. This scenario predicts that the population in 2040 rises by 14% if the maximum population growth is set to $PG_{5\text{-}max} = 4\%$ for all countries (for comparison, the status-quo scenario anticipates a 30% increase in population). The global energy consumption rate increases by 40%, and the global quality of life index increases slightly above the status-quo value to $QL_{global} = 6.5$. Currently, 64% of the world's population lives in countries with population growth rates larger than $PG_5 = 4\%$ (79 out of 119 countries considered in Figure 2.5).

2.4.6 Scenario 6: Combining energy and quality of life policies

Multiple actions can be combined to optimize worldwide quality of life with minimal energy use. Consider the following set of combined strategies: the maximum energy consumption rate per capita is established at $ECR_{max} = 5$ kW/person, the minimum

consumption is raised to reach ECR_{min} = 1 kW/person, the minimum efficiency is set to α_{min} = 70º, and the maximum 5-year population growth rate is limited to $PG_{5\text{-}max}$ = 10%. Thus, the global energy consumption rate in 2040 would increase by 14% with respect to 2010 consumption (status-quo: 50%), the global quality of life index would reach QL_{global} = 7.1 (status-quo: QL_{global} = 6.3), and the world population would be P_{global} = 8.1 billion (status-quo: P_{global} = 8.9 billion).

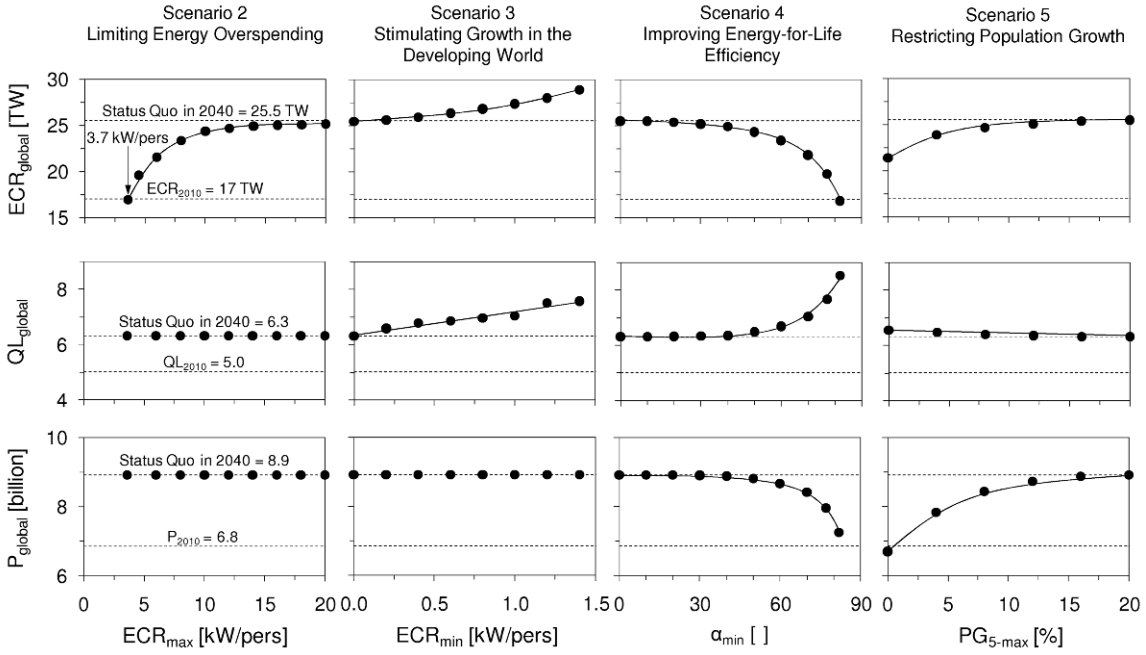

Figure 2.7 Predicted global energy consumption rate ECR_{global}, global quality of life index QL_{global}, and world population P_{global} under various development scenarios in 2040.

2.4.7 Scenario 7: Reducing social inequality

Social inequality sustains internal tension, diminishes quality of life, and hinders development (Wilkinson 2006). The Gini index is a measure of inequality: Gini = 0 corresponds to perfect equality whereas Gini = 100 corresponds to perfect inequality.

Figure 2.8 shows a plot of the Gini index versus the quality of life index defined in this study. Latin American countries exhibit marked inequality, i.e., a significantly higher Gini index compared to countries with a similar quality of life index. Disregarding Latin American countries, the general trend indicates that inequality decreases with an increase in quality of life.

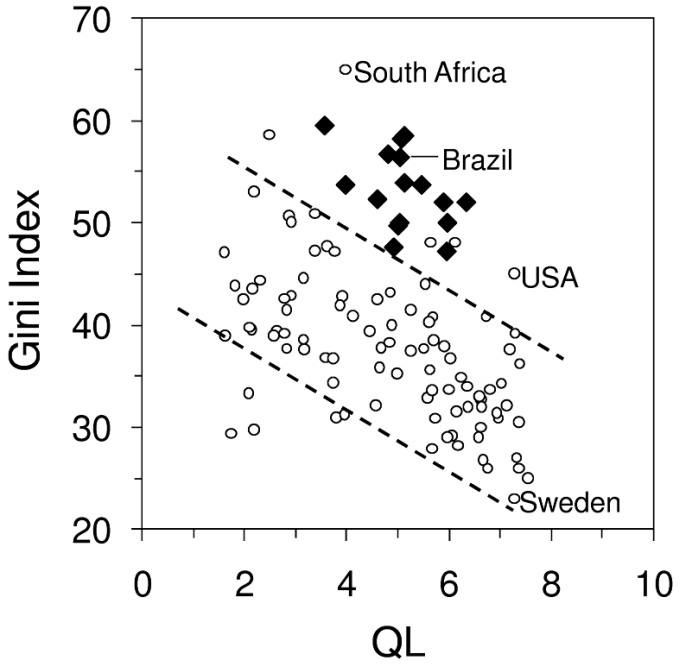

Figure 2.8 Social inequality and quality of life. Gini index versus quality of life index. Data for countries with populations larger than four million in 2005. Diamonds represent Central and South American countries. Note: Gini index = 0 is perfect equality, and Gini index = 100 is perfect inequality. Data gathered from the World Bank (WB 2011a) and Central Intelligence Agency (CIA 2011).

In the absence of disaggregated national data, the global impact of limiting inequality cannot be completed. Nevertheless, the nature of the non-linear relationship between energy consumption rate per capita and quality of life index (Figure 2.2) suggests that improvements in impoverished societies lowers social inequality, increases

the overall quality of life, and has a minor effect on a nation's energy consumption. For example, combining trends in Figures 2.2 and 2.4 allows us to predict that an increase in the average quality of life index $\Delta QL/QL_0$ = 25% requires a energy consumption rate increase $\Delta ECR/ECR_0$ = 18% at 0.1 kW/person, 29% at 1 kW/person, and 41% at 10 kW/person.

2.4.8 Comments

The two variables in the proposed quality of life index, life expectancy and mean years of schooling, correlate with other quality of life parameters. Therefore, improvements in the *QL* index will come together with improvements in all related indicators in most cases, including enhanced access to clean water, electrification, and income.

Scenarios analyzed in this study focus on quality of life and associated energy needs. They do not consider limitations in energy resources, the cost of energy and its implications, possible rates of infrastructure deployment, and potential restrictions on carbon dioxide emissions (Höök et al. 2010).

2.5 Discussion and Conclusions

General Observations: National averages of energy consumption per capita range in three orders of magnitude. Approximately 6% of the world population consumes less than 0.1 kW/person (i.e., the energy in a healthy diet), and 44% is below 1 kW/person (i.e., the energy level required to attain an adequate quality of life given today's technology). On the other hand, 15% of the world population consumes more than 5 kW/person (i.e., the energy required to attain the highest quality of life with today's technology).

Future energy demands will reflect the coupling between energy consumption, quality of life, population growth, social inequality, and governments' energy-for-life

efficiency. Following current trends, the status-quo scenario anticipates a global power consumption of 25.5 TW by the year 2040, which is a 50% increase from the 2010 level and an 8.5 TW increase in global demand in 30 years.

Developing Countries – Observations and Policies: Growth in the developing world will cause a marked increase in global energy demand due to higher energy consumption rate per capita compounded with high values of current population growth rates.

Restricted population growth limits global energy use. Nevertheless, the impact of this single strategy on energy consumption is not significant unless the population growth rate in five year intervals is limited to $PG_{5\text{-}max}$ = 5% worldwide, which is similar to the current population growth rate in the USA.

Yet, significant improvements in quality of life can be attained with a limited impact on energy demands in all nations, particularly in developing countries. In fact, several countries (including Mozambique and Cuba) have successfully increased their quality of life with relatively low increases in energy consumption in the last decades. Furthermore, given the inverse correlation between quality of life and population growth, improvements in quality of life may lead to decreased energy consumption.

Stimulating growth in the developing world to attain a minimum energy consumption rate per capita of ECR_{min} = 1 kW/person increases the global energy consumption by only 7% above the status-quo scenario and has a profound effect on global quality of life. To achieve this goal, emphasis should be placed on the implementation of available technology, the reduction in social inequality, and renewed government policies to enhance energy-for-life efficiency. The widespread use of technology for efficient knowledge delivery and for optimal use of resources, low-cost medicines, and portable medical systems are examples of recent developments that can be made readily available worldwide to improve quality of life with a virtually null increase in energy demand. Partnerships with developed countries and the private sector

may facilitate the development and adoption of leapfrog technology and ensure financial support for energy plans.

Developed Nations - Observations an-d Policies: Affluent societies in developed countries can readily reduce energy overconsumption. Energy consumption rates in excess of ~5 kW/person do not lead to higher quality of life. Furthermore, limiting consumption to 3.7 kW/person would keep 2040 energy consumption at 2010 levels (note: it is anticipated that a consumption rate of 3.7 kW/person is achievable with today's technology with no negative impact on quality of life).

These energy conservation targets can be attained guided by education and motivated by taxation. However, what would individuals do with saved funds, or governments with excess tax collection? All expenditures imply energy consumption; thus, policy instruments must guide the use of saved funds to promote the development and adoption of clean, renewable energy, to correct energy market failures (e.g., not-accounted negative externality costs), and to overcome barriers in the adoption of energy-efficient technology.

Short and Long-term Plan: The implementation of policies properly targeted to developed and developing economies, can optimally steer future energy demands in order to maximize quality of life worldwide. Short-term policies must recognize the current dependency on fossil fuels, their diminishing reserves, and climate implications. In this context, emphasis should be placed on increasing quality of life in the developing world and limiting overconsumption in developed nations. Savings should be invested to cause change towards a long-term solution based on unlimited, clean renewable energy and leap-frog technology required to support a high quality of life worldwide.

CHAPTER 3

ENERGY GEO-STORAGE – ANALYSIS AND GEOMECHANICAL IMPLICATIONS

3.1 Introduction

Fossil fuels are the product of solar-driven photosynthesis accumulated for almost a billion years and they account for nearly 85% of the total primary energy consumption in the world (EIA 2010). Unfortunately, the accelerated consumption of these resources over the past two centuries will eventually lead to supply limitations and ecosystem damage. In this context, the more extensive use of renewable energy sources is gaining relevance as part of a sustainable long-term energy strategy.

Renewable energy sources such as solar, wind, wave, and tidal energy often fluctuate anti-cyclically with electricity demand. For example, solar energy yields maximum output in the daytime whereas the electrical load usually peaks at night. Hence, the use of intermittent renewable energy sources for electric power generation underscores the need for energy storage (Cavallo 2007; Denholm and Margolis 2007; Mason et al. 2008). Large-scale storage systems are needed to accommodate the excess off-peak generation and to deliver high power during peak load (Ibrahim et al. 2008; McLarnon and Cairns 1989). In addition, energy storage allows the operation of power plants at their highest efficiency throughout the year.

The most promising energy geo-storage systems are pumped hydro storage (Garg et al. 1985; Ter-Gazarian 1994), compressed air energy storage (Allen et al. 1985; Giramonti et al. 1978; Succar and Williams 2008), thermal energy storage (Hepbasli 2004; Novo et al. 2010; Sanner et al. 2003), and stored energy in waste (Williams et al. 2003). Large-scale compressed air energy storage and pumped hydro storage have

suitable storage capacities to satisfy current urban demands. On the other hand, distributed small-scale systems, such as thermal energy storage, are attractive for residential-scale applications.

Geo-materials involved in geo-storage systems experience complex cyclic loading that varies with the type and periodicity of the imposed boundary conditions. Generally, these excitations do not cause monotonic failure, but their repetitive application can gradually deteriorate the properties of geo-materials and affect the performance of geo-storage systems.

This study reviews geo-storage systems, provides simple analyses to assess their capacity and cost, and highlights the most important geotechnical challenges in their implementation. In addition, it identifies cyclic loadings on geo-materials, investigates their behavior, and attempts to anticipate emergent phenomena and coupled processes that may compromise the long-term performance of energy geo-storage systems.

3.2 Energy Storage Systems

The requirements for an energy storage system depend on the type and the extent of the mismatch between energy supply and demand. The system must satisfy the transient capacity gap and the rate of energy delivery, or power. As a result, hourly, daily, and seasonal storage systems may be needed.

The volume V [m^3] of a storage system is a function of the stored energy density e_V [J/m^3], either the stored energy E [J] or the delivered power P [W], and the time of supply t [s] as follows

$$V = \frac{E}{e_V} = \frac{P \cdot t}{e_V} \tag{3.1}$$

The duration of the energy storage is a function of the time delay between energy surplus and deficiency. Yet, storage is limited by stability constraints. For example,

energy stored as fuel lasts decades whereas energy stored as heat and high pressure air is conduction- and diffusion-loss limited.

Energy storage depends on energy quality. High-grade mechanical, electrical, magnetic, and chemical energy can be readily converted into other forms of energy with high efficiency. For example, the commercial efficiency of an electric generator, defined as the electrical power output over the mechanical power input, can reach 95%. In contrast, thermal energy is low-grade energy since its transformation into a higher form of energy is limited by the Carnot efficiency,

$$\eta_C = 1 - \frac{T_L}{T_H} \tag{3.2}$$

where T_L [K] and T_H [K] are the low and high temperatures of the cycle. The storage process must prevent the conversion of high-grade energy into low-grade form. Table 3.1 summarizes the efficiency of typical energy conversion devices.

Examples of energy geo-storage in chemical form include national emergency fuel storage in underground caverns (e.g., Strategic Petroleum Reserve maintained by the United States Department of Energy and the Federal Oil Reserve in Germany), and the commercial storage of natural gas, butane, propane, propylene, and gasoline in salt caverns, aquifers or depleted reservoirs (Bary et al. 2002; Katz 1973; Thoms and Gehle 2000). Liquefied natural gas and liquefied petroleum gas may also be stored in refrigerated caverns under very low temperatures; these extreme conditions require an adequate understanding of the behavior of geo-materials under freeze-thaw cycles (Glamheden and Lindblom 2002).

3.2.1 Thermal Energy Storage

Thermal energy storage is recommended only when the available energy surplus is heat, for example, from solar water/air heating systems. The design of a thermal energy storage system mainly depends on the required heat output and the available

space. Thermal energy can be stored as sensible heat or latent heat. Latent heat is preferred when the storage size is limited, but it is typically more expensive than an equivalent sensible heat storage system. In both cases, heat is recovered from the storage medium with a transfer fluid and a heat exchanger. Energy recovery increases with the thermal conductivity and the heat transfer coefficient of the medium. The main cost components of a thermal energy storage system are the cost of the heat storage material, the cost of the space of storage, and the cost of the heat exchanger.

Sensible Heat Storage

The energy density e_V [kJ/m^3] stored as sensible heat in a given material is a function of the material mass density ρ [kg/m^3], its specific heat capacity C_p [kJ/kg/K], and the change in temperature ΔT [K]

$$e_V = \rho \cdot C_p \cdot \Delta T \,. \tag{3.3}$$

Values of specific heat capacity and mass density for several substances are listed in Table 3.2. For example, the energy density of water subjected to ΔT = 10°C is e_V = 42 MJ/m^3. The use of water as sensible heat storage is preferred over other materials, despite the limited range of operating temperatures, because of its low cost, wide availability, large heat capacity, low environmental impact, and the advantages of convective and conductive heat transport. Other advantages include simple heat exchanger geometry, simultaneous heat charging and discharging, direct integration with solar heating/cooling water systems, low cost of pumps and fans, and low corrosion with conventional materials (Farid et al. 2004; Sharma et al. 2009). In contrast, the use of rocks as sensible heat storage is more limited due to their low heat capacity, low thermal conductivity, and unknown response to long-term thermal cycling (Farid et al. 2004).

Table 3.1 Energy Conversion Efficiency

From	To	Devices	Efficiency
Thermal	Mechanical	Heat engine	$\eta = \frac{\text{useful work output}}{\text{heat input}}$ Limited by Carnot efficiency (Cengel and Boles 2001) $\eta_C = 1 - \frac{T_L}{T_H}$ Eq.(3.2)
Electric	Mechanical	Electric motor	$\eta = \frac{\text{mechanical power output}}{\text{electric power input}}$ $\eta_{\max} = 95\%$ (USDOE 2004a)
Chemical	Electric	Fuel cell	$\eta_{ideal} = \frac{\text{change in Gibbs free energy}}{\text{change in enthalpy}}$ $\eta_{ideal} = 83\%$ (1)
Mechanical	Electric	Electric generator	$\eta = \frac{\text{electric power output}}{\text{mechanical power input}}$ $\eta_{\max} = 95\%$

Note: (1) thermal efficiency of an ideal fuel cell operating reversibly on pure hydrogen and oxygen (USDOE 2004b)

Underground thermal energy storage systems typically refer to large-scale sensible heat storage systems that combine the use of water with an underground reservoir. The system rejects or absorbs heat at the surface using a heat exchanger, and may be coupled to an aquifer, a cavern, or a gravel filled space (Novo et al. 2010). These systems are suitable for seasonal storage of solar energy since low surface area to volume ratio reduces heat losses.

Latent Heat Storage

Materials absorb heat to change from solid to liquid or from liquid to gas, and release heat during the reverse phase change. The energy density e_V [kJ/m^3] in a latent heat storage system is proportional to the material specific latent heat for phase transformation L [kJ/kg] and the material mass density ρ [kg/m^3]

$$e_V = L \cdot \rho \tag{3.4}$$

Table 3.2 Specific Heat, Thermal Conductivity, and Mass Density of Different Substances

Substance	**Specific heat capacity C_p** [kJ / kg / K]	**Thermal conductivity λ** [W / m / K]	**Mass density P** [kg / m^3]
Air (dry, 20°C) (1)	1.0	0.03	1.2
Air (dry, 100°C) (1)	1.0	0.03	0.9
Water (80°C) (1)	4.2	0.67	972
Water (20°C) (1)	4.2	0.60	998
Ice (0°C) (1)	2.1	2.14	917
Ice (-80°C) (1)	1.5	3.30	927
Quartz (0°C)	0.7	6.8 to 11.4 (2)	2650
Quartz (100°C)	0.8	4.9 to 8.0 (2)	2650
Granite (3)	0.9	2.9	2600
Salt rock	0.9	6.6 (2)	2160
Paraffin wax	2.9 (4)	0.17 (liquid) (5) 0.34 (solid) (5)	790 (liquid) (5) 916 (solid) (5)
Asphalt (6)	0.92	1.2	2200

Note: Data from (1) Lide (2010); (2) Clauser and Huenges (1995); (3) Heuze (1983); (4) El-Dessouky and Al-Juwayhel (1997); (5) Zalba et al. (2003); (6) Chadbourn et al. (1996)

The latent heat of transformation is large in many materials. For instance, the latent heat of fusion of water, 333 kJ/kg or e_V = 305 MJ/m^3 (properties of ice at 0°C - Table 3.2), is equivalent to the sensible heat corresponding to a temperature increase from 5°C to 78°C (properties of water at 20°C - Table 3.2). Figure 3.1 summarizes the melting point and specific latent heat of fusion for several phase change materials. In the temperature range between 10°C and 60°C, the latent heat of fusion of most materials ranges between 75 and 300 kJ/kg.

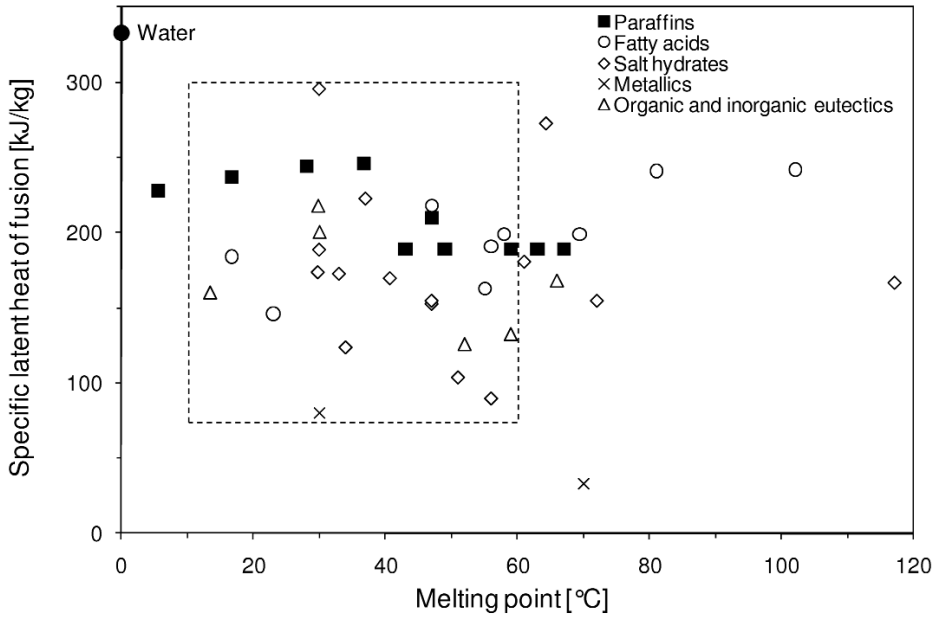

Figure 3.1 Possible phase change materials: melting point and latent heat of fusion (Data from Sharma et al. 2009 and Zalba et al. 2003)

The desired properties of phase change materials include: for thermal properties, phase transition temperature in the range of operating temperatures, high latent heat for phase transformation, and high thermal conductivity; for physical properties, congruent melting in order to avoid composition differences between the solid and liquid phase, high density, small volume change during phase transition, and low vapor pressure; for kinetic properties, no supercooling during freezing and a high crystallization rate; and for chemical properties, long-term chemical stability, compatibility with container materials, non-toxic, and non-flammable. Phase change materials generally have low thermal conductivity and expand upon melting (Garg et al. 1985; Sharma et al. 2009).

Phase change materials are classified into three main groups: organic, inorganic, and eutectic. Organic materials can be subdivided into paraffin and non-paraffin compounds. Paraffin compounds are among the most reliable in latent heat storage systems due to their availability, cost, and safeness. They also have a wide range of

melting points, are chemically inert (stable below 500°C), and exhibit volume change upon melting on the order of 10% (Dincer and Rosen 2011; He and Setterwall 2002). The latent heat of fusion of paraffins is about L = 200 kJ/kg (Figure 3.1). For a mass density ρ = 850 kg/m^3 (Table 3.2), the approximate energy density of paraffin is e_V = 170 MJ/m^3. However, paraffin compounds have low thermal conductivity and are chemically incompatible with some plastic containers.

The stability of the phase change material under thermal cycling (Farid et al. 2004) and the long-term stability of the surrounding geo-materials under induced chemical stresses (Wang et al. 1998) may limit latent heat storage. Other inherent difficulties arise from the solid-liquid interface movement as the phase change material melts: heat exchange decreases because the heat transfers through the low thermal conductivity liquid phase (see values for paraffin wax in Table 3.2) and a more complex heat exchanger configuration is required.

Geothermal Heat Pump

A geothermal or ground-coupled heat pump is a sensible heat storage system that combines a heat pump with a ground heat exchanger in a closed or open loop system configuration to extract thermal energy stored underground during the summer surplus. The heat pump exchanges heat with the soil mass via a fluid that circulates in pipes either placed directly in vertical boreholes or horizontal trenches or incorporated into foundation elements such as piles and basement slabs (Brandl 2006; Hepbasli 2004; Omer 2008).

The number and size of heat exchangers depend on the thermal properties of the soil, the radius of influence and the interaction between neighboring systems, and the thermal coupling between the fluid, the pipe, the grout, and the soil in the borehole. Geothermal heat pumps can be used in combination with phase change materials to enhance thermal storage.

3.2.2 Mechanical Energy Storage

Large energy geo-storage systems are pumped hydro storage and compressed air energy storage.

Pumped Hydro Storage

Pumped hydro systems store potential energy using low-cost off-peak electric power to elevate water from a lower to a higher reservoir. The stored water is then discharged to run turbines and generate electric power during peak demand periods (Deane et al. 2010). The potential energy density e_V [kJ/m^3] of a fluid with unit weight γ [kN/m^3] raised to an elevation ΔH [m] is

$$e_V = \gamma \cdot \Delta H \tag{3.5}$$

The energy density of water elevated ΔH = 100 m is e_V = 1 MJ/m^3 (mass density of water at 20°C - Table 3.2). This relatively small value can only justify large-scale storage, which requires large inundation areas.

The total stored energy can be expressed as a function of the discharge rate q [m^3/hr] and the duration of discharge t [hr]

$$E = \eta \cdot q \cdot \gamma \cdot \Delta H \cdot t \tag{3.6}$$

where the efficiency coefficient η accounts for energy losses during discharge. Approximately 70 to 85% of the electrical energy used to elevate the water is recovered during the generation stage. To avoid large inundation areas, pumped hydro storage systems are built using lakes as reservoirs or operated with underground, sealed mines (Uddin and Asce 2003). Geographical constraints and high capital cost are the main drawbacks of these systems (Yang and Jackson 2011).

Compressed Air Energy Storage

A conventional compressed air energy storage power plant utilizes excess low cost electricity generated during off-peak periods to compress and store a large volume of

air in an underground cavity or reservoir. The stored air is later released and expanded with heat provided by fossil fuels to drive turbines that generate electricity during peak periods. Alternative adiabatic concepts couple compressed air energy storage with thermal energy storage to reduce fuel consumption using the heat generated during the compression stage to expand the air as it is released from storage to drive the turbines (Bullough et al. 2004; Najjar and Jubeh 2006; Zaloudek and Reilly 1982). The construction and operation of compressed air energy storage plants have less of an environmental impact and similar land use compared to conventional electrical generating facilities. In addition, locating a compressed air energy storage project is more flexible than a pumped hydro storage (Beckwith and Associates 1983).

An ideal gas compressed in isothermal conditions has an energy density e_V [kJ/m^3] that is a function of the cycle's minimum and maximum pressures P_{min} and P_{max} [kPa],

$$e_V = P_{\max} \ln\left(\frac{P_{\max}}{P_{\min}}\right) \tag{3.7}$$

For instance, the energy density in air compressed from P_{min} = 4 MPa to P_{max} = 7 MPa is e_V = 4 MJ/m^3. The energy density of an isothermal compressed air system is plotted versus the maximum air pressure for two efficiency values in Figure 3.2. Moreover, the energy density of the existing compressed air energy storage power plants is shown in the range of working pressures.

Consider a hollow foundation of volume V = 2 m^3 and compressed air pressure ranging from P_{min} = 0.1 MPa (atmospheric pressure) to P_{max} = 8 MPa. The energy density is e_V = 35 MJ/m^3 (Eq. 3.7). From Eq. (3.1), and assuming a recovery efficiency η = 0.75, the energy stored is 53 MJ. Taking a house power consumption of 2 kW, this distributed compressed air energy storage can provide 7.3 hours of power supply.

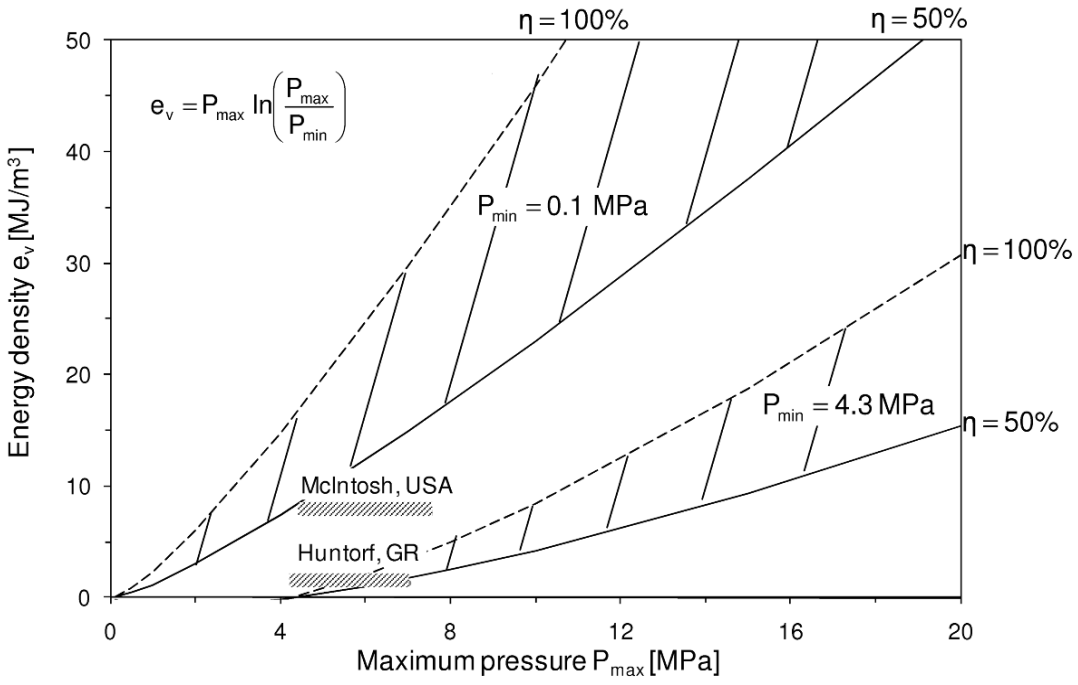

Figure 3.2 Energy density of compressed air in isothermal conditions. The energy density is a function of the maximum P_{max} and minimum P_{min} storage pressures, and the recovery efficiency η. Dotted and continuous lines represent 50 and 100% efficiency, respectively. The energy density of the CAES projects shown was calculated dividing their energy output (total electric energy minus the thermal energy used in the generation stage) by the total volume of the salt caverns.

Various underground storage concepts have been considered for compressed air projects including solution-mined salt caverns, excavated rock caverns, existing porous rock formations, and abandoned limestone or coal mines. Salt domes can be economically excavated by solution mining (Allen et al. 1982b). Moreover, these formations tend to be homogeneous, impermeable, and self-healing (Chan et al. 2000; Fuenkajorn 2006; Munson et al. 1999). The only two operating compressed air energy storage power plants in the World operate in salt caverns. One is installed in Huntorf, Germany (Crotogino et al. 2001) and the other is in McIntosh, Alabama, U.S. The operating air pressure ranges between 4 MPa and 7 MPa. The air temperature and

relative humidity increase during compression (Landsbaum et al. 1955). Moisture, temperature, and the in-situ geothermal gradient determine the creep behavior of the salt rock (Note: air may be dried before storage). Salt caverns may fail due to creep, cavern roof collapse, subsidence, loss of cavern integrity, leakage, and salt fracture. These failure mechanisms must be considered to design the cavern geometry (e.g., shape, depth, diameter, height, and separation distance) and to define operational variables, such as the working pressure, the loading/unloading rate, and the air flux humidity (Allen et al. 1985; Thoms and Martinez 1978).

Hard rock caverns involve expensive mining processes. Thus, some abandoned mines have been evaluated for potential storage (EPRI-DOE 2003). In fact, an abandoned mine in a limestone formation with a shale caprock will be used as a storage reservoir in Ohio, U.S. This power plant will generate 2700 MW with a 30 hr supply duration (van der Linden 2006). Hard rock caverns can sustain larger air pressure fluctuations (e.g., 7 and 8 MPa). Their design must account for fluctuations of the phreatic level and the chemical composition of the underground water, changes in the rock strength, the development of fractures and sliding blocks, and thermo-chemo-mechanical weakening of the rock mass (Allen et al. 1982a). Typical requirements for the host rock are low permeability ($<10^{-8}$ m/s), limited faulting and jointing to prevent instability and air leakage, thermal stability between 4 to 80 °C, unconfined compressive strength larger than 25 MPa, limited creep and shrink/swell to control unexpected jointed rock behavior, and in-situ stress anisotropy smaller than 1.5 (Allen et al. 1982a).

Injected compressed air in aquifers displaces the in-situ underground water, which later provides the reaction pressure to recover the compressed air. This scheme can be regarded as a constant volume system because the movement of the air-water interface is negligible for daily cycles compared to the initial displacement of the interface (Allen et al. 1983; Katz and Lady 1976). An appropriate underground reservoir requires large dimensions (e.g., the generation of 200 MW in 8 hours requires a 16 ha x 100 m

reservoir), the presence of a confined aquifer, an impermeable cap rock, compatible underground water regime, high porosity, and high permeability of the rock formation (Allen et al. 1983). A new compressed air energy storage power plant is under development in a sandstone aquifer with these characteristics in Iowa, U.S. (Fortner 2008). Fast, cyclic, multidirectional fluid flow, mixed fluid composition, and cyclic loading take place in the reservoir during operation. These processes can result in cementation loss, fines production, migration and clogging, accelerated dissolution, and mineral precipitation and oxidation. Anticipated problems include the enhancement of wellbore corrosion due to biological activity; turbo-machinery damage due to fine sand production and migration; and changes in permeability, corrosion, and flammability due to the presence of residual hydrocarbons (Katz and Lady 1976).

The long-term performance of mechanical energy geo-storage systems requires continuous monitoring of the storage integrity. Volume reduction and subsidence induced by creep in salt caverns (Bérest and Brouard 2003; Munson and Myers 2000; Wierczeyko 1983), and leakage of the stored substance caused by changes in hydraulic conductivity (Bérest et al. 2007; Fossan 1979; Hinkebein et al. 1995) can be identified and mitigated with proper monitoring.

3.2.3 Stored Energy in Waste

Biomass accounts for nearly 65% of the total municipal solid waste stream in the U.S (including paper, food scraps, wood, and yard trimmings) (EPA 2009). Biomass can be converted into energy through thermochemical, biochemical, and physicochemical methods (Williams 2007). Thermochemical conversion methods are suitable for low moisture-content materials and include combustion (incineration), gasification, and pyrolysis.

Table 3.3 Higher Heating Calue of Waste Materials

Type of municipal solid waste	Higher heating value HHV [MJ / kg]
Paper/cardboard	16
Food	4.2
Leaves and grass	6
Other organics	8.5
Construction and demolition lumber	17
Prunings, trimmings, branches, and stumps	11.4
All non-film plastic	22
Film plastic	45
Textiles	17.4
Hydrogen	142

Note: Higher heating values of waste as received. Values in Williams et al. (2003)

The potential energy density of waste e_V [kJ/m^3] regarding combustion can be quantified using the higher heating value *HHV* [kJ/kg] of the burnt waste multiplied by its mass density ρ [kg/m^3]

$$e_V = HHV \cdot \rho \tag{3.8}$$

Higher heating values of some generic waste materials are listed in Table 3.3. For a mass density ρ = 1200 kg/m^3 (Zekkos 2005) and a higher heating value *HHV* = 11 [MJ/kg] (based on the composition of municipal solid waste), the energy density of municipal solid waste is about e_V = 13200 MJ/m^3.

Biochemical conversion methods are recommended for high moisture-content materials and include anaerobic digestion, aerobic conversion, and anaerobic fermentation. Both methods produce gas, which is later used to generate electricity or is

converted into a biofuel, such as methane or ethanol. The potential ethanol extractable from paper/cardboard and wood & green is approximately 0.3 m^3 per dry ton of biomass. This estimation assumes that 50% of paper/cardboard and 40% of wood & green from the landfill stream can be recovered for fuel production (Williams 2007).

3.2.4 Capacity and Cost Analysis

The design of an energy storage system accounts for the required energy E [kJ], the power P [kW], the time duration of supply t [s], the available volume V [m^3], and the energy density e_v [kJ/m^3] according to Eq. (3.1). Table 3.4 provides simple guidelines to estimate the energy density, the energy stored, the power delivered, and the costs of various energy storage systems. In addition, Figure 3.3 highlights the energy stored and the power capacity of existing compressed air energy storage and pumped hydro storage power plants compared to other distributed storage systems.

Table 3.4 Energy Storage Systems: Guidelines to Estimate Energy Density, Power, and Cost

System	**Energy density** $\mathbf{e_V}$ [kJ/m^3]	**Costs** $\mathbf{C_C}$
Sensible Heat Storage	$\rho \cdot C_p \cdot \Delta T$ Eq. (3.3)	Storage material Underground space Heat exchanger system
Latent Heat Storage	$L \cdot \rho$ Eq. (3.4)	
Pumped Hydro Storage (PHS)	$\gamma \cdot \Delta H$ Eq. (3.5)	Energy capacity Power capacity Balance of plant Power conversion Fuel/electricity Operation and maintenance
Compressed Air Energy Storage (CAES)	$P_{\max} \ln\left(\frac{P_{\max}}{P_{\min}}\right)$ Eq. (3.7) (isothermal conditions)	
Stored energy in waste	$HHV \cdot \rho$ Eq. (3.8)	Containment space Lining and cover system Gas recovery system

Notes: (1) Stored energy $E = V \cdot e_V$, where V is the volume of the energy storage system
(2) Power $P = E / t$, where t is the supply time duration
(3) Reference costs for CAES and PHS in Bradbury (2010), and Schoenung and Hassenzahi (2003)

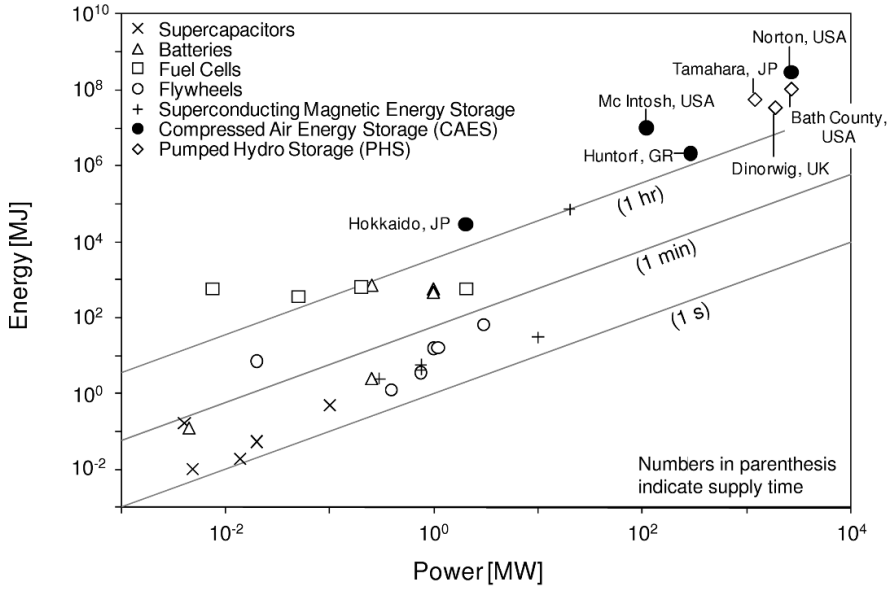

Figure 3.3 Energy and power capacity of storage systems (Based on Schoenung 2001 with additional data from EPRI-DOE 2004, Electricity Storage Association, Power Plants Around the World, and First Hydro Company)

Various energy storage alternatives are compared using the levelized annual cost (Masters and Wiley 2004; Schoenung and Hassenzahi 2003). The levelized annual cost *LAC* [$/kW/yr] is estimated with the fixed charge for capital equipment C_{FC} [$/kW/yr], the levelized fixed operation and maintenance costs C_{OM} [$/kW/yr], the levelized cost for replacement parts C_{RP} [$/kW/yr], and the levelized costs for energy generation C_{EG} [$/kW/yr] according to

$$LAC = C_{FC} + C_{OM} + C_{RP} + C_{EG} \tag{3.9}$$

The fixed charge for capital equipment is calculated with the fixed charge rate *FCR* [1/yr] and the total capital cost C_C [$/kW]

$$C_{FC} = FCR \cdot C_C \tag{3.10}$$

Given the required time duration of supply *t* [s], the total capital cost C_C [$/kW] is estimated using the energy storage cost C_E [$/kJ], the power cost C_P [$/kW], the balance

of plant costs C_{BOP} [$/kW], which includes the cost of the components and structures not considered in the other costs, and the power conversion system costs C_{PCS} [$/kW] (Bradbury 2010; EPRI-DOE 2003; Schoenung and Hassenzahi 2003):

$$C_C = C_E \cdot t + \left(C_P + C_{BOP} + C_{PCS}\right) \tag{3.11}$$

Figure 3.4 provides estimates of energy and power capacity costs for various energy storage systems.

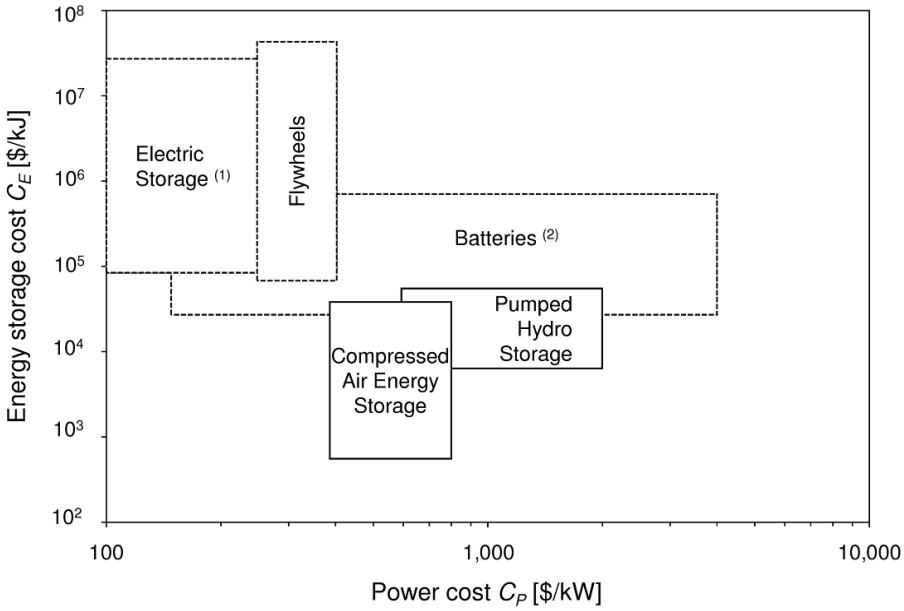

Figure 3.4 Energy and power costs for various energy storage systems. Note: (1) electric storage includes standard electrostatic capacitors, electrochemical capacitors, and superconducting magnetic energy storage; (2) batteries include conventional, molten salt, lead-acid, and flow batteries (Data from Bradbury 2010).

The levelized fixed operation and maintenance costs are computed with the fixed operation and maintenance cost C_{OMF} [$/kW/yr] and the levelizing factor for operation and maintenance cost LF_{OM} [-]

$$C_{OM} = C_{OMF} \cdot LF_{OM} \tag{3.12}$$

The levelized cost for replacement parts is calculated using the annualized replacement cost C_{AR} [$/kW/yr] and the levelizing factor for operation and maintenance cost

$$C_{RP} = C_{AR} \cdot LF_{OM} \tag{3.13}$$

Finally, the levelized costs for energy generation includes the cost of fuel and electricity charge

$$C_{EG} = \left(C_{fuel} \cdot HR \cdot LF_{fuel} + C_{el} \cdot \frac{1}{\eta_{el}} \cdot LF_{el} \right) \cdot t_{year} \tag{3.14}$$

where C_{fuel} is the unit cost of fuel [$/kJ], HR is the heat rate [kJ/kJ], LF_{fuel} [-] is the levelizing factor for fuel, C_{el} is the unit cost of input electricity [$/kJ], η_{el} [kJ_{out}/kJ_{in}] is the storage efficiency, LF_{el} [-] is the levelizing factor for electricity, and t_{year} [s/yr] is the annual operation time (Schoenung and Hassenzahi 2003). The variable operation and maintenance cost C_{OMV} [$/kWh-delivered] is generally neglected for energy storage systems (Bradbury 2010).

The levelizing factors are calculated with the real discount rate d [-], the equivalent discount rate d' [-], and the levelization period n [-] (Masters and Wiley 2004)

$$LF = \left[\frac{(1+d')^n - 1}{d' \cdot (1+d')^n} \right] \cdot \left[\frac{d \cdot (1+d)^n}{(1+d)^n - 1} \right] \tag{3.15}$$

The equivalent discount rate is calculated with the total escalation rate e_T [-]

$$d' = \frac{1+d}{1+e_T} - 1 \tag{3.16}$$

The total escalation rate is a function of the real escalation rate e_R [-] and the inflation rate i_R [-] (Drbal et al. 1996)

$$e_T = (1+i_R) \cdot (1+e_R) - 1 \tag{3.17}$$

Figure 3.5 compares the average levelized annual cost of compressed air energy storage, pumped hydro storage, lead-acid batteries, and flywheel energy storage obtained following the described methodology. The results indicate that levelized annual costs of

compressed air energy storage and pumped hydro storage are lower than those of other systems for discharge times longer than two hours.

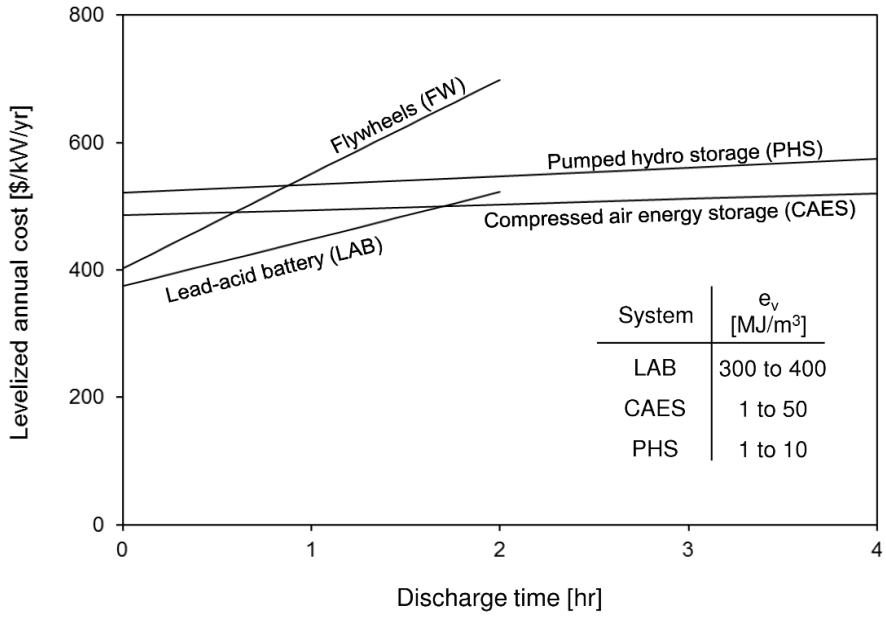

Figure 3.5 Average levelized annual cost of energy storage systems. Flywheels and lead-acid batteries have less than two hours of discharge time according to Figure 3.3 (Data from Bradbury 2010; Schoenung and Eyer 2008; and Schoenung and Hassenzahi 2003).

3.3 Geotechnical Implications: Cyclic Response of Geo-materials

The long-term performance of energy geo-storage systems depends on the cyclic behavior of geo-materials. Periodic storage and release exert cyclic changes in effective stress, temperature (including freeze-thaw), and relative humidity (wetting and drying). In this section, the main characteristics of the behavior of geo-materials under cyclic excitations are discussed. Table 3.5 summarizes the type and the frequency of possible cyclic excitations, and anticipates emergent phenomena caused by coupled processes for every storage system.

Table 3.5 Energy Storage Systems, Frequency and Type of Excitation

System	Frequency	Cyclic excitation	Coupled processes and emergent phenomena
Compressed Air Energy Storage (CAES)	Daily	Effective stress Temperature Relative Humidity	- Cyclic air flow causes fines production and migration clogging aquifers - Warm, compressed air enhances creep in salt cavern
Pumped Hydro Storage (PHS)	Daily/Seasonal	Effective stress Wet-dry	- Water flow through rock joints dissolves filling materials
Geothermal Heat Pump (GHP)	Daily	Temperature Relative Humidity	- Heat front dries soil reducing thermal conductivity - Vapor migration induces hygrothermal stresses
Sensible Heat Storage	Daily	Temperature	- Substance thermal expansion induces stress in heat exchanger system
Latent Heat Storage	Daily/Seasonal	Temperature Freeze/thaw	- Substance thermal expansion induces stress in container and heat exchanger system - Storage substance induces chemical stresses on geomaterials
Stored energy in waste	Months - years	Depends on the method	- Gas migration and fluid percolation induces dissolution of geomaterials and chemical stresses

3.3.1 Effective Stress Cycles

The change in effective stress around an underground cavern in an elastic medium as a result of cycles of internal pressure is illustrated in Figure 3.6. The figure shows the mean and shear stress fields and the stress path of two points as the internal pressure increases from 4.5 MPa to 7 MPa.

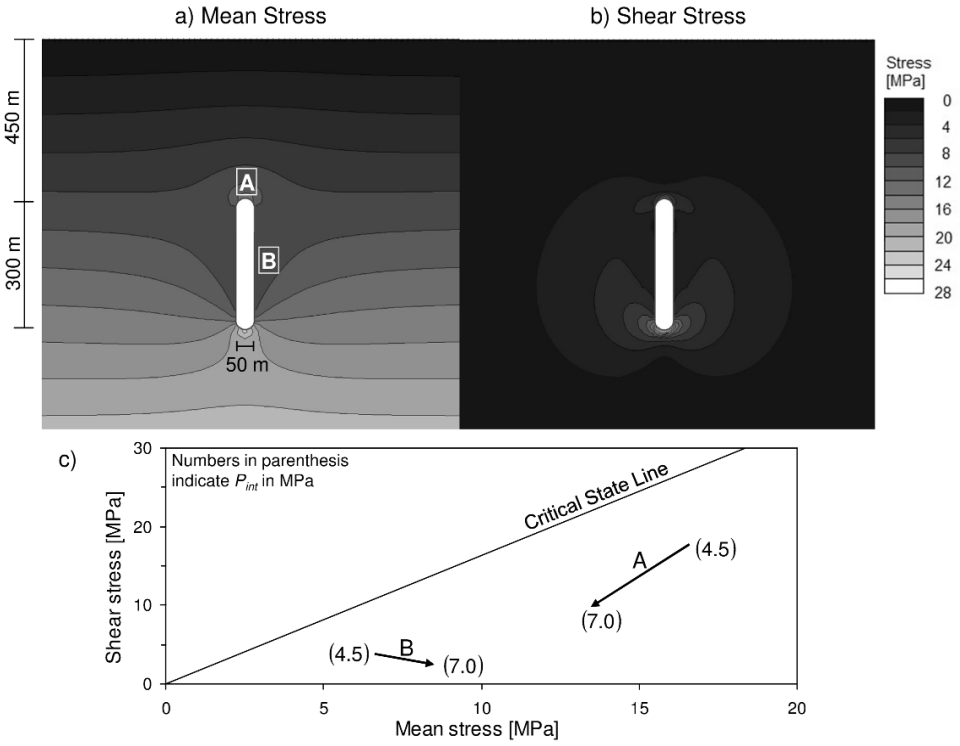

Figure 3.6 Underground cavity in elastic medium subjected to cyclic internal pressure P_{int} from 4.5 to 7 MPa. (a) Mean stress and (b) shear stress for internal pressure of 7 MPa. (c) Stress paths of points A and B. Stress field computed using a gravitational stress field and plane strain conditions. Simulated conditions correspond to McIntosh salt cavern.

The material response to cyclic loading can be described within the framework of the shakedown theory, which includes elastic response; elastic shakedown; plastic shakedown, or alternating plasticity; and ratcheting, or incremental collapse (Koiter 1960; Melan 1938; Sharp and Booker 1984).

The elastic response refers to low-magnitude loads that do not cause plastic deformation, i.e., the strain level is below the linear threshold strain (Dobry and Swiger 1979; Vucetic 1994). Even in the small strain regime, the impact of repetitive loading on material properties and long-term behavior can be detrimental if the number of cycles is large. Elastic shakedown refers to loads above the "elastic limit load" and below the "shakedown limit load." In this regime, plastic deformation develops during a finite

number of early cycles; thereafter, the material recovers elastically. If the applied load is larger than the shakedown limit, the material reaches a stable hysteretic cycle of deformation after several cycles of permanent deformation. This state is called "plastic shakedown," or "alternating plasticity." Finally, ratcheting, or incremental collapse, is a process in which the material continues to accumulate plastic deformation under loads larger than the shakedown limit and the material cannot adapt to cyclic loading. The long-term behavior of a system subjected to cyclic loading is determined by its ability to reach a state of shakedown.

The average state of stress, the imposed strain amplitude, the initial density, and the characteristics of the geo-material determine its long-term behavior under cyclic loading (Wichtmann 2005). Figure 3.7 depicts the development of shear and volumetric strains during cyclic drained loading. Soil elements with an initially high stress obliquity mostly exhibit shear strain whereas elements subjected to an initial isotropic stress condition mainly develop volumetric strain. The figure also emphasizes that soil elements with high stress obliquity exhibit ratcheting in the long-term. In all cases, sediments reach a terminal density under repetitive loading (Narsilio and Santamarina 2008).

Rocks subjected to cycles of effective stress may experience fatigue as shown in the stress-number of cycle space in Figure 3.8. As the cyclic stress amplitude increases, the number of cycles required to cause failure decreases (Haimson 1978; Scholz and Koczynski 1979; Xiao et al. 2010). Fatigue in rocks is related to the development of intergranular cracks and their growth in preferential orientations (Kobayashi et al. 2009). It is enhanced by the presence of pre-existing cracks (Prost 1988), and it is usually accompanied by volumetric strain, which is a function of the confining stress (Hadley 1976; Scholz and Koczynski 1979; Zoback and Byerlee 1975). When the rock is saturated, the opening and closing of cracks and the variation of porosity generates changes in pore-fluid pressure (Tien et al. 1990).

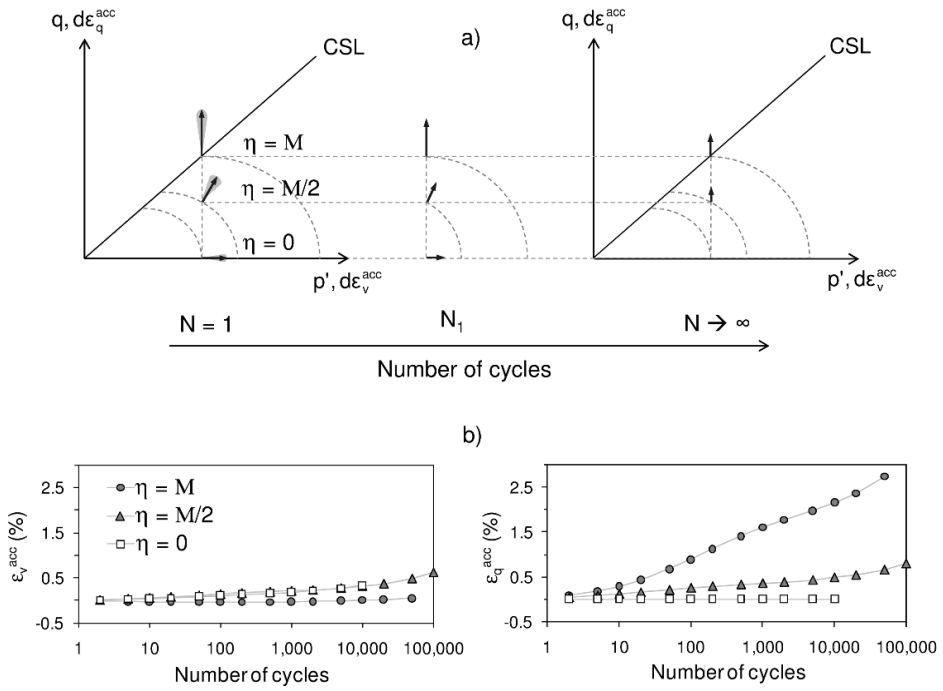

Figure 3.7 Cyclic behavior of granular materials. (a) Schematic representation of the increments of volumetric ε_v^{acc} and shear strain ε_q^{acc} with the number of cycles for soil elements at three different average state of stress. The arrows represent the direction and magnitude of the accumulated strain. (b) Measured accumulated volumetric and shear strain in sand with the number of cycles for each average state of stress (Data from Wichtmann 2005)

3.3.2 Temperature Cycles

A temperature change can cause sediment consolidation (Campanella and Mitchell 1968; Towhata et al. 1993), swelling, an increase in pore water pressure (Abuel-Naga et al. 2007), a decrease in strength, and creep (Demars and Charles 1982). Water drainage takes place if the rate of temperature increase and volume expansion is lower than the rate of drainage. Otherwise, temperature increase induces excess pore water pressure. The sediment response is analogous to consolidation due to changes in effective stress (Figure 3.9a), and high plasticity soils are more sensible to temperature changes (Demars and Charles 1982). When the temperature decreases, water and mineral volume contraction trigger suction and water absorption.

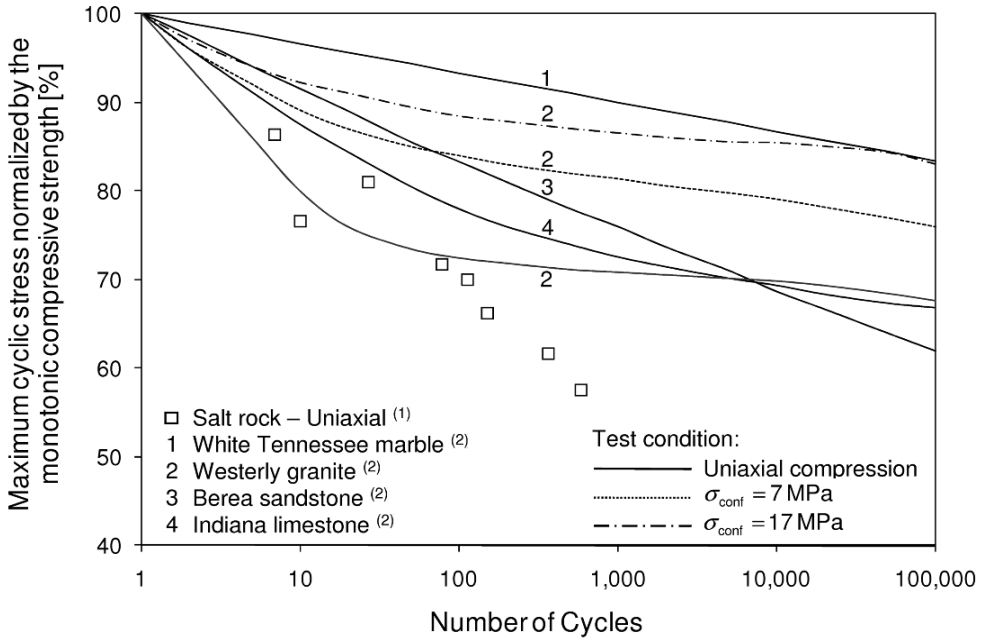

Figure 3.8 Fatigue strength of various types of rock subjected to cyclic loading in uniaxial and triaxial compression. Note: data from (1) Fuenkajorn and Phueakphum (2010); and (2) Haimson (1978).

Subjecting a soil to cyclic thermal loading is similar to overconsolidation. Even though the volume change induced by the first cycle is more pronounced than the change induced by subsequent ones, cyclic thermal excitation can cause damage accumulation in the long-term. In particular, thermal cycles can lead to thermal ratcheting (Carson 2000; Carson and Holmes 2003) and the gradual rearrangement of grains due to differential thermal expansion (Chen et al. 2006).

Mineral heterogeneity and different thermal expansion may cause damage accumulation in rocks subjected to thermal cycles (Figure 3.9b). A transition from brittle to ductile behavior is expected (Tullis and Yund 1977). In jointed rocks, temperature cycles enhance relative movement of the joint faces and affect the properties of the filling materials (Thirumalai and Demou 1974; Wong 1982).

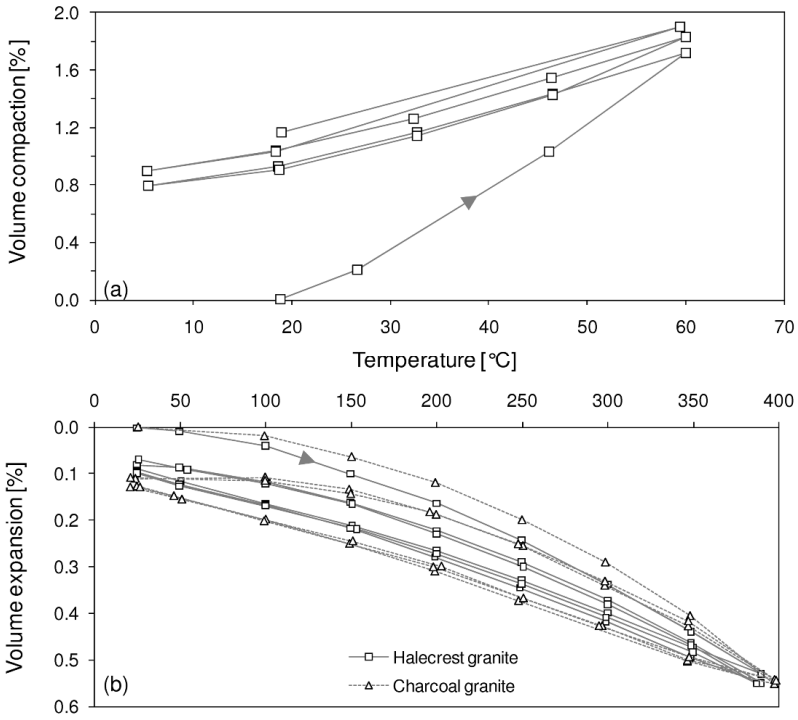

Figure 3.9 Thermal cycling on geo-materials. (a) Sediments: consolidation of remolded illite (Campanella and Mitchell 1968). (b) Rocks: expansion of granite (Thirumalai and Demou 1974).

3.3.3 Freeze-Thaw Cycles

Freeze-thaw cycles exacerbate the effects of thermal cycling. Most sediments experience volume expansion during freezing and consolidation after thawing, resulting in net volume contraction. Sediments eventually reach a residual void ratio after a certain number of freeze-thaw cycles regardless of the initial void ratio (Viklander 1998b). In addition, freeze-thaw cycles enhance particle segregation (Viklander 1998a; Viklander and Eigenbrod 2000).

Other consequences of freeze-thaw cycles are changes in permeability (Eigenbrod 1996; Viklander 1998b), liquid limit, grain size distribution (Qi et al. 2006), consolidation behavior (Graham and Au 1985), shear strength (Leroueil et al. 1991), and stiffness (Simonsen et al. 2002).

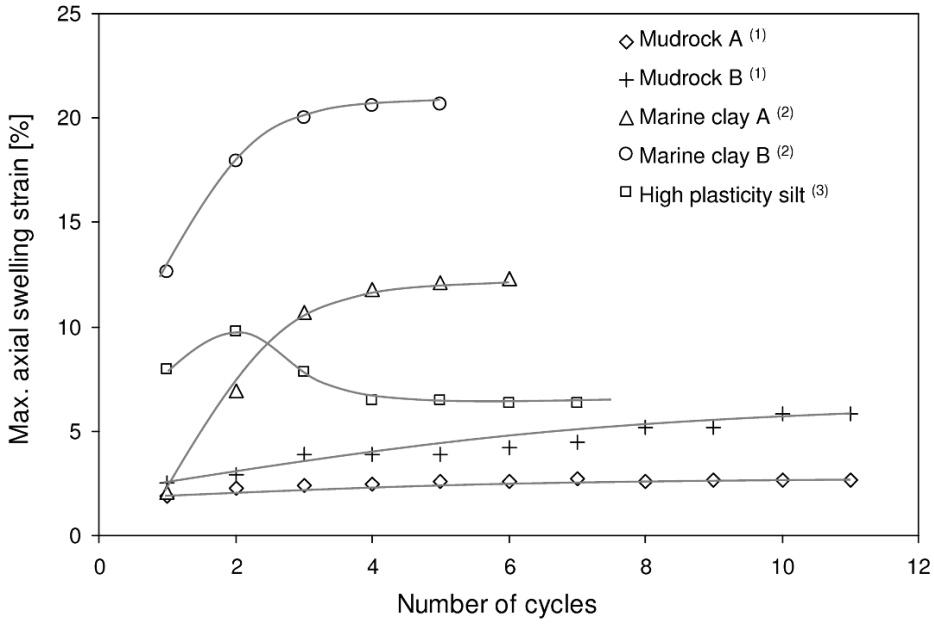

Figure 3.10 Maximum axial swelling strain of sediment and mudrock samples subjected to wet-dry cycles. Mudrock and marine clay samples tested in odometer cells under free swelling conditions. High plasticity silt tested in odometer cells with vertical surcharge of 50 kPa. Note: data from (1) Pejon and Zuquette (2002), (2) Osipov et al. (1987), and (3) Tripathy and Subba Rao (2009).

3.3.4 Wet-Dry Cycles

Fine grained sediments subjected to wet-dry cycles develop volumetric swell/shrink changes. Eventually, these volumetric changes can lead to plastic deformations and desiccation cracks (Albrecht and Benson 2001; Boardman and Daniel 1996; Herrera et al. 2007; Lin and Benson 2000).

Specific surface determines the pore size and the suction magnitude in fine grained soils. The matric suction (u_g - u_w)[Pa] can be calculated with the surface tension T_s [N/m], the mass density of the soil particle ρ_s [kg/m^3], the void ratio e, and the specific surface S_s [m2/kg]

$$u_g - u_w = \frac{T_s \cdot S_s \cdot \rho}{e} . \tag{3.18}$$

Suction and stiffness M [Pa], which is mainly controlled by compaction, determine the strain amplitude

$$\varepsilon_{amplitude} = \frac{u_g - u_w}{M} \tag{3.19}$$

Most volumetric changes occur during the first few wet/dry cycles (scaly clays in Farulla et al. 2007; and expansive soils in Tripathy and Subba Rao 2009, and Tripathy et al. 2002). Clay rocks, such as shales, also experience swelling due to the hydration of clay minerals, which are more susceptible to expansion (Harper et al. 1979). Figure 3.10 illustrates the vertical strain of soil and rock samples subjected to wet-dry cycles in odometer cells.

3.4 Conclusions

The increase in both energy demand and the use of intermittent renewable energy sources underscores the need for energy storage. Surplus electric power generated from fossil fuels or renewable energy must be stored as high-grade energy (e.g., mechanical and electric energy).

Energy geo-storage provides multiple alternatives for the storage of surplus electric power. The cost analysis of energy geo-storage systems indicates that mechanical energy storage, such as compressed air and pumped hydro, is suitable for large scale power systems since it has a lower levelized annual cost for high discharge times compared to batteries, flywheels, and electric storage systems.

Nominal energy density values for typical storage implementations rank as follows: 100 to 300 MJ/m^3 for latent heat, 10 to 300 MJ/m^3 for sensible heat, 1 to 50 MJ/m^3 for compressed air, and 1 to 10 MJ/m^3 for elevated water. Although thermal heat storage can reach higher energy densities, energy recovery is limited by the Carnot efficiency.

A compressed air energy storage system uses less volume than an equivalent pumped hydro storage system because higher energy density can be achieved in compressed air than in elevated water under typical conditions. In addition, the underground space of compressed air energy storage has a lower environmental impact.

Thermal energy storage either as sensible or latent heat is recommended when the available surplus energy is heat. These systems can be coupled with solar water/air heating systems. Under volume restrictions, latent heat systems are preferred because of their higher energy densities in the range of working temperatures.

It is worth noting that distributed geo-storage systems may also satisfy economic criteria, especially thermal energy storage systems. Distributed compressed air energy storage is limited by its low energy density compared to batteries and its higher levelized annual cost at low discharge times.

Energy geo-storage systems exert cyclic changes in effective stress, temperature (including freeze-thaw), and moisture on geo-materials. Although these excitations may not cause monotonic failure, their repetitive application can gradually deteriorate the properties of geo-materials and affect the long-term performance of geo-storage systems. Shakedown and ratcheting behavior can be developed in long-term cyclic storage systems.

The use of energy geo-storage systems enhances conventional power generation and optimizes the use of renewable energy sources. Therefore, energy geo-storage must be considered as an integral component of a sustainable energy strategy.

CHAPTER 4

MODELING THE LONG-TERM BEHAVIOR OF GRANULAR MATERIALS

4.1 Introduction

The repetitive action of cyclic boundary loads can induce volumetric and shear strain accumulation on granular materials. Cumulative deformations reflect the static and cyclic stress fields, drainage and frequency effects, and the number of repetitions.

The long-term behavior of granular materials subjected to repetitive boundary conditions can be modeled using classical constitutive models. Examples of mechanical models that describe the complete stress-strain response of a material include bounding surface plasticity (Dafalias and Herrmann 1986), kinematic hardening (Mróz 1967), generalized plasticity (Zhang et al. 2001), and combined formulations (Gajo and Muir Wood 1999). Constitutive models with irreducible plastic potentials during unloading are not suitable to simulate strain accumulation because of their inability to predict plastic strain upon re-loading. In general, the use of classical constitutive models requires major computational resources, and the accumulation of numerical errors may overwhelm the predicted deformations when the number of load repetitions is high (Niemunis et al. 2004).

Alternatively, empirical strain accumulation functions fitted to cyclic test results have been proposed to predict the accumulated strain for the imposed cyclic stress as a function of the number of load cycles. Accumulation functions can be divided into three groups: (1) equations that describe one component of the accumulated strain as a function of the first load cycle, the number of cycles, the static state of stress, and the initial density (Diyaljee and Raymond 1982; Gidel et al. 2001; Lentz and Baladi 1981;

Sawicki and Swidzinski 1989; Sweere 1990; Tseng and Lytton 1989); (2) equations that predict one component of the accumulated strain at a reference number of cycles N_{ref} as a function of the state of stress, the initial void ratio, and the static shear strength (Barksdale 1972; Brown 1974; Lekarp and Dawson 1998; Lentz and Baladi 1980); and (3) equations that predict the complete evolution of strain accumulation (i.e., magnitude and direction) as a function of the number of cycles, the state of stress, and the initial density (Bouckovalas et al. 1984; François et al. 2010; Kaggwa et al. 1991; Marr and Christian 1981; Niemunis et al. 2005; Suiker and de Borst 2003). While strain accumulation functions are stable, their application is restricted to simple boundary conditions.

This study advances more stable long-term deformation accumulation analyses to study the long-term response of geotechnical structures subjected to repetitive loading using a hybrid approach that combines a classical mechanical constitutive model with empirical strain accumulation functions. The mechanical constitutive model is used to analyze the static load, the first load cycle, and to satisfy equilibrium and compatibility during repetitive loading. In addition, empirical strain accumulation functions are invoked to estimate strain accumulation during repetitive loading. This chapter starts with a review of soil behavior under repetitive mechanical loading, followed by a description of the proposed numerical scheme and field examples.

4.2 Soil Behavior under Repetitive Loading

The analysis of the long-term response of geotechnical systems subjected to repetitive loading is fraught by the large number of variables involved and by constitutive parameters that are difficult to calibrate. This study seeks to develop a robust numerical scheme with a limited number of parameters that properly reflects salient features of soil behavior under repetitive loading.

4.2.1 Threshold Strains

Particle-level deformation mechanisms change with strain level. If the cyclic strain level is below the elastic threshold strain, the soil deforms at grain contacts without slippage (Dobry and Swiger 1979; Santamarina et al. 2001). In contrast, the soil undergoes particle rearrangement and fabric changes when the strain level exceeds the volumetric threshold strain. At this strain level, the soil experiences either plastic volumetric strain in drained conditions or changes in pore pressure in undrained conditions (Vucetic and Dobry 1991).

4.2.2 Ratcheting, Shakedown, and Terminal Density

The long-term response of geomaterials subjected to repetitive loading can be characterized by either ratcheting or shakedown behavior. Ratcheting is the sustained long-term accumulation of shear strain upon repetitive loading; typically, it develops under high stress obliquity (Alonso-Marroquin and Herrmann 2004). In contrast, when strain accumulation decreases towards an asymptotic value (i.e., the plastic strain increment per cycle becomes null), the soil reaches a stable deformation state known as shakedown (Garcia-Rojo and Herrmann 2005).

When the initial cyclic strains are larger than the elastic threshold strain, the soil fabric gradually evolves towards a statistically stable structure characterized by its terminal density, or terminal void ratio (Narsilio and Santamarina 2008). The terminal density is process-dependent and sets the upper bound for volumetric strain accumulation. Note that terminal density is reached in both ratcheting and shakedown behavior, even if the material experiences particle breakage during repetitive loading.

4.2.3 Cyclic Response in the Stress-Strain-Volume Space

The behavior of a granular material subjected to cyclic stress-controlled loading in triaxial conditions is schematically shown in Figure 4.1a. The soil response is

characterized by the initial void ratio e_0, the initial static mean stress p_0 and deviatoric stress q_0, and the cyclic stress amplitude Δq (Note: Octahedral definitions $p = (\sigma_{11} + \sigma_{22} + \sigma_{33})/3$ and $q = (3/2)^{1/2} [(\sigma_{11} - p)^2 + (\sigma_{22} - p)^2 + (\sigma_{33} - p)^2 + 2(\sigma_{12})^2 + 2(\sigma_{13})^2 + 2(\sigma_{23})^2]^{1/2}$ are adopted). The conceptual trends in Figure 4.1a show high plastic deformation induced by the first load cycle, gradual strain accumulation in every cycle, a relatively constant elastic component of the deformation (q - ε_1 quadrant), and the soil asymptotically approaching terminal density ($e - p'$ and e - ε_1 quadrants).

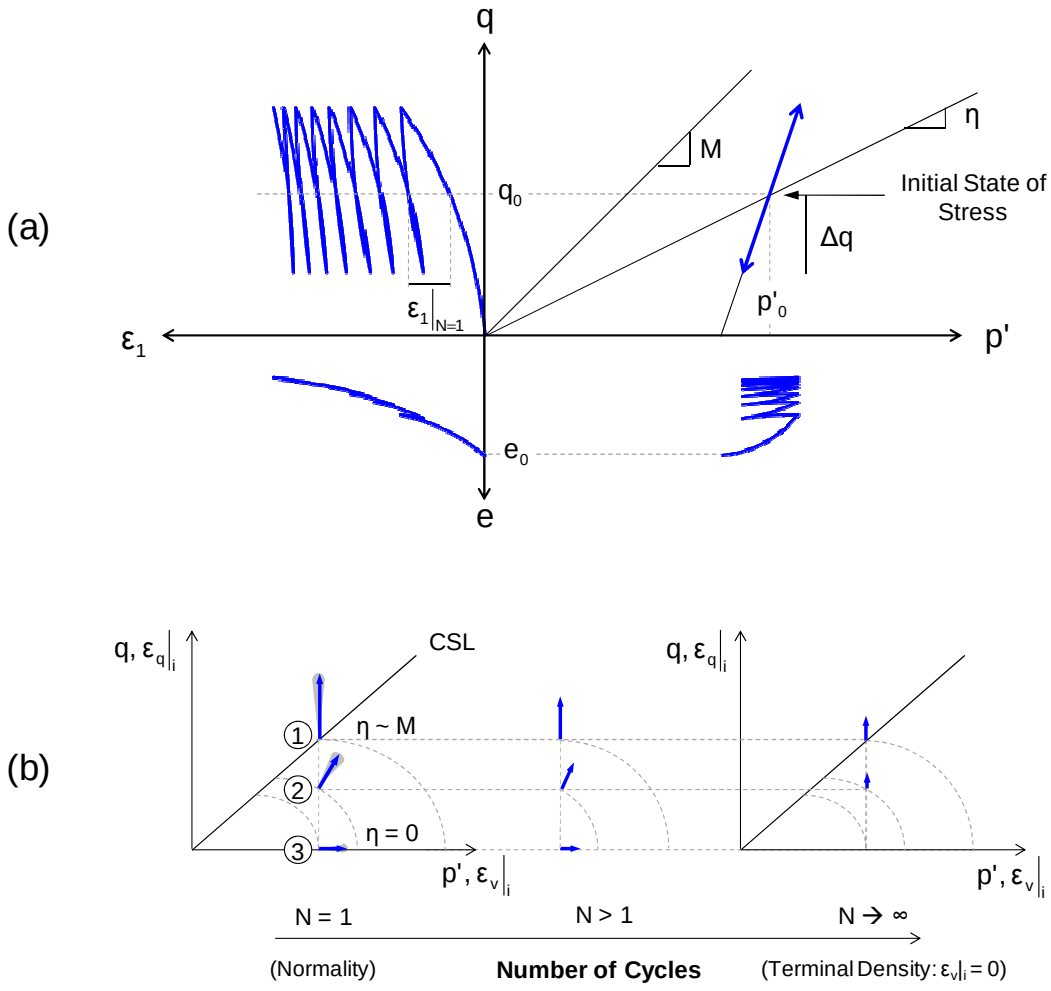

Figure 4.1 Behavior of a granular material subjected to drained cyclic triaxial loading. (a) Evolution of effective mean stress p', deviatoric stress q, axial strain ε_1, and void ratio e. (b) Evolution of the strain increment per cycle with the number of load cycles.

Figure 4.1b depicts the evolution of the strain increment per cycle as a function of the number of load cycles for soil elements subjected to three different initial stress obliquities $\eta_0 = q_0/p_0'$. The arrows represent the incremental strain vector per load cycle. The horizontal and vertical components reflect the volumetric $\varepsilon_v|_i$ and the shear $\varepsilon_q|_i$ strain changes per cycle. The strains in the first load cycle, $\varepsilon_v|_{N=1}$ and $\varepsilon_q|_{N=1}$, are assumed normal to the monotonic plastic potential, such as the modified Cam Clay yield surface shown in the figure. This approximation has been confirmed for a wide range of granular materials (Chang and Whitman 1988; Lackenby 2006; Suiker et al. 2005; Wichtmann et al. 2006; Wichtmann et al. 2009).

The soil element subjected to an initial state of stress close to the critical state line $\eta = M$ (shown as #1) accumulates mainly shear strain, and its increment per cycle gradually becomes constant as the number of cycles increases. In contrast, the soil element subjected to an initial nearly-isotropic state of stress (shown as #3) experiences mainly volumetric strain accumulation, and the strain increment per cycle goes to zero as the material approaches its terminal void ratio e_∞.

4.3 Numerical Modeling of Boundary Value Problems

A numerical scheme is developed herein to analyze geotechnical systems that experience long-term repetitive mechanical boundary conditions. The algorithm is framed within a finite-element formulation and considers soil behavior trends described above. Vectors are expressed in bold lower-case letters and matrices in bold upper-case letters.

4.3.1 Algorithm for Long-Term Repetitive Loading

The proposed algorithm involves 4 modules. These modules and the selected constitutive functions are described herein.

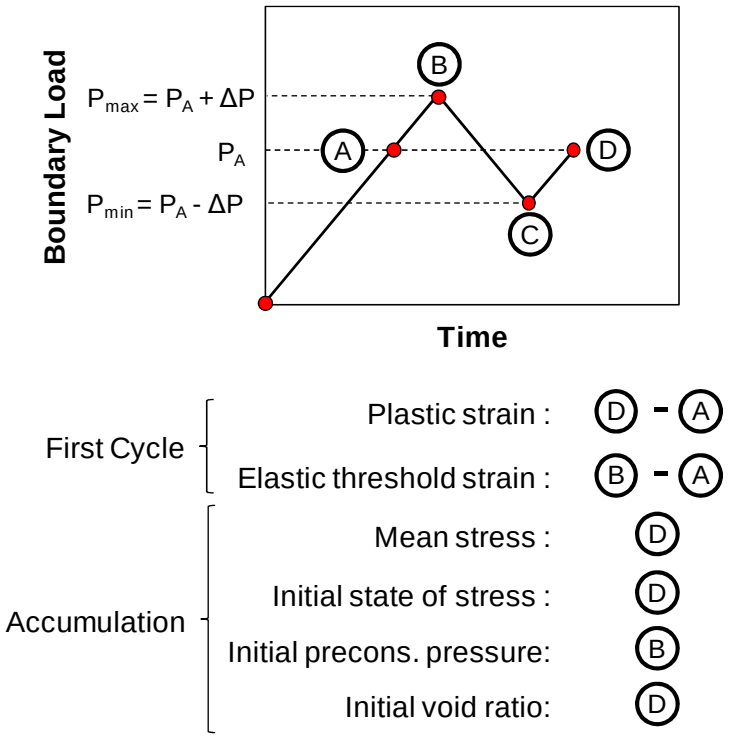

Figure 4.2 Computation scheme for the average load and the first cycle (Steps #1 and #2).

Module #1: Initial Static Condition

The stress field induced by self-weight and the initial static component of the applied load P_A are computed using the standard finite element method and a selected mechanical constitutive model (Figure 4.2). At every integration point, the computed static stress is $\boldsymbol{\sigma}_A$ and the corresponding strain is $\boldsymbol{\varepsilon}_A$.

Module #2: First Load Cycle

The first load cycle is computed with the same constitutive model used in the previous module. The following stress $\boldsymbol{\sigma} = (\sigma_{xx}, \sigma_{yy}, \sigma_{zz}, \tau_{xy}, \tau_{xz}, \tau_{yz})^T$ and strain $\boldsymbol{\varepsilon} = (\varepsilon_{xx}, \varepsilon_{yy}, \varepsilon_{zz}, \varepsilon_{xy}, \varepsilon_{xz}, \varepsilon_{yz})^T$ vectors are obtained at every integration point (T denotes the transpose):

- $\boldsymbol{\sigma}_B$ and $\boldsymbol{\varepsilon}_B$ at the maximum cycle load $P_{max} = P_A + \Delta P$ (Figure 4.2),

- $\boldsymbol{\sigma}_C$ and $\boldsymbol{\varepsilon}_C$ after unloading to the minimum load $P_{min} = P_A - \Delta P$, and
- $\boldsymbol{\sigma}_D$ and $\boldsymbol{\varepsilon}_D$ after reloading to the initial static load P_A.

Note that the modified Cam Clay model can be used only if the medium is normally consolidated or slightly overconsolidated after the initial static load so that the model can compute non-zero plastic strains for the first load cycle.

Subsequent load cycles will cause cyclic strain accumulation as long as the induced strain ($\boldsymbol{\varepsilon}_B - \boldsymbol{\varepsilon}_A$) exceeds the elastic threshold strain $\boldsymbol{\varepsilon}_{el}$, which is a function of soil type and the confining stress. The plastic strain at the end of the first cycle is

$$\boldsymbol{\varepsilon}^{D\text{-}A} = \boldsymbol{\varepsilon}_D - \boldsymbol{\varepsilon}_A . \tag{4.1}$$

Hence, the volumetric and shear strains at the end of the first cycle are

$$\varepsilon_v\big|_{N=1} = \boldsymbol{\varepsilon}_1 + \boldsymbol{\varepsilon}_2 + \boldsymbol{\varepsilon}_3\big|_{D-A} \tag{4.2}$$

and

$$\varepsilon_q\big|_{N=1} = \sqrt{\frac{2}{3}}\left[\left(\boldsymbol{\varepsilon}_1 - \frac{\varepsilon_v\big|_{N=1}}{3}\right)^2 + \left(\boldsymbol{\varepsilon}_2 - \frac{\varepsilon_v\big|_{N=1}}{3}\right)^2 + \left(\boldsymbol{\varepsilon}_3 - \frac{\varepsilon_v\big|_{N=1}}{3}\right)^2 + 2\left(\boldsymbol{\varepsilon}_4\right)^2 + 2\left(\boldsymbol{\varepsilon}_5\right)^2 + 2\left(\boldsymbol{\varepsilon}_6\right)^2\right]^{1/2}\Bigg|_{D-A} . \tag{4.3}$$

The strains at the end of the first cycle inherently reflect the combined effects of the initial effective stress and the initial void ratio, the cyclic stress amplitude and direction, and the sediment prior stress history. If the modified Cam Clay model is used, strains in the first cycle are compatible with experimentally observed cyclic flow directions, in particular, $\varepsilon_v|_{N=1}(\eta = M) = 0$ and $\varepsilon_q|_{N=1}(\eta = 0) = 0$.

Module #3: Strain Accumulation

The volumetric and shear strains that accumulate during repetitive cyclic loading are calculated using empirical accumulation functions. The selected functions are simple, mechanics-informed, and capture the main features of strain accumulation. Empirical equations for strain increments in the *i*-th cycle and for cumulative strains after the *N*-th cycle are described next.

Strain increments for the i-th cycle: The plastic volumetric strain per cycle vanishes as the sediment reaches terminal density while the one-cycle plastic shear strain evolves towards a constant value. Then, volumetric and shear strain increments in the *i*-th cycle are estimated as

$$\varepsilon_v\big|_i = \varepsilon_v\big|_{N=1}\left(\frac{a}{i}\right) \tag{4.4}$$

and

$$\varepsilon_q\big|_i = \varepsilon_q\big|_{N=1}\left(\frac{b}{i}+c\right), \tag{4.5}$$

where *a*, *b*, and *c* are constitutive parameters. The asymptotic values for i→∞ are $\varepsilon_v|_i = 0$ when the sediment reaches terminal density and ($\varepsilon_q|_{N=1} \cdot c$) for the plastic shear strain increment; the parameter $c > 0$ corresponds to an element that experiences ratcheting.

Cumulative strains after the N-th cycle: The accumulated shear and volumetric strains after the *N*-th cycle are obtained by integrating Eqs. (4.5) and (4.4) from 1 to *N*:

$$\varepsilon_q^{acc}\big|_N = \varepsilon_q\big|_{N=1}\left[1+b\cdot ln(N)+c\cdot(N-1)\right], \tag{4.6}$$

$$\varepsilon_v^{acc}\big|_N = \varepsilon_v\big|_{N=1}\left[1+a\cdot ln(N)\right] \le \varepsilon_v^{\infty}\ , \tag{4.7}$$

where ε_v^{∞} is the cumulative volumetric strain the soil experiences when it changes from the initial void ratio e_A to the terminal void ratio e_∞

$$\varepsilon_v^{\infty} = \frac{e_A - e_\infty}{1+e_A}. \tag{4.8}$$

Equations (4.7) and (4.8) combine to predict the number of cycles needed to reach terminal void ratio N^*

$$N^* = exp\left[\frac{1}{a}\left(\frac{e_A-e_\infty}{1+e_A}\frac{1}{\varepsilon_v\big|_{N=1}}-1\right)\right]. \tag{4.9}$$

Note that the number of cycles to reach terminal void ratio N^* increases as the volumetric strain in the first cycle $\varepsilon_v|_{N=1}$ decreases (as shown in Narsilio and Santamarina, 2008).

The accumulation functions predict trends that are asymptotically compatible with the sediment behavior reviewed earlier (sketched in Figure 4.1). The volumetric strain accumulation for a soil element with an average stress obliquity close to critical state is null since $\varepsilon_v|_{N=1}(\eta_{av} = M) = 0$. In contrast, a soil element with an average stress obliquity close to the isotropic state does not accumulate shear strain given that $\varepsilon_q|_{N=1}(\eta_{av} = 0) = 0$. For any other stress obliquity, the shear strain continues accumulating linearly with N at a very high number of cycles $\varepsilon_q^{acc}|_N = \varepsilon_q|_{N=1} \cdot c \cdot (N - 1)$, while volumetric strain accumulation gradually ceases.

Constitutive parameters: The accumulation equations multiply the plastic strains in the first cycle, $\varepsilon_v|_{N=1}$ and $\varepsilon_q|_{N=1}$, so strain accumulation is inherently affected by the initial void ratio e_A, the initial static mean p_A and deviatoric q_A stresses, and the cyclic mean $\Delta p'$ and deviatoric Δq stress amplitudes. Experimental data show that constitutive parameters a, b, and c are mainly affected by the average stress obliquity $\eta_{av} = q_{av}/p'_{av}$ while other parameters have a secondary effect (see data in Wichtmann, 2005). The initial average deviatoric stress q_{av} and mean stress p'_{av} are calculated using the stress field at the end of the first load cycle (point D in Figure 4.2).

Module #4: Boundary Value Problem Solver

Cumulative strains predicted for each element must satisfy compatibility and equilibrium throughout the domain, regardless of whether the soil elements experience cyclic strain accumulation or not (refer to Module #2). Figure 4.3 shows the calculation sequence for the numerical algorithm used to compute strain accumulation with the number of load cycles in the boundary value problem.

Strain accumulation functions are not updated; thus, constitutive parameters (a, b, and c) and the strains in the first cycle $\varepsilon_v|_{N=1}$ and $\varepsilon_q|_{N=1}$ remain constant. The additional volumetric and shear strains that accumulate from cycle N to the cycle ($N + \Delta N$) are

$$\Delta\varepsilon_v^{acc} = \varepsilon_v^{acc}\Big|_{N+\Delta N} - \varepsilon_v^{acc}\Big|_N \tag{4.10}$$

and

$$\Delta\varepsilon_q^{acc} = \varepsilon_q^{acc}\Big|_{N+\Delta N} - \varepsilon_q^{acc}\Big|_N . \tag{4.11}$$

Both strains combine into the accumulated strain vector (similar expression in Suiker and de Borst 2003, and in Francois et al. 2009)

$$\Delta\boldsymbol{\varepsilon}^{acc} = \frac{1}{3}\Delta\varepsilon_v^{acc}\mathbf{1} + \frac{3}{2}\frac{\Delta\varepsilon_q^{acc}}{q_N}\left(\boldsymbol{\sigma}_N - p_N \cdot \mathbf{1}\right), \tag{4.12}$$

where p_N and q_N are the mean and deviatoric stress components of the stress state $\boldsymbol{\sigma}_N$ from the previous converged N-step and $\mathbf{1} = (1,1,1,0,0,0)^T$ is the identity vector. Note that while $\Delta\varepsilon_v^{acc}$ and $\Delta\varepsilon_q^{acc}$ depend on the static load and the first load cycle, the accumulation direction depends on the previously converged stress state $\boldsymbol{\sigma}_N$.

The stress increment due to the accumulated strain is

$$\Delta\boldsymbol{\sigma} = \mathbf{D}^e \cdot \left[\Delta\boldsymbol{\varepsilon} - \Delta\boldsymbol{\varepsilon}^{acc} - \Delta\boldsymbol{\varepsilon}^p\right], \tag{4.13}$$

where $\mathbf{D}^e$ [6x6] is the elastic stiffness matrix, $\Delta\boldsymbol{\varepsilon}$ [6x1] is the total strain increment, and $\Delta\boldsymbol{\varepsilon}^p$ [6x1] is the plastic strain increment. The total strain increment results from iterations for system equilibrium. The plastic strain increment is defined by the plastic flow rule that corresponds to the constitutive model used to compute the static load and first load cycle.

If the modified Cam Clay model is used to compute the static load and first load cycle, the elastic stiffness matrix $\mathbf{D}^e$ is evaluated with a stress-dependent bulk modulus $B = (1 + e_N)\cdot p_N/\kappa$ and a constant Poisson's ratio ν. The void ratio e_N, the mean pressure p_N, and the preconsolidation pressure p_{cN} are obtained from the previous converged step N. In addition, the plastic strain increment is

$$\Delta\boldsymbol{\varepsilon}^p = \Delta\xi \cdot \frac{\partial f(\boldsymbol{\sigma}_N, p_{cN})}{\partial\boldsymbol{\sigma}}, \tag{4.14}$$

where $f = f(\boldsymbol{\sigma}_N, p_{cN})$ is the associative yield function of the model and $\Delta\xi$ [-] is the consistency parameter

$$\Delta\zeta = \frac{\left(\frac{\partial f}{\partial \boldsymbol{\sigma}}\right)^{\mathrm{T}} \cdot \mathbf{D}^{e} \cdot \left(\Delta\boldsymbol{\varepsilon} - \Delta\boldsymbol{\varepsilon}^{acc}\right)}{\left(\frac{\partial f}{\partial \boldsymbol{\sigma}}\right)^{\mathrm{T}} \cdot \mathbf{D}^{e} \cdot \frac{\partial f}{\partial \boldsymbol{\sigma}} - \left(\frac{1+e_N}{\lambda-\kappa}\right) p_{cN} \frac{\partial f}{\partial p} \cdot \frac{\partial f}{\partial p_c}}. \tag{4.15}$$

The global stiffness matrix is constructed with the continuum tangent stiffness $\mathbf{D}^{ep}$ [6x6] (Borja and Lee 1990)

$$\mathbf{D}^{ep} = \mathbf{D}^{e} - \frac{\mathbf{D}^{e} \cdot \left(\frac{\partial f}{\partial \boldsymbol{\sigma}}\right) \cdot \left(\frac{\partial f}{\partial \boldsymbol{\sigma}}\right)^{\mathrm{T}} \cdot \mathbf{D}^{e}}{\left(\frac{\partial f}{\partial \boldsymbol{\sigma}}\right)^{\mathrm{T}} \cdot \mathbf{D}^{e} \cdot \frac{\partial f}{\partial \boldsymbol{\sigma}} - \left(\frac{1+e_N}{\lambda-\kappa}\right) p_{cN} \frac{\partial f}{\partial p} \cdot \frac{\partial f}{\partial p_c}}. \tag{4.16}$$

The updated void ratio $e_{N+\Delta N}$ is calculated using the accumulated volumetric strain increment (Eq. 4.10) and the updated preconsolidation pressure $pc_{N+\Delta N}$ using the updated mean stress $p_{N+\Delta N}$:

$$e_{N+\Delta N} = e_N - (1+e_N)\Delta\varepsilon_v^{acc} \tag{4.17}$$

$$pc_{N+\Delta N} = \exp\left(\frac{\mathrm{N} - \kappa \ln\left(p_{N+\Delta N}\right) - e_{N+\Delta N}}{\lambda-\kappa}\right). \tag{4.18}$$

The void ratio at the end of the first cycle $e_{N=1}$ (Module #2) is the value after reloading e_D, and the preconsolidation pressure p_{cN} is the cycle maximum load pc_B.

The accumulated strain (Eq. 4.12) induces internal stress $\Delta\boldsymbol{\sigma}$ (Eq. 4.13) and unbalanced forces in the system. Unbalanced force reduction causes node displacements until the system reaches the equilibrium state through Newtonian iterations.

Comments on Stability and Convergence

The stress field induced by the static load and the first load cycle (Modules #1 and #2) are "spatially regular," as they inherently satisfy equilibrium and compatibility. Anticipated strains after *N*-cycles will also be relatively regular as long as the cyclic load amplitude ΔP is small when compared to the static load P_A. It follows that the proposed solution will more readily converge for smaller $\Delta P/P_A$ and smaller increments in the

number of load cycles. In any case, strain accumulation is advanced slowly during early cycles (low N values) to prevent numerical instabilities. Additional load cycle increments ΔN are imposed until a given number of cycles N_f is reached (Figure 4.3).

1. Initial Static Condition: Self-Weight and Static Load (P_A)
   Calculated Strain: $\boldsymbol{\varepsilon}_A$
   Calculated Stress: $\boldsymbol{\sigma}_A$

2. First Load Cycle
   Calculated Strain: $\boldsymbol{\varepsilon}_B$, $\boldsymbol{\varepsilon}_C$, and $\boldsymbol{\varepsilon}_D$
   Calculated Stress: $\boldsymbol{\sigma}_B$, $\boldsymbol{\sigma}_C$, and $\boldsymbol{\sigma}_D$ (refer to Fig. 4.2)
   $\boldsymbol{\varepsilon}^{D\text{-}A} \rightarrow \varepsilon_v|_{N=1}$ and $\varepsilon_q|_{N=1}$ Eqs. (4.2) and (4.3)
   $\boldsymbol{\sigma}_D \rightarrow \eta_{av} = q_D/p'_D$

3. Accumulated Strain Increment
   $\varepsilon_v^{acc}|_N = \varepsilon_v|_{N=1}[1 + a(\eta_{av})\ln(N)]$
   $\varepsilon_q^{acc}|_N = \varepsilon_q|_{N=1}[1 + b(\eta_{av})\ln(N) + c(\eta_{av})]$
   First Increment:
      $\Delta\varepsilon_v^{acc} = \varepsilon_v^{acc}|_N - \varepsilon_v|_{N=1}$
      $\Delta\varepsilon_q^{acc} = \varepsilon_q^{acc}|_N - \varepsilon_q|_{N=1}$
      $\Delta\boldsymbol{\varepsilon}^{acc} = f(\Delta\varepsilon_v^{acc}, \Delta\varepsilon_q^{acc}, \boldsymbol{\sigma}_D)$ Eq.(4.12)
   Subsequent Increments:
      $\Delta\varepsilon_v^{acc} = \varepsilon_v^{acc}|_{N+\Delta N} - \varepsilon_v^{acc}|_N$
      $\Delta\varepsilon_q^{acc} = \varepsilon_q^{acc}|_{N+\Delta N} - \varepsilon_q^{acc}|_N$
      $\Delta\boldsymbol{\varepsilon}^{acc} = f(\Delta\varepsilon_v^{acc}, \Delta\varepsilon_q^{acc}, \boldsymbol{\sigma}_N)$ Eq.(4.12)

4. Compatibility and Equilibrium
   Calculated Strain: $\boldsymbol{\varepsilon}_N$
   Calculated Stress: $\boldsymbol{\sigma}_N$

5. Increase Number of Cycles ΔN
   Return to 3

Figure 4.3 Calculation sequence for the numerical algorithm. The final number of load cycles is N_f.

4.4 Numerical Examples

The hybrid algorithm described above is implemented using the UMAT subroutine in Abaqus/Standard with an explicit integration scheme so that the current step is calculated with values from the previous converged step. The modified Cam Clay constitutive model is used to analyze the static load (Module #1) as well as the first load cycle (Module #2), and to satisfy equilibrium and compatibility during repetitive loading (Module #4).

4.4.1 Calibration

For this exploratory study, the model is calibrated using published triaxial test results for a quartzitic subangular sand (Wichtmann 2005). The sand critical state friction angle is φ = 31.2° (i.e., M = 1.25), the minimum and maximum void ratios are $e_{\min}$ = 0.577 and $e_{\max}$ = 0.874, the mean grain diameter is d_{50} = 0.55 mm, and the coefficient of uniformity is C_u = 1.8. In the absence of experimental soil-specific data, the elastic threshold strain is estimated by assuming that interparticle displacement must exceed the atomic scale to break bonds $\|\boldsymbol{\varepsilon}_{el}\|$ = 1A/d_{50}; therefore, both volumetric and shear elastic threshold strains for this sand are assumed to be $\varepsilon_{v,el} = \varepsilon_{q,el} = 10^{-7}$. Furthermore, in the absence of empirical data, the minimum void ratio $e_{\min}$ is selected as the terminal void ratio e_∞ for the empirical accumulation functions in Module #3.

The effect of the average stress obliquity is considered using the following constitutive parameters in Eqs. (4.6) and (4.7):

$$a(\eta_{av}) = a_1(\mathrm{M} - \eta_{av})^2 + a_2 \qquad (a_1 = 1.09 \text{ and } a_2 = 0.87), \tag{4.19}$$

$$b(\eta_{av}) = -b_1(\eta_{av}) + b_2 \qquad (b_1 = 1.96 \text{ and } b_2 = 2.42), \text{ and} \tag{4.20}$$

$$c(\eta_{av}) = c_1(\eta_{av}) \qquad (c_1 = 6\cdot10^{-6}). \tag{4.21}$$

Figures 4.4a and 4.4b compare experimental data and calculated cumulative volumetric and shear strains. In linear-log scale, the measured volumetric strains show a pronounced

increase after N ~ 1000 cycles. This trend is unsustainable from a terminal-density point of view. Either a new deformation mechanism emerged (e.g., fatigue breakage) or experimental difficulties biased results. Therefore, it is decided to deviate from the volumetric strain data at large number of cycles when $N > 1000$.

Table 4.1 Soil Parameters in Numerical Examples

Parameter	**Symbol**	**Value**
Density	γ	18 kN/m^3
Coefficient of earth pressure at rest [(1)]	K_0	0.586
Modified Cam Clay		
Slope of unloading-reloading line in e-ln(p')	κ	0.002
Poisson's ratio	ν	0.3
Slope of critical state line in e-ln(p')	λ	0.004
Isotropic consolidation line at 1kPa	N	0.71
Slope of critical state line in p′-q	M	1.252
Empirical Accumulation Functions		
Accumulated volumetric strain	a_1	1.09
	a_2	0.87
Accumulated shear strain	b_1	1.96
	b_2	2.42
	c_1	$6 \cdot 10^{-6}$

Note: (1) The coefficient of earth pressure at rest is obtained from the compressibility parameters of the modified Cam Clay model (details in Muir Wood 1990)

The number of cycles to reach terminal density N^* computed using Eq. (4.9) and the selected constitutive parameters (Table 4.1) show that a soil element with initial void ratio e_A = 0.61 and average stress obliquity η_{av} = 0.5 reaches a terminal void ratio e_∞ = e_{min} = 0.577 after N^* ~ 1,200,000 load cycles if $\varepsilon_v|_{N=1}$ = 0.004, and N^* ~ 200 cycles if $\varepsilon_v|_{N=1}$ = 0.008.

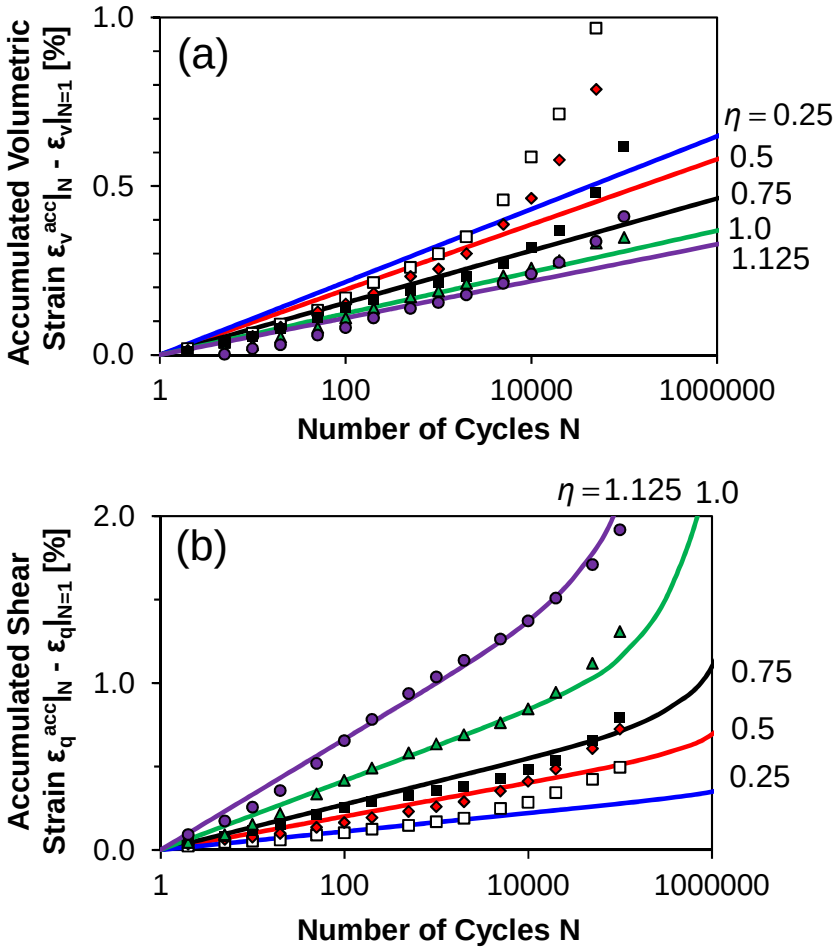

Figure 4.4 Calibration of the accumulation functions using drained cyclic triaxial test results for stress obliquities η = 0.25 (□), 0.5 (♦), 0.75 (■), 1.0 (▲), and 1.125 (●). (a) Accumulated volumetric strain, and (b) accumulated shear strain. The average initial void ratio is e_0 = 0.69, the stress amplitude is Δq = 60 kPa, and the average mean stress is p'_0 = 200 kPa. Note: data from Wichtmann (2005).

4.4.2 Physical Validation: Element Tests

Cyclic Triaxial Test

The cumulative axial strain and radial strain evolution with the number of load cycles N experienced by a soil element subjected to triaxial conditions are recovered from the volumetric and shear strain accumulation functions:

$$\varepsilon_{radial}^{acc}\Big|_N = \frac{1}{3}\left(\varepsilon_v^{acc}\Big|_N - \varepsilon_v\Big|_{N=1}\right) - \frac{1}{2}\left(\varepsilon_q^{acc}\Big|_N - \varepsilon_q\Big|_{N=1}\right) \tag{4.22}$$

and

$$\varepsilon_{axial}^{acc}\Big|_N = \frac{1}{3}\left(\varepsilon_v^{acc}\Big|_N - \varepsilon_v\Big|_{N=1}\right) + \left(\varepsilon_q^{acc}\Big|_N - \varepsilon_q\Big|_{N=1}\right). \tag{4.23}$$

Figure 4.5a shows the calculated trends for model parameters summarized in Table 4.1. An increase in the accumulated axial strain indicates vertical compaction, whereas a decrease in accumulated radial strain implies radial expansion. Both strains increase with stress obliquities, in agreement with Eqs. (4.19) to (4.21). (Note: The apparent acceleration with N is due to the logarithmic scale).

Cyclic Zero-Lateral Strain Tests

Experimental evidence shows that a soil element subjected to cyclic vertical load under zero-lateral strain conditions experiences volumetric strains and lateral stress changes (Sawicki and Swidzinski 1995). Figure 4.5b shows a soil element consolidated to σ_v = 100 kPa and cyclically loaded with a stress amplitude $\Delta\sigma_v$ = 20 kPa. The coefficient of earth pressure at rest $K_0 = \sigma_h/\sigma_v$ for virgin loading and the first unloading depends on the modified Cam Clay model parameters in Table 4.1 and results in K_0 = 0.62. Assuming accumulation parameters summarized in Table 4.1, the value of K_0 decreases to a minimum value K_0 = 0.58 during the initial cycles and increases gradually towards the isotropic state for a large number of cycles. The void ratio decreases from the initial value e_0 = 0.692 to reach e = 0.684 after N = 250,000 cycles. For reference, the

number of cycles to reach a terminal void ratio equal to $e_\infty = e_{min} = 0.577$ is $N^* \sim 10^{80}$ (from Eq. 4.9); however, it is unlikely that e_{min} is the terminal void ratio for zero-lateral-strain loading.

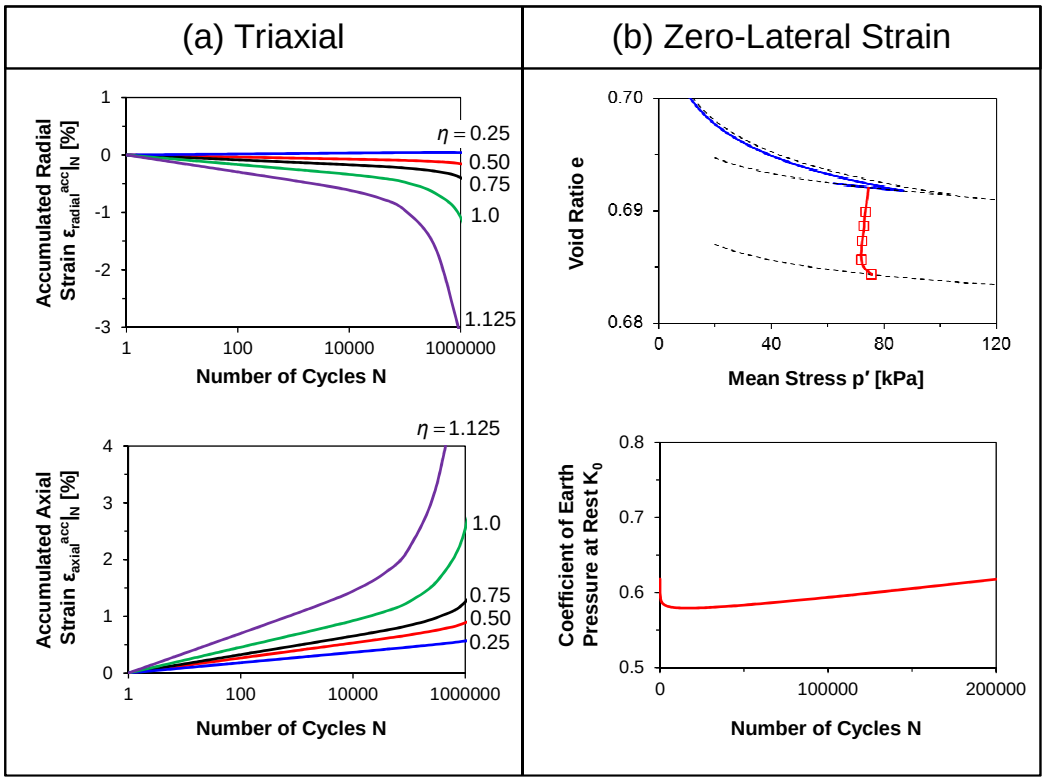

Figure 4.5 Strain accumulation in element tests. (a) Traixial test: evolution of radial $\varepsilon_{radial}^{acc}$ and axial $\varepsilon_{axial}^{acc}$ strain with the number of cycles N of samples subjected to cyclic vertical load; the average mean stress is $p'_0 = 200$ kPa, and the stress amplitude is $\Delta q = 60$ kPa. (b) Zero-lateral strain test: evolution of mean stress p', void ratio e, and coefficient of earth pressure at rest K_0 in an oedometer cell with average vertical stress $\sigma_v = 100$ kPa and subjected to a cyclic vertical stress $\Delta\sigma_v = 20$ kPa.

4.4.3 Example 1: Flexible Foundation Subjected to Repetitive Loading

Consider a flexible shallow foundation on sand subjected to a static vertical load followed by repetitive vertical loading (Figure 4.6). The subsurface is modeled using 2870 4-node plane strain elements with full integration. The numerically-predicted

footing bearing capacity is Q_{ult} = 750 kPa and agrees well with Terzaghi's bearing capacity.

The stress and strain fields due to the static load $Q_A = Q_{ult}/3$ = 250 kPa and the first load cycle $\Delta Q = 0.05 \cdot Q_A$ = 12.5 kPa are calculated using the modified Cam Clay model parameters in Table 4.1. The evolution of the footing vertical displacement with the number of cycles is shown in Figure 4.6a. The repetitive load causes an additional vertical displacement of 6 mm after N = 100,000 cycles, and there is an associated decrease in void ratio underneath the footing (Figure 4.6b).

The average void ratio from the surface to an influence depth similar to the footing width $z = B_f$ = 1 m is e_A = 0.689. Assuming that repetitive loading compacts the soil to its terminal void ratio e_∞ = 0.577, the maximum volumetric change the soil can experience in this zone is $\Delta\varepsilon_v^{max} = (e_A - e_\infty)/(1 + e_A)$ = 0.066. This volumetric change is equivalent to a maximum settlement $\delta_{max} = B_f \cdot \Delta\varepsilon_v^{max}$ = 66 mm, which is 11 times larger than the additional vertical displacement calculated after N = 100,000 cycles. This comparison between an upper bound estimate and numerical results suggest that footing settlement may still accumulate after the maximum number of cycles analyzed.

The zone of high stress obliquity $\eta = q/p$ grows from the footing center towards the edge underneath the footing (Figure 4.6c). This result suggests that while the static vertical load remains constant, the cyclic load gradually brings the subsurface soil closer to the critical stress obliquity η = M. However, sediment densification increases the preconsolidation pressure p_c and consequently enlarges the yield surface; therefore, cyclic loading does not necessarily bring the system closer to failure in this case.

The factor of safety FS = Q_{ult}/Q_A and the cyclic load amplitude ΔQ affect the footing response to the repetitive load (Figure 4.7). The settlement of the footing center point increases with the applied static load Q_A and with the cyclic load amplitude ΔQ (i.e., lower factor of safety).

The application of an additional static horizontal load on the footing $T_A \sim Q_A/6$ does not increase surface settlements. However, horizontal displacements increase proportional to the cyclic load amplitude ΔQ during repetitive loading (Figure 4.7b).

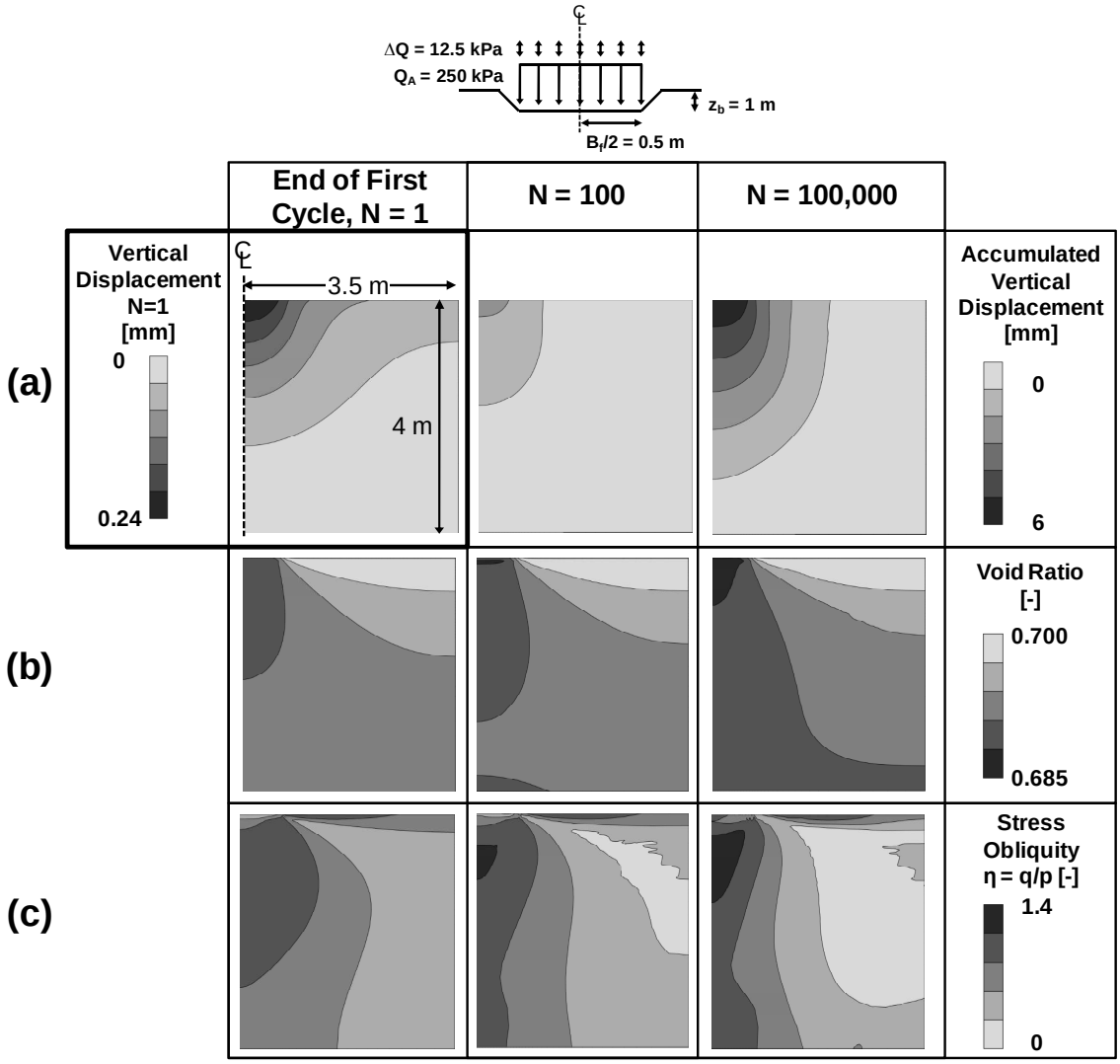

Figure 4.6 Flexible shallow foundation subjected to vertical repetitive loading. (a) Accumulation of vertical displacement. Distribution of (b) void ratio and (c) stress obliquity η for load cycles N = 1, 100, 100000. The static and the cyclic loads are $Q_A = Q_{ult}/3$ = 250 kPa and $\Delta Q = 0.1 \cdot Q_A$ = 12.5 kPa for a bearing capacity $Q_{ult} \sim$ 750 kPa.

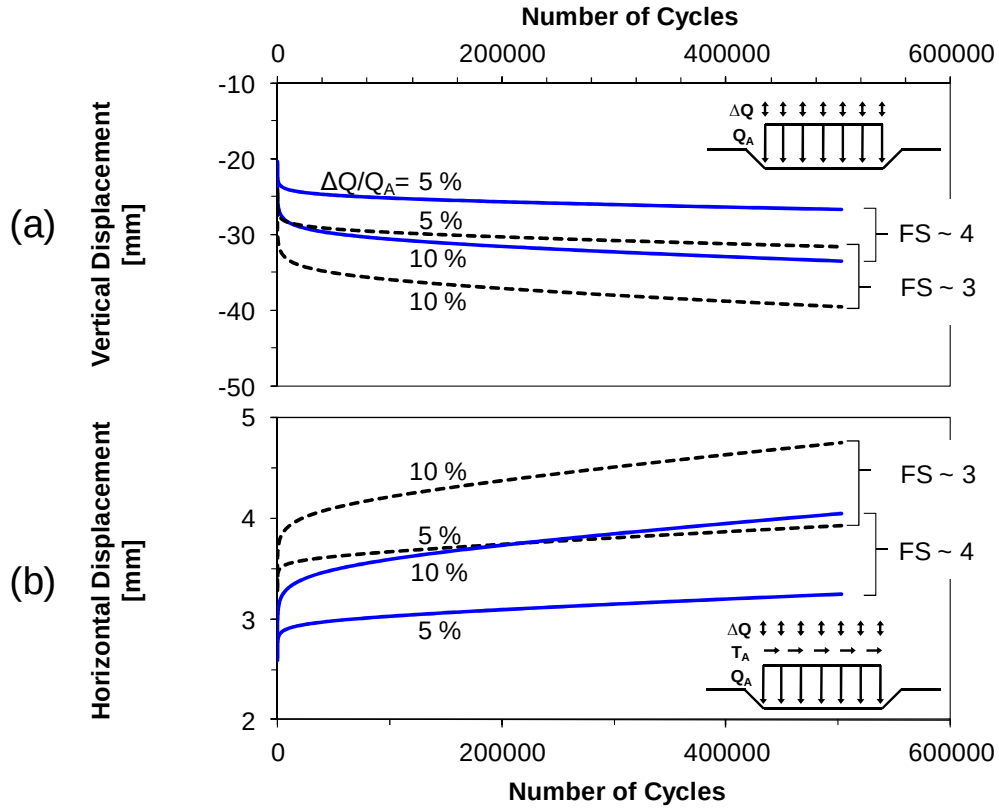

Figure 4.7 Displacement evolution of a flexible shallow foundation subjected to repetitive loading. (a) Vertical displacement measured at the center of the footing for static vertical loads Q_A = 250 kPa ($FS = Q_A^{ult}/Q_A \sim 3$) and Q_A = 190 kPa ($FS \sim 4$), and cyclic vertical loads ΔQ. (b) Horizontal displacement caused by an additional static horizontal load T_A = 40 kPa ($FS \sim 3$) and T_A = 30 kPa ($FS \sim 4$). Note: the static horizontal load T_A does not change the vertical displacement.

4.4.4 Example 2: Rigid Footing Subjected to Repetitive Eccentric Load

Gravity-based foundations are preferred for wind turbines onshore and offshore in shallow water (Byrne and Houlsby 2006). The repetitive wind load is transferred as an overturning moment to the foundation. Consider a B_f = 14 m wide footing buried D_f = 2.5 m deep, and made of concrete density γ_f = 25 kN/m^3 and Young's modulus E_f = 30 GPa. A static vertical force P_A = 10 MN/m is applied at the center of the footing. The

cyclic overturning moment is modeled as an eccentric cyclic force ΔP = 0.5 MN/m applied 3.5 m away from the centerline.

The sand subsurface is modeled with 4400 4-node plane strain elements with full integration. The stress and strain fields induced by the static load and the first load cycle are calculated using the modified Cam Clay model (sand model parameters in Table 4.1). For these parameters, the maximum numerically-predicted normal force the footing can sustain is approximately P_A^{ult} = 60 MN/m.

Figure 4.8 shows (a) vertical displacements induced by the static force and the first loading cyclic force, and the additional displacement due to the cyclic force after N = 100,000 cycles, (b) the void ratio, and (c) the stress obliquity for load cycles N = 1 and N = 100,000. It can be seen that the cyclic force induces densification, resulting in footing settlement and rotation.

The horizontal and vertical displacement of the footing center point B as well as the footing rotation, the difference between the vertical displacements of points A and C divided by the footing width B_f, are shown in Figure 4.9 for various static factors of safety $FS = P_{ult}/P_A$ and cyclic force amplitude $\Delta P/P_A$. Results indicate that displacements and rotations increase as the factor of safety P_{ult}/P_A decreases and the cyclic force amplitude $\Delta P/P_A$ increases. The continuous accumulation of both horizontal displacement and rotation suggests that the footing may experience long-term ratcheting behavior.

The volumetric accumulation is slow and the lowest void ratio reached after N = 100,000 cycles is $e = 0.68 > e_\infty = 0.577$ (Figure 4.8). Hence, the footing may continue settling and rotating with increasing load cycles until the soil approaches its terminal void ratio everywhere beneath the footing depth of influence where the strain from the first load cycle exceeds the elastic threshold strain.

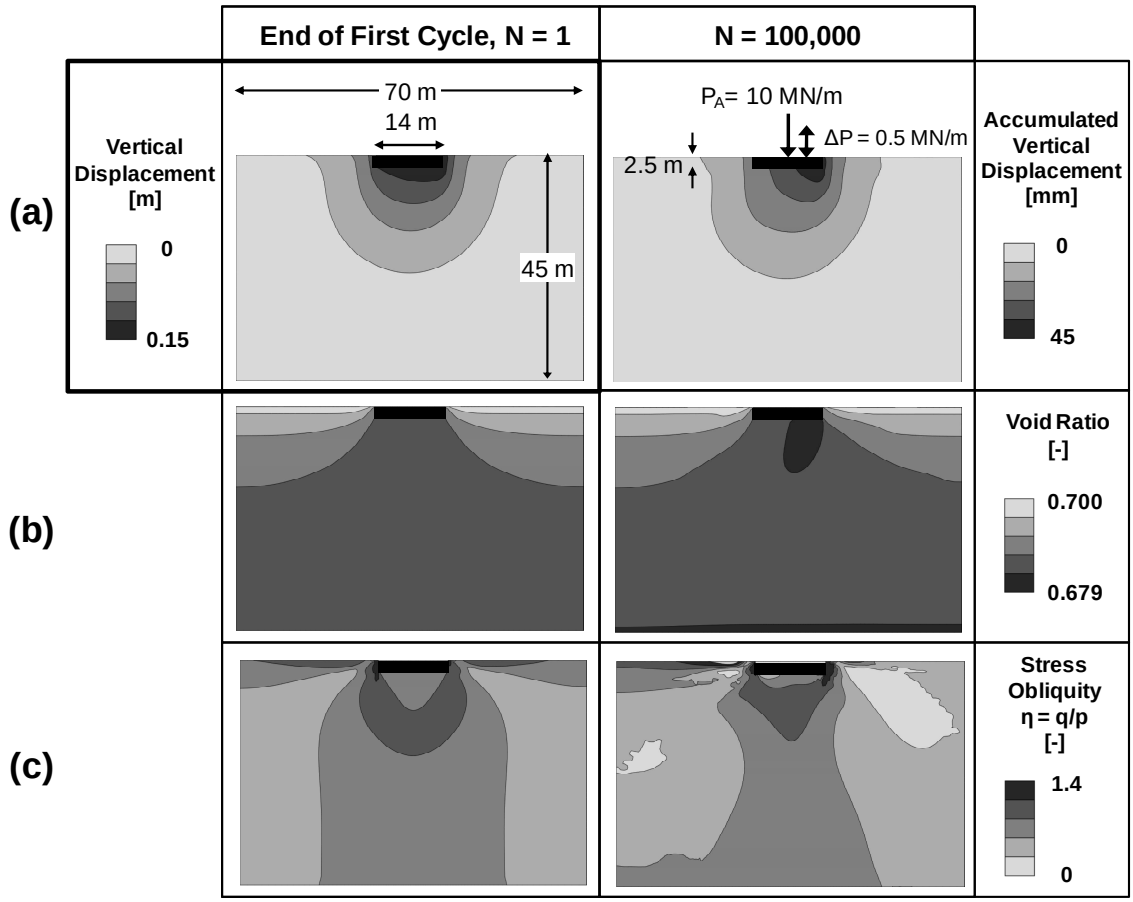

Figure 4.8 Rigid foundation subjected to repetitive eccentric load. (a) Vertical displacement. Distribution of (b) void ratio and (c) stress obliquity η for load cycles N = 1 and N = 100,000. The cyclic force ΔP is applied at e_x = 3.5 m from the footing center. Note: The maximum force the footing can sustain is estimated as P_A^{ult} = 60 MN/m.

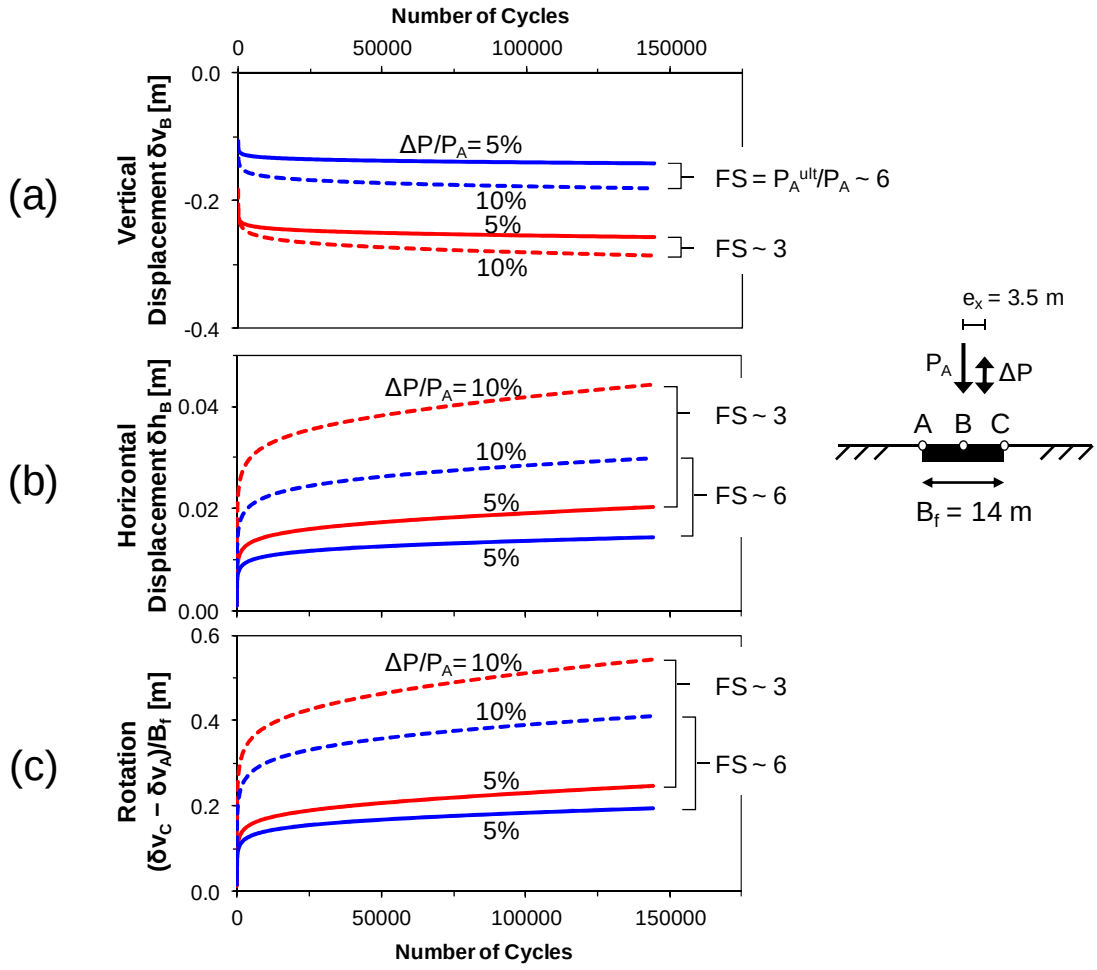

Figure 4.9 Rigid foundation subjected to repetitive eccentric load at e_x = 3.5 m. (a) Vertical displacement, (b) horizontal displacement, and (c) rotation ($\delta v_C - \delta v_A)/B_f$ for static loads P_A = 20 kN/m ($FS = P_A^{ult}/P_A \sim 3$) and P_A = 10 kN/m ($FS \sim 6$), and cyclic loads ΔP. Note: The maximum force the footing can sustain is estimated as P_A^{ult} = 60 MN/m.

4.5 Discussion

The review of the sediment response to a large number of cycles hinted at inherent complexity in numerical simulations. Choices made in the numerical approach introduced in this chapter attempt to reduce the problem complexity in view of robust predictions.

The empirical constitutive model should be carefully calibrated with available data, emphasizing the incremental and cumulative strain ratios trends. Additional element tests, such as triaxial and zero-lateral strain tests, can be performed to validate the proposed empirical constitutive model. Insightful guidance can be gained by predicting the evolution of vertical and horizontal strains in a triaxial condition and the evolution of the coefficient of earth pressure at rest K_0 under zero-lateral strain boundary conditions.

4.5.1 Limitations of the Numerical Scheme

The numerical scheme is not energy-based. The use of the number of cycles N as a state variable cannot capture previous cyclic loading effects or preconsolidation.

Available published data is limited to triaxial conditions, so analyses of plane strain problems should be carefully interpreted until adequate data become available. Proper model calibration will also require experimental data to determine elastic threshold strains and terminal densities.

The algorithm is designed to explore relatively constant repetitive loads, and it can only accommodate moderate changes in stress paths. Furthermore, the algorithm uses constant stress and strain amplitude to evaluate the empirical accumulation functions even though the state of stress and the strain amplitudes change during the application of repetitive loads. A control cycle can be included in the formulation to check the validity of this assumption (this verification is done in Niemunis et al., 2005)

The use of the modified Cam Clay model to predict the static load and first load cycle typically yields large deformations. The chosen stiffness parameters (κ and λ) are small in the examples presented above in order to limit the initial deformation to realistic field conditions; yet, higher stiffness causes pronounced stress concentrations during the application of the cyclic load. Hence, the stress induced by the accumulated strain must be carefully interpreted.

4.5.2 Advantages of the Numerical Scheme

The proposed numerical scheme and other recently-developed models with empirical strain accumulation are summarized and compared in Table 4.2. The simple and robust numerical scheme proposed in this study presents some clear advantages with respect to other methods. The constitutive model and accumulation functions capture proper initial and asymptotic trends, such as the non-linear response to the initial load and the first load cycle, terminal density, and ratcheting behavior for high stress obliquity. The same constitutive model is used for the static load, the first load cycle, and to satisfy equilibrium and compatibility during repetitive loading. The accumulated strain is explicitly defined, and the solution converges fast particularly when the cyclic component of the boundary load is low compared to the static component. The formulation can be modified to account for repetitive displacement boundary conditions.

Finally, the hybrid constitutive model with empirical strain accumulation described here adds five basic parameters (a, b, c, e_∞, and $\boldsymbol{\varepsilon}_{el}$) to the parameters needed for the constitutive model used to analyze the static and first-cycle loads. Additional calibration flexibility can be gained by relaxing these parameters; for example, accommodating a, b, and c as a function of the stress obliquity η or defining the terminal void ratio as a function rather than as a constant value. New test protocols will be needed to (1) properly calibrate the accumulation functions with emphasis on the determination of asymptotic conditions, and (2) accurately predict the first cycle strains $\varepsilon_v|_{N=1}$ and $\varepsilon_q|_{N=1}$.

4.5.3 Other Cyclic Loads

Other repetitive actions can cause cumulative soil deformation. For example, temperature oscillations trigger consolidation, excess pore fluid pressure, strength softening, and creep (Campanella and Mitchell 1968; Towhata et al. 1993), whereas freeze-thaw cycles (Qi et al. 2006), wet-dry cycles (Albrecht and Benson 2001; Tripathy and Subba Rao 2009), and cyclic pore fluid changes (Musso et al. 2003) induce soil

restructuration, volume change, and plastic strains. Thermo-mechanical coupling is addressed in Chapter 5, 6, and 7.

Table 4.2 Comparison of Accumulation Models

	Suiker and de Borst (2003)	**Niemunis et al. (2005)**	**Francois et al. (2009)**	**This study**
Definition of accumulated strain	Frictional sliding and volumetric compaction	Intensity times direction	Frictional sliding and volumetric compaction	Volumetric and shear strain
Consideration of the cyclic load amplitude	Pseudo-static application of the maximum expected boundary load	Strain amplitude from first cycle	Wave propagation model	Strain amplitude from first cycle
Account for threshold strains	No	No	No	Yes
Model for the initial state	Elasto-plastic model analogous to cyclic model	Hypoplastic with intergranular strain	N/A (1 step calculation)	MCC (it can accommodate any model)
Failure criterion	Drucker-Prager	Matsuoka-Nakai	N/A	MCC
Predefined cyclic flow rule	No	Modified Cam Clay direction	No	No
Accounts for terminal density	Yes	No	No	Yes
Stress dependent elastic stiffness	Yes	Yes	Yes	Yes
Accumulation Functions				
Stress dependent	Yes	Yes	Yes	Yes
Number of cycles	Yes	Yes	Yes	Yes
Depend on the previous-step accumulated strain	Yes	No (depend on first cycle)	Yes	No (depend on first cycle)
Initial void ratio effect	No	Yes	No	Not explicitly

Note: N/A = Not applicable

4.6. Conclusions

A numerical scheme is proposed to analyze the long-term behavior of boundary value problems with a large number of mechanical load cycles. The hybrid approach involves a mechanical constitutive model to analyze the static load and the first load cycle, and empirical strain accumulation functions to track the deformation accumulation during repetitive loading. The empirical functions predict volumetric and shear strain accumulation as a function of the plastic strain during the first load cycle, the obliquity and amplitude of the cyclic load, and the number of load cycles.

The numerical scheme satisfies initial conditions and asymptotic trends of the strain evolution. In particular, the cyclic flow rule, obtained from dividing the volumetric strain by the shear strain, (1) satisfies the modified Cam Clay model's flow rule for the first cycle and (2) approaches zero for a high number of cycles to account for terminal density while allowing for continuous shear strain accumulation, or ratcheting.

Accumulation functions add five new variables that require new test protocols for calibration. The physical admissibility of constitutive parameters can be pre-tested by modeling triaxial and zero-lateral strain tests.

Numerical simulations of a shallow foundation subjected to vertical and horizontal static loads and repetitive vertical load show the accumulation of vertical and horizontal displacements, and stress redistribution with the number of load cycles. On the other hand, the analysis of a rigid foundation subjected to repetitive eccentric load indicates that the footing experiences cumulative settlement and rotation; both trends are more pronounced as the factor of safety decreases and the cyclic load amplitude increases.

CHAPTER 5

THERMALLY-INDUCED WEDGING AND RATCHETING DISPLACEMENT

5.1 Introduction

The stability of a rock mass may be compromised by short-term events, such as earthquakes and pore-water pressure build-up due to rainfall. However, these conventional failure mechanisms cannot adequately explain rock slope deterioration at sites such as the Masada Mountain next to the Dead Sea rift (Hatzor et al. 2004; Sagy et al. 2003). Monitoring data gathered for finite key-blocks separated from the host rock mass by 20-to-50 cm wide cracks filled with chockstones reveal that annual permanent cliff displacements in the order of 0.5 mm do not correlate with the seismic activity of the region, and that the displacements occur even though the block geometry does not support toppling failure (Hatzor 2003).

On the other hand, the long-term systematic incidence of repetitive events can gradually lead to fracture weathering and slope erosion, and it can eventually cause failure of the entire rock mass. Cyclic changes in relative humidity aggravate subcritical crack propagation and particle breakage, as demonstrated by post-construction deformations observed in rockfill materials (Marsal 1967; Oldecop and Alonso 2007). Similarly, thermal cycles may result in gradual downward displacements of rock slopes (Gunzburger et al. 2005; Watson et al. 2004); in fact, the correlation between lateral displacements and temperature changes (Hatzor 2003; Vlcko et al. 2009) may resemble the expansion of grain silos subjected to temperature fluctuations (Blight 1987; Lapko and Prusiel 1997; Manbeck 1984). In addition, freeze-thaw cycles intensify thermal

effects on the mechanical response of rock discontinuities (Davies et al. 2001; Gruber and Haeberli 2007; Matsuoka 2001; Tharp 1987).

This chapter proposes a thermally-induced wedging mechanism that can explain the observed incremental displacement of rock blocks subjected to repeated temperature changes, such as those observed at the Masada Mountain.

5.2 Analytical Model

Consider the block sitting on the inclined plane shown in Figure 5.1a. Elongated chockstones fill the back joint and act as a wedge against the block. The frictionally-constrained thermal expansion of the block-wedge system upon heating can cause plastic displacement of the block base joint, followed by contraction and downward wedge movement upon cooling. Then, successive heating-cooling cycles would lead to displacement accumulation or ratcheting.

5.2.1 Equilibrium and Compatibility

This system is modeled in one dimension as a block resting on the inclined base at an angle η [°]. The elastic perfectly-plastic base joint has a shear stiffness k_j [Pa/m] and a friction coefficient μ [-]. The interface between the wedge and the block is perpendicular to the inclined base (Figure 5.1b). A fraction $\theta < 1$ of the wedge weight is transferred to the block through the shear stress along the block-wedge interface. The maximum force per unit length parallel to the base $F_{\max}$ [N/m] that the block frictional resistance can sustain is

$$F_{\max} = H \cdot \gamma_r \cdot (L_B + \theta \cdot L_W)(\mu \cdot \cos\eta - \sin\eta), \tag{5.1}$$

where H [m] is the block height (Figure 5.1b), γ_r [N/m^3] is the rock unit weight, L_B [m] is the block length, and L_W [m] is the wedge length.

A change in ambient temperature causes a thermal front that diffuses from the boundaries to the center of a rock element. One-dimensional heat diffusion from the

boundaries of the rock elements is considered. The shaded zones width S_d [m] in Figure 5.1b represent the areas affected by the diffusive thermal front.

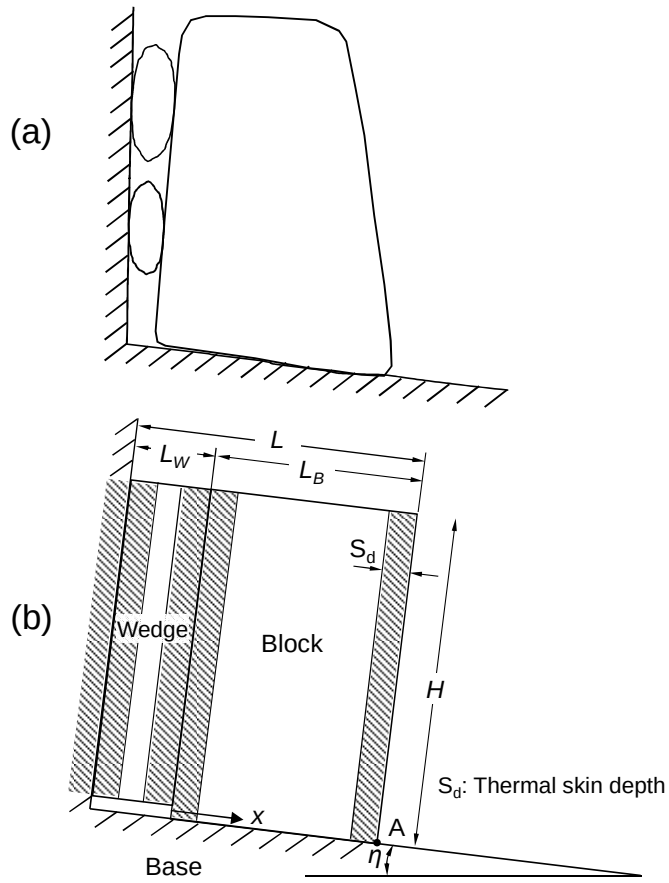

Figure 5.1 Model configuration. (a) Rock block resting on an inclined plane with chockstones filling the back joint. (b) Simplified block-wedge model for analysis. (Note: pictures of the actual block at the Masada Mountain can be found in Hatzor 2003).

The ensuing thermal expansion is constrained by friction at the block base. Compatibility of displacements requires that the joint elastic displacement δ_j^e [m] equals the displacement caused by the constrained thermal expansion of the block-wedge system

($\delta_T - \delta_\sigma$), i.e., the displacement caused by free thermal expansion δ_T [m] minus the elastic contraction δ_σ [m]:

$$\delta_T - \delta_\sigma = \delta_j^e . \tag{5.2}$$

It is assumed in the limit condition, before thermally-induced sliding occurs, that the block toe does not slide (point *A* in Figure 5.1b), and that the equivalent strain of the block is half the maximum strain. In this condition, the elastic contraction due to the force per unit length $F_{\max}$ [N/m] is

$$\delta_\sigma = \frac{F_{\max}}{H \cdot E}\left(L_W + \frac{L_B}{2}\right), \tag{5.3}$$

where E [Pa] is the rock Young's modulus. On the other hand, the limiting joint elastic displacement δ_j^* [m] satisfies

$$\frac{F_{max}}{L_B} = k_j \cdot \delta_j^* , \tag{5.4}$$

thus,

$$\delta_j^* = \frac{1}{k_j} \cdot \frac{F_{max}}{L_B} . \tag{5.5}$$

The joint shear stiffness k_j [Pa/m] is obtained from the shear displacement required to reach the maximum shear strength (Goodman 1989). Experimental results show that the joint shear stiffness is proportional to the normal stress and inversely proportional to the joint length. For instance, the joint shear stiffness of dolomites may exceed 10 GPa/m for 10 cm length samples and normal stresses larger than 1 MPa (Hatzor et al. 2004), but it may be lower than 0.1 GPa/m for interface lengths between 1 and 10 m and normal stresses lower than 0.1 MPa (Bandis et al. 1983). These values indicate that the limiting joint elastic displacement is in the order of 100 to 2000 times smaller than the joint length.

5.2.2 Thermal Expansion

Typical daily and seasonal air temperature fluctuations in various environments are compiled in Table 5.1. Daily temperature fluctuations can be as high as 35°C on Earth and may exceed hundreds of degrees on the lunar surface.

The rock temperature $T(x,t)$ at a distance x from the boundary and time t responds to changes in boundary temperature, as prescribed by the heat diffusion equation (Carslaw and Jaeger 1986)

$$\frac{\partial T(x,t)}{\partial t} = D_T \frac{\partial^2 T(x,t)}{\partial x^2} . \tag{5.5}$$

The rock thermal diffusivity $D_T = k_T/(\rho \cdot c_p)$ [m^2/s] is proportional to its thermal conductivity k_T [W/m/K] and inversely proportional to its mass density ρ [kg/m^3] and specific heat capacity c_p [J/kg/K]. Table 5.2 lists typical values of mass density, thermal conductivity, specific heat capacity, and thermal diffusivity for various rock types. These data show that thermal diffusion is faster in dolomite than in granite and basalt.

Table 5.1 Air Temperature Fluctuations in Typical Environments

Site	**ΔT** [°C]	**References**
Atlanta, USA	10° (daily - 12 hrs) 20° (seasonal – 180 days)	Earth System Research Laboratory (ERSL), NOAA's Physical Sciences Division (PSD)
Masada, Israel	20° (daily - 12 hrs) 20° (seasonal – 180 days)	Hatzor (2003)
Atacama Desert, Chile	35° (daily - 12 hrs) 5° (seasonal – 180 days)	McKay et al. (2009)
Moon	280° (354 hrs) [(a)]	Heiken et al. (1991)
Mars	60° (daily - 12 hrs) [(b)]	Tamppari et al. (2010)

Notes: (a) From Lunar sunrise to sunset
(b) Martian synodic day is similar to that of the Earth.

Table 5.2 Typical Rock Properties

Parameter	Symbol	Units	Granite	Basalt	Dolomite
Young's modulus	E	[GPa]	50 (a)	70 (a)	50 (b)
Mass density	ρ	[kg/m^3]	2650 (a)	2850 (c)	2550 (b)
Friction coefficient of discontinuities	μ	[-]	0.6 (d)	0.6 (e)	0.5 (f)
Thermal expansion coefficient	α	[10^{-6}/°C]	8 (g)	5 (h)	8 (g)
Thermal conductivity	k_T	[W/m/K]	3 (i)	2 (a)	4 (j)
Specific heat capacity	c_p	[J/kg/K]	900 (i)	900 (c)	900 (c)
Thermal diffusivity	D_T	[m^2/s]	$1.3 \cdot 10^{-6}$	$0.8 \cdot 10^{-6}$	$1.7 \cdot 10^{-6}$

Notes: Data from (a) Turcotte and Schubert (2002); (b) Hatzor and Palchik (1997); (c) Waples and Waples (2004); (d) Jaeger et al. (2007); (e) Barton and Choubey (1977); (f) Handin (1969); (g) Franklin and Dusseault (1989); (h) Ryan and Sammis (1981); (i) Heuze (1983); (j) Vosteen and Schellschmidt (2003)

The homogenization time t^* [s] is defined as the time required to change the temperature at the center $x = L/2$ of a one-dimensional rock element length L from an initial temperature T_0 [°C] to 99 % the new boundary temperature T_1 [°C] at $x = 0$ and $x = L$ (e.g., see x-direction for the block in Figure 5.1b). The homogenization time of the block and the wedge can be estimated as $t_B^* = 0.5 \cdot L_B^2 / D_T$ and $t_W^* = 0.5 \cdot L_W^2 / D_T$, respectively (Carslaw and Jaeger 1986). From this estimation, the thermal skin depth S_d [m] of a rock element length L for a certain exposure time t_{exp} [s] is defined as

$$S_d = \begin{cases} \sqrt{0.5 \cdot D_T \cdot t_{\exp}} & t_{\exp} < 0.5 \cdot L^2 / D_T \\ L/2 & t_{\exp} \geq 0.5 \cdot L^2 / D_T \end{cases} . \quad (5.6)$$

The skin depth maximum value is half the length of the rock element $S_d = L/2$ when the exposure time equals the homogenization time $t_{exp} = t^*$. For daily temperature fluctuations, the thermal skin depth for rocks listed in Table 2 ranges between $S_d = 0.1$ m

and 0.2 m (t_{exp} ~ 12hr), and it exceeds S_d = 2.5 m for seasonal temperature changes (t_{exp} > 180 days).

Homogenization t^* and exposure t_{exp} times define three different thermal expansion regimes. Consider a block larger than the wedge ($L_B > L_W$ - Figure 5.1b) and an air temperature change from T_0 to T_1 ($T_1 > T_0$). When the exposure time is short, $t_{exp} < 0.5L_W^2/D_T < 0.5L_B^2/D_T$, the wedge, the block, and the left wall behind the wedge have transient non-homogeneous temperature distributions. If the resultant thermal expansion upon heating is unconstrained, the expansion of the four skin depths involved could reach the free thermal displacement (Figure 5.1b)

$$\delta_T = \alpha \cdot \Delta T \cdot (4 \cdot \beta \cdot S_d), \tag{5.7}$$

which is proportional to $\Delta T = T_1 - T_0$ [°C] and the rock thermal expansion coefficient α [1/°C]. The dimensionless coefficient $\beta \leq 1.0$ accounts for the non-uniform diffusive temperature distribution within the skin depth of the rock element.

For exposure times t_{exp} longer than the time required to homogenize the wedge but shorter than that required to reach a homogeneous block temperature, $0.5L_W^2/D_T < t_{exp} < 0.5L_B^2/D_T$, the free thermal displacement of the system combines the full expansion of the wedge and the partial expansion of the block and the left wall

$$\delta_T = \alpha \cdot \Delta T \cdot (L_W + 2 \cdot \beta \cdot S_d) \ . \tag{5.8}$$

Finally, when the exposure time t_{exp} exceeds the time required for temperature homogenization in the block and the wedge, $0.5L_W^2/D_T < 0.5L_B^2/D_T < t_{exp}$, the free thermal displacement is

$$\delta_T = \alpha \cdot \Delta T \cdot (L_W + \xi \cdot L_B + \beta \cdot S_d) \ , \tag{5.9}$$

where the dimensionless coefficient $\xi \leq 1.0$ is introduced to account for the free thermal expansion of the right portion of the block that does not contribute to constraining the system thermal expansion.

5.2.3 Maximum Temperature Change for Elastic Deformation

The displacement compatibility condition at the verge of plastic deformation is $\delta_T - \delta_\sigma = \delta_j^*$ (Eq. 5.2). Replacing in this equation the thermal expansion displacement δ_T computed for an exposure time t_{exp} (Eqs. 5.7, 5.8, or 5.9), the elastic contraction δ_σ (Eq. 5.3), and the maximum joint elastic displacement δ_j^* (Eq. 5.4), the maximum temperature that the system can sustain without plastic displacement is

$$\Delta T_{max} = \frac{F_{max}}{\alpha \cdot d(t_{exp}) \cdot E}\left[\frac{E}{k_j \cdot L_B} + \frac{L_W}{H} + \frac{L_B}{2H}\right], \tag{5.10}$$

where the length subjected to expansion d(t_{exp}) is a function of the exposure time

$$d(t_{exp}) = \begin{cases} 4 \cdot \beta \cdot S_d & if \quad t_{exp} < 0.5L_W^2 / D_T < 0.5L_B^2 / D_T \\ L_W + 2 \cdot \beta \cdot S_d & if \quad 0.5L_W^2 / D_T < t_{exp} < 0.5L_B^2 / D_T \\ L_W + \xi \cdot L_B + \beta \cdot S_d & if \quad 0.5L_W^2 / D_T < 0.5L_B^2 / D_T < t_{exp} \end{cases} .$$

The ratio $E/(k_j \cdot L_B)$ is much larger than $(L_W + 0.5 \cdot L_B)/H$ for typical field conditions, so the term $(L_W + 0.5 \cdot L_B)/H$ can be neglected and the maximum temperature for elastic deformation ΔT_{max} becomes independent of the rock Young's modulus E. Furthermore, if all the wedge weight is assumed to act on the block (θ = 1 - Eq. 5.1), the maximum temperature at the verge of plastic deformation for a given exposure time t_{exp} is

$$\Delta T_{max} \approx \frac{1}{\alpha}\left(1 + \frac{L_W}{L_B}\right)(\mu \cdot cos\,\eta - sin\,\eta)\frac{H}{d(t_{exp})} \cdot \frac{\gamma_r}{k_j} . \tag{5.11}$$

The factor $(\mu \cdot \cos\eta - \sin\eta)$ decreases as the base inclination η increases. Hence, the maximum temperature ΔT_{max} decreases when either the base inclination η, the thermal expansion coefficient α, or the joint shear stiffness k_j increases. Conversely, ΔT_{max} increases with the system height H, the rock unit weight γ_r, and the friction coefficient μ.

Figure 5.2 shows the variation in ΔT_{max} as a function of the relative wedge-to-block length ratio L_W/L_B predicted by Eq. (5.11) for different common rocks. Results indicate that: (1) basaltic rock systems require higher temperature changes to exhibit plastic deformation in comparison to granite and dolomite; (2) seasonal temperature

changes are more likely to cause permanent displacements due to the extent of the thermal skin depth; and (3) the relative wedge-to-block length L_W/L_B has a non-linear effect on the ΔT_{max} value.

The condition at the Masada Mountain in Figure 5.2 considers a block height H = 13m, a block length L_B = 7.5m and properties for dolomite in Table 5.2. A comparison of this condition with the daily dolomite curve in Figure 5.2 indicates that an average daily temperature fluctuation of 20°C at Masada (Table 5.1) cannot cause plastic deformation. In contrast, a seasonal temperature fluctuation of 20°C can cause plastic deformation regardless of L_W/L_B (seasonal dolomite curve in Figure 5.2). These results suggest that the seasonal temperature changes are responsible for plastic block displacements observed in the Masada massif.

5.2.4 Plastic Displacement - Ratcheting

If the external temperature change ΔT exceeds the maximum temperature for elastic deformation ΔT_{max}, the plastic displacement δ_j^p [m] that the block will experience is

$$\delta_j^p = \delta_T - \delta_\sigma - \delta_j^* \ . \tag{5.12}$$

Figure 5.3 shows plastic displacements for a dolomite block-wedge system subjected to an external seasonal temperature change of ΔT = 20°C. Results are presented as a function of the wedge-to-block size ratio L_W/L_B for several plane inclination angles η. The calculated plastic displacement agrees with the value of 0.5 mm per year measured at the Masada Mountain (Hatzor 2003).

Gravitational bias hinders the block upward motion during cooling. Instead, cooling contraction allows chockstones to fall down into a lower position in the back joint and to exert a renewed wedging action against the block during the following heating cycle. This sequence of events leads to displacement accumulation, or ratcheting.

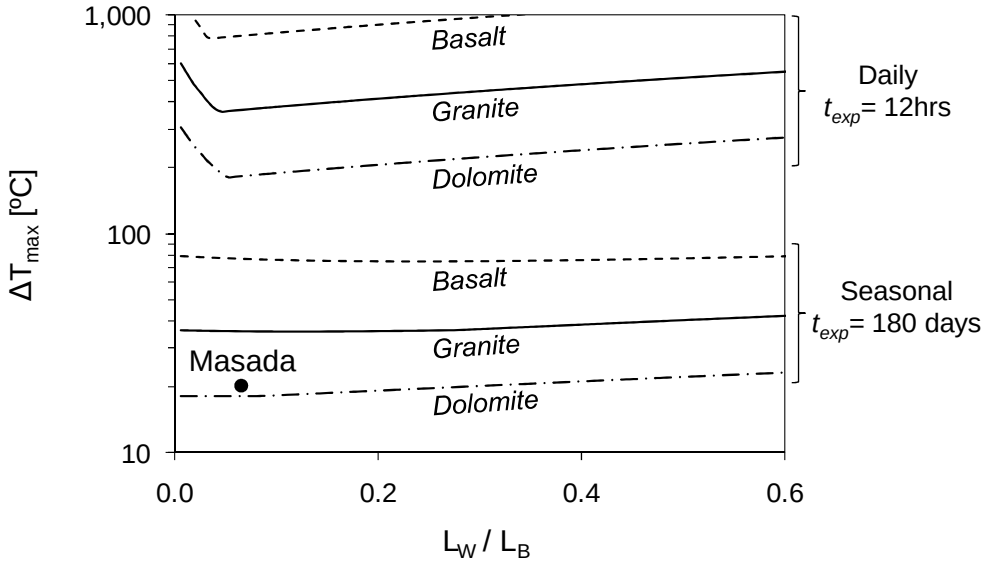

Figure 5.2 Maximum temperature change for elastic deformation ΔT_{max} as a function of the relative wedge-to-block size L_W/L_B. Model parameters: η = 19°, L = 8 m; H = 13 m, k_j = 0.045 GPa/m, β = 1.0, and ξ = 0.5. Material parameters in Table 5.2.

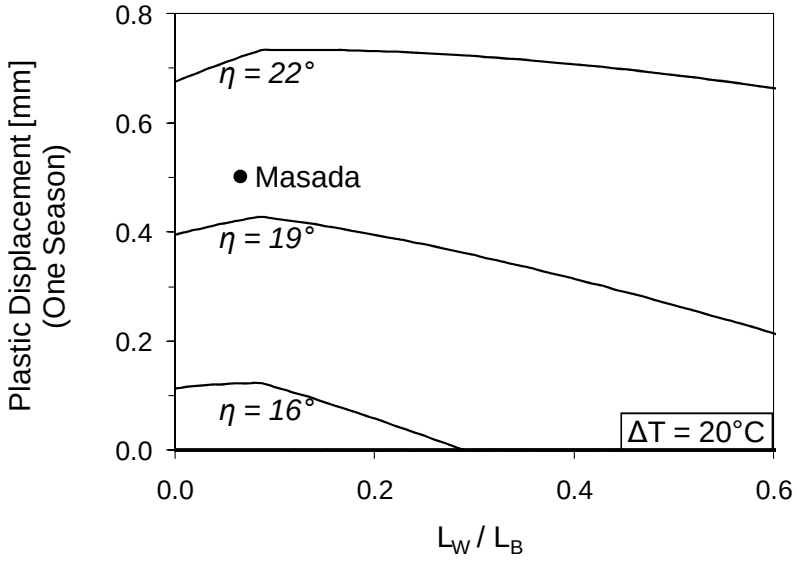

Figure 5.3 One-cycle plastic displacement for several plane inclination angles. Dolomite block-wedge system subjected to a seasonal temperature change ΔT = 20°C. Model and material parameters as in Figure 5.2. (Note: basaltic and granitic block-wedge systems do not experience seasonal plastic displacement for ΔT = 20°C – Figure 5.2).

5.3 Experimental Validation

The proposed analytical model was experimentally validated using an acrylic block-wedge system that reacts against an aluminum base and back wall (Figure 5.4). The thermal expansion of the block-wedge elements ($\alpha_{acrylic} = 90 \cdot 10^{-6}$/°C) exceeds at least four times the expansion of the base and wall ($\alpha_{aluminum} = 20 \cdot 10^{-6}$/°C). Dimensionless ratios regarding model size, material and interface stiffness, exposure time, and thermal diffusion time were selected to simulate conditions similar to Masada Mountain.

The block-wedge system and the frame are housed within an extruded polystyrene foam box. The air temperature inside the box is controlled with light bulbs powered through a thermostat switch, and homogenized with a fan. The air and the block temperatures are monitored with thermocouples, and the wedge vertical displacement is monitored with a linear variable differential transformer (LVDT) mounted outside the insulating box. Shields prevent direct radiation to the acrylic elements and sensors. Temperatures and displacement are recorded every 5 sec with a data logging system.

5.3.1 Experimental Results

The parametric study included various slope angles and thermal regimes. A typical experimental result for a horizontal base $\eta = 0°$ is shown in Figure 5.5. The time history comprises four stages: (i) stabilization (2 hrs), (ii) heating (~2hr), (iii) thermal cycles (~19 hrs), and (iv) cooling (~14 hrs). Initial heating $\Delta T = 25$°C and final cooling can be regarded as long-term or seasonal temperature changes, whereas the temperature variation $\Delta T = 1$°C during the cyclic stage can be considered as a short-term or daily temperature change.

Figure 5.5 shows a downward wedge movement during the cooling phase of thermal cycles. The plastic displacement accumulates at a rate of $\delta_v = 10$ μm per cycle, which corresponds to a permanent horizontal block displacement $\delta_h = 1.2$ μm per cycle (note: from geometric considerations, the horizontal block displacement δ_h is related to

the vertical wedge displacement δ_v as $\delta_h = \delta_v \cdot \tan 7°$). Initial heating and final cooling without thermal cycles results in a permanent vertical wedge displacement $\delta_v = 3$ μm and a permanent horizontal block displacement $\delta_h = 0.37$ μm.

The experimental model is thin ($t_B = 22$ mm thick) and heat propagates from both faces. Hence, the length subjected to thermal expansion, $d(t_{exp})$ in Eq. (5.11), can be estimated as $d(t_{exp}) = L_W + L_B = 286$ mm. Considering a horizontal base $\eta = 0°$, the maximum force per unit length that the block frictional resistance can sustain is $F_{max} = (W_B + W_W) \cdot \mu / t_B = 571.5$ N/m, where the block weight is $W_B = 25.7$ N, the wedge weight is $W_W = 4.2$ N, and the measured friction coefficient between acrylic and aluminum is $\mu = 0.42$. Assuming a shear stiffness $k_j = 0.1$ [GPa/m] and a Young's modulus $E = 3$ GPa, Equation (5.10) predicts a maximum temperature without plastic displacement $\Delta T_{\max} = 0.98°C$. Since both short- and long-term temperature changes exceed $\Delta T_{\max}$, thermal ratcheting is expected. However, the magnitude of the predicted permanent displacement depends on the temperature change in each case. The elastic contraction due to the force per unit length in Equation (5.3) is $\delta_\sigma = 0.1$ μm, and the limiting joint elastic displacement in Equation (5.4b) is $\delta_j^* = 25.0$ μm. Hence, a short-term temperature change $\Delta T = 1°C$ causes a free thermal displacement $\delta_T = \alpha \cdot \Delta T \cdot (L_W + L_B) = 26.5$ μm and a plastic horizontal block displacement $\delta_j^p = 0.6$ μm, according to Equation (5.12). Similarly, a long-term temperature change $\Delta T = 25°C$ causes a free thermal displacement $\delta_T = \alpha \cdot \Delta T \cdot (L_W + L_B) = 0.64$ mm, which yields a plastic horizontal block displacement $\delta_j^p = 0.62$ mm. Both values compare well with measured experimental values.

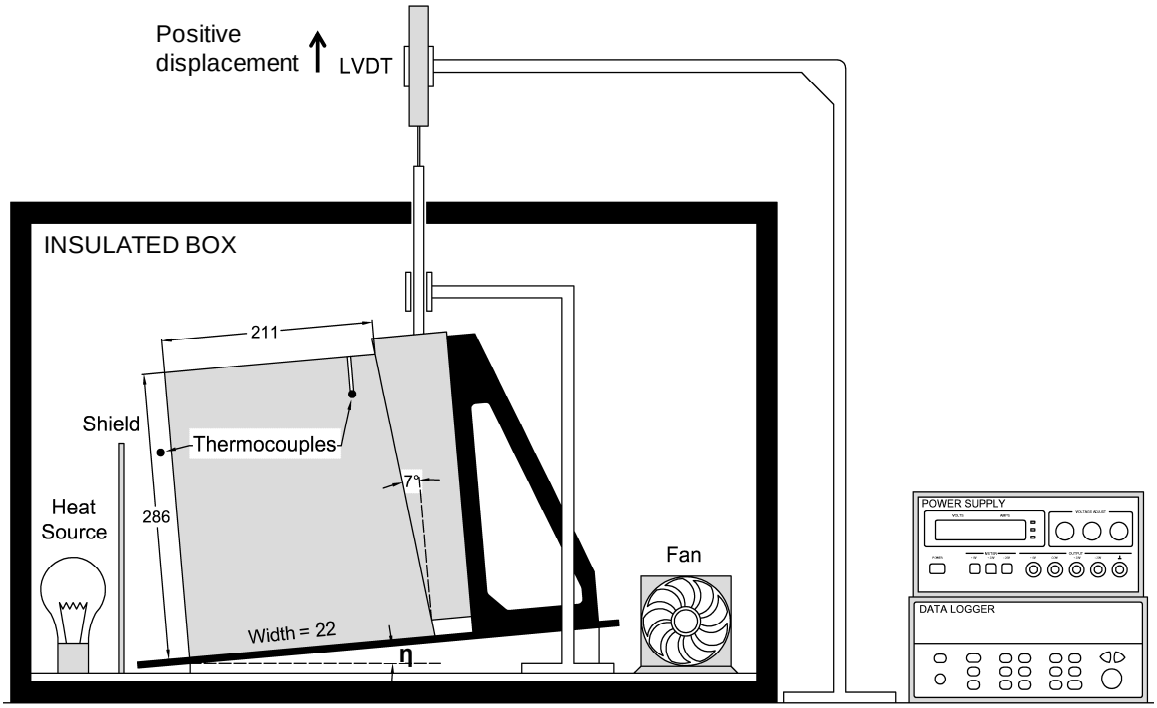

Figure 5.4 Thermally-induced wedging and ratcheting displacement: Experimental setup. Dimensions are in milimeters.

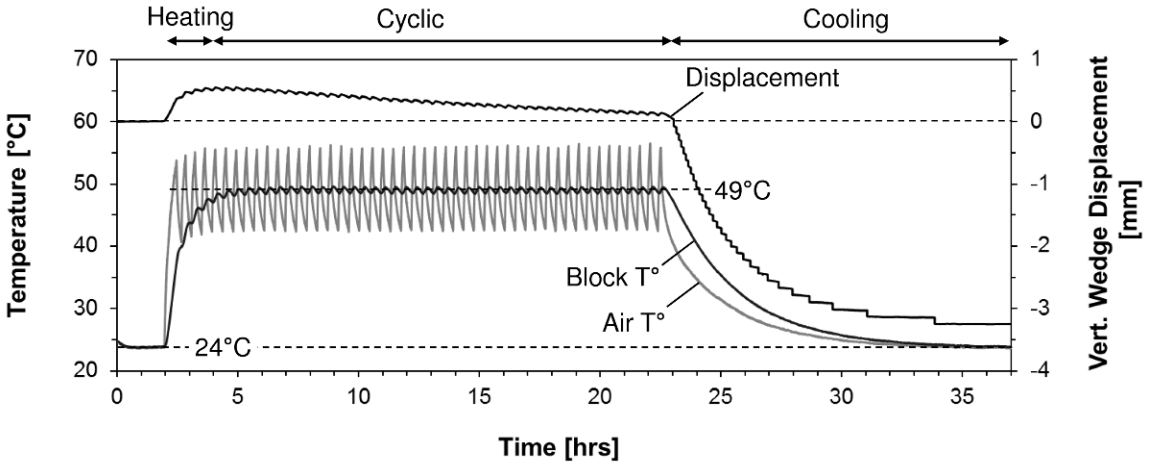

Figure 5.5 Experimental results for horizontal base η = 0°. Air and block temperatures, and vertical wedge displacement are measured by the thermocouples and the LVDT shown in Figure 5.4.

5.4 Conclusions

Thermally-induced plastic displacement along joints can combine with wedging effects to cause the gradual accumulation of block displacements. The proposed analytical solution shows the non-linear effect of relative wedge-to-block size and the relevance of exposure time and the base inclination.

Most rock slope systems are likely to experience this deformation mechanism in environments with seasonal temperature fluctuations higher than ΔT = 20 ºC. Dolomite rocks are more sensitive to this mechanism than granite because of their higher thermal diffusivity. Basaltic rocks are least prone to thermo-mechanical wedging and ratcheting displacement.

Experimental results validate the analytical model. Repeated heating and cooling cycles cause accumulation of permanent displacement, which is proportional to the temperature change amplitude. This mechanism can explain the ratcheting behavior observed at the Masada massif.

CHAPTER 6

THERMALLY-INDUCED GEOMEMBRANE RATCHETING DISPLACEMENT

6.1 Introduction

Geomembranes are impermeable barriers that can remain exposed either during construction or as part of a permanent geomembrane cover system (Richardson 2000; Rowe 2005). An exposed geomembrane heated by direct sun radiation can undergo temperature changes as high as 50°C (Chappel 2012; Take et al. 2012). The thermal expansion is constrained by friction against the underlying soil. Low flexural stiffness, high thermal expansion, and frictional restraint lead to both the formation of wrinkles, especially at imperfections such as creases, seams, and overlaps (Rowe 2011; Take et al. 2007), and gradual slippage when geomembranes are placed on slopes (Chappel et al. 2008; Rowe et al. 2012).

This study examines the behavior of geomembranes on inclined planes subjected to thermal cycles. First, experimental evidence of thermally-induced ratcheting displacement is presented. Then, governing equations are identified to formulate a numerical algorithm that solves this coupled thermo-mechanical problem.

6.2 Experimental Evidence of Geomembrane Ratcheting Displacement

Consider a geomembrane resting on an inclined plane. The membrane behavior when subjected to thermal cycles is experimentally examined first.

6.2.1 Devices and Methods

The experimental setup consists of a low density polyethylene membrane resting on an inclined aluminum base (Note: parameters summarized in Table 6.1). The slope-

membrane system is housed within a thermally-insulated box with controlled air temperature. The air temperature is recorded every five seconds using two thermocouples mounted near the membrane longitudinal edges and a data logger system. Metal shields prevent direct source radiation to the membrane and sensors, and a fan ensures air circulation and thermal homogenization (Figure 6.1).

Membrane displacements are monitored every five minutes with a digital camera mounted normal to the inclined base outside the insulating box. The membrane displacement is determined by image processing using marks painted on the membrane; the image resolution is 0.03 mm/pixel and allows for a displacement resolution better than δ = 0.03 mm.

Table 6.1 Geomembrane Parameters

Parameter	Symbol	Units	Value
Length	L	[m]	0.16
Width	B	[m]	0.08
Thickness	t_h	[mm]	0.5
Unit weight	γ_m	[kN/m^3]	9.5
Young's modulus	E	[GPa]	0.3
Thermal expansion coefficient	α	[10^{-5}/°C]	32 (a)
Interface friction coefficient	μ	[-]	0.58
Critical interface displacement	δ^*	[mm]	0.01

Note: (a) This value was measured with image processing by hanging the membrane and changing the air temperature in the insulated box.

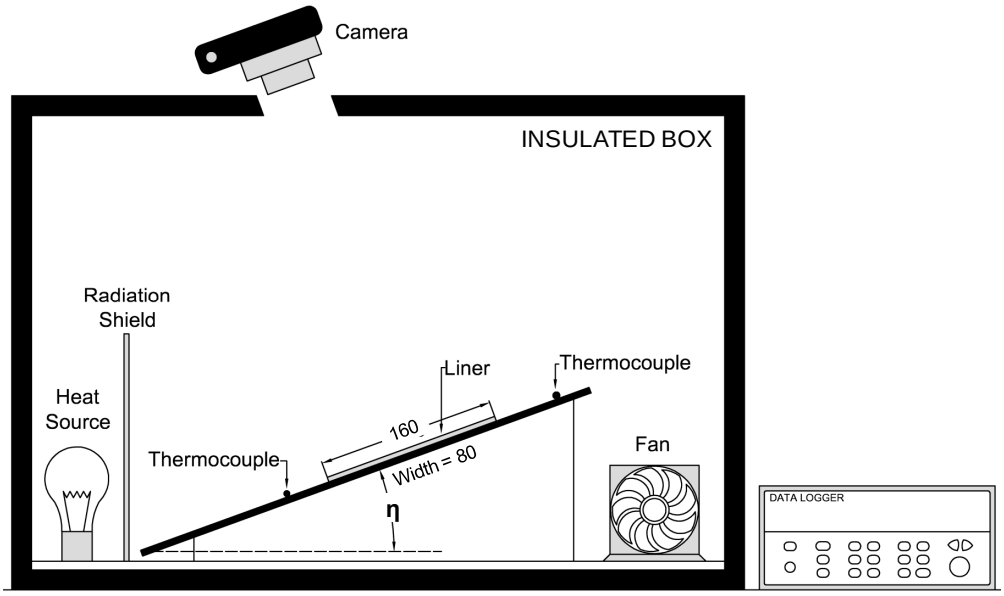

Figure 6.1 Thermally-induced geomembrane ratcheting displacement: Experimental setup. Dimensions are in millimeters.

6.2.2 Experimental Results

Air temperature and the displacement of points near the lower and upper edges of the membrane are shown in Figure 6.2 for base inclinations η = 20°, 25°, and 29°. A typical test comprises three stages: (i) stabilization (2 hrs), (ii) thermal cycles (~10 hrs), and (iii) cooling (~6 hrs). A thermal cycle has amplitude ΔT = 9°C and period P = 34 min.

The initial temperature increase (ΔT ~ 15°C) expands the membrane ΔL. The measured elongation ΔL = 0.36 mm (Figure 6.2) agrees with the computed free thermal expansion $\Delta L = \alpha \cdot \Delta T \cdot L$ (for $\alpha = 3.2 \cdot 10^{-4}$ °C^{-1}). Additional temperature changes cause expansions and contractions that correlate with the heating and the cooling phases, resulting in membrane ratcheting displacement. The rate of accumulated displacement increases with the base inclination η and is linearly related to the number of thermal cycles (Figure 6.2).

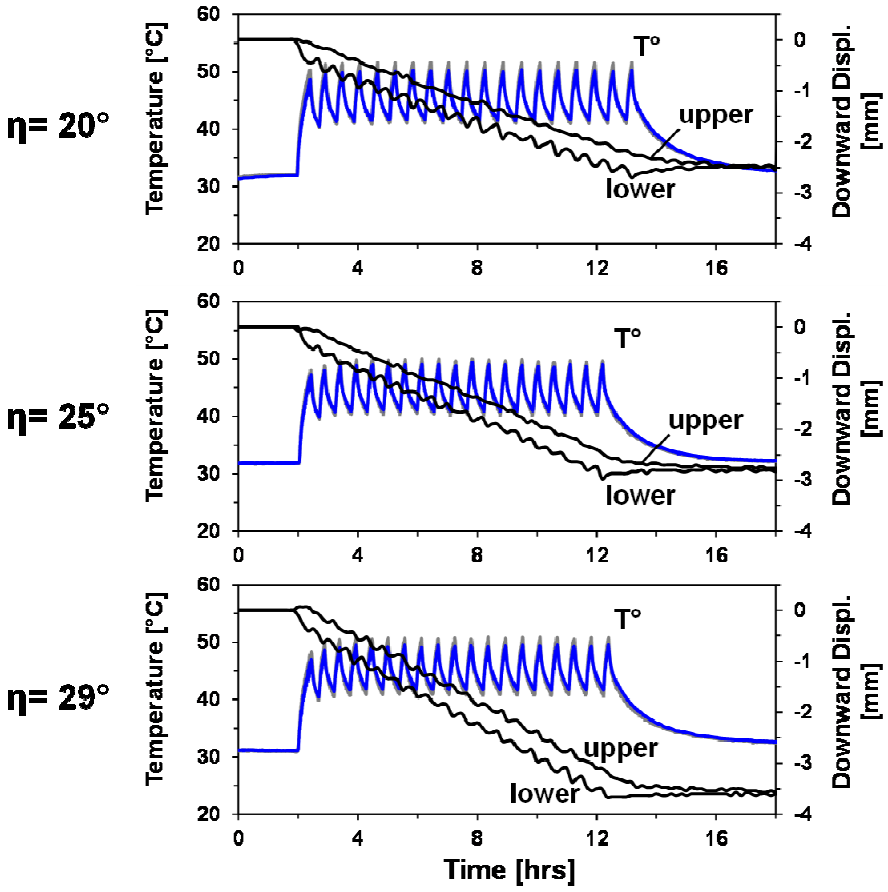

Figure 6.2 Thermally-induced geomembrane ratcheting displacement for various base inclinations angles η. Air temperature $T°$ is measured by two thermocouples shown in Figure 6.1. Displacements at points near the lower and upper edges of the membrane are determined from image processing.

6.3 Numerical Algorithm for Cyclic Thermal Loading

Let's analyze the membrane thermally-induced ratcheting displacement to identify the governing equations.

6.3.1 Global Static Equilibrium

Consider a geomembrane with longitudinal length L [m], width B [m], thickness t_h [m], and unit weight γ_m [N/m^3] resting on a plane inclined at an angle η [°]. Equilibrium requires that the shear stress τ [Pa] induced by the geomembrane weight along the

inclined plane is less than or equal to the shear strength τ_{max} [Pa] of the geomembrane-base interface. The component of the weight parallel to the plane causes a mean shear stress τ [Pa]

$$\tau = \gamma_m \cdot t_h \cdot \sin\eta \le \tau_{\max} = \mu \cdot \gamma_w \cdot t_h \cdot \cos\eta\,, \tag{6.1}$$

where μ [-] is the interface friction coefficient. Then, the static global factor of safety is

$$FS = \frac{\tau_{max}}{\tau} = \frac{\mu}{tan\eta}\ . \tag{6.2}$$

6.3.2 Element-Level Equilibrium and Compatibility

Repeated heating and cooling cycles alter the geomembrane static equilibrium. The geomembrane is discretized into N elements of length $L_0 = L/N$ [m]. The ith-element experiences a displacement δ_i [m] at its higher edge and δ_{i+1} [m] at its lower edge (Figure 6.3a).

Force equilibrium requires that the longitudinal force on the ith-element upper edge Q_i [N] plus the weight component parallel to the plane $W_i \cdot \sin\eta = (\gamma_m \cdot t_h \cdot L_0 \cdot B \cdot \sin\eta)$ equals the sum of the longitudinal force on its lower edge Q_{i+1} [N] and the shear force at the base interface S_i [N] (Figure 6.3):

$$Q_i = Q_{i+1} + S_i - W_i \cdot \sin\eta\ . \tag{6.3}$$

The shear force S_i is the shear stress on the ith-element τ_i [Pa] times the element base area $A_c = B \cdot L_0$ [m^2]:

$$S_i = \tau_i \cdot B \cdot L_0\,. \tag{6.4}$$

The shear stress τ_i [Pa] is assumed to have a linear-elastic-perfectly-plastic displacement response:

$$\tau_i = \tau_i(\delta_i, \delta_{i+1}) = \begin{cases} -\tau_{\max} & if \quad \delta_i < -\delta^* \\ k \cdot \left(\dfrac{\delta_i + \delta_{i+1}}{2}\right) & if \quad -\delta^* < \delta_i < \delta^* \\ \tau_{\max} & if \quad \delta^* < \delta_i \end{cases}, \tag{6.5}$$

where the limiting interface elastic displacement δ^* [m] defines the interface shear stiffness k_j [Pa/m] as

$$k = \frac{\tau_{\max}}{\delta^*}. \tag{6.6}$$

Consider a uniform membrane temperature increase. Thermal expansion of the ith-element is constrained by the longitudinal forces acting on the element. Displacement compatibility requires that the element shortening or elongation $\delta^{\Delta}_i = \delta_{i+1} - \delta_i$ [m] equals the free thermal expansion displacement δ^T_i [m] minus the elastic contraction δ^{σ}_i [m]:

$$\delta_i^{\Delta} = \delta_{i+1} - \delta_i = \delta_i^T - \delta_i^{\sigma}. \tag{6.7}$$

The free thermal expansion displacement δ^T_i [m] is a function of the thermal expansion coefficient α [°C^{-1}] and the temperature change amplitude ΔT [°C]:

$$\delta_i^T = \alpha \cdot \Delta T \cdot L_0, \tag{6.8}$$

whereas the elastic contraction of the element δ^{σ}_i [m] is inversely proportional to the geomembrane Young's modulus E [Pa]

$$\delta_i^{\sigma} = \frac{Q_i + Q_{i+1}}{2} \frac{L_0}{B \cdot t_h \cdot E}. \tag{6.9}$$

Combining equilibrium and compatibility conditions (Eqs. 6.3 and 6.7), the displacement of the ith-element upper edge δ_i can be solved as a function of the ith-element lower edge displacement δ_{i+1} and axial force Q_{i+1}:

$$\delta_i(\delta_{i+1}, Q_{i+1}) = \begin{cases} \delta_{i+1} + \dfrac{L_0}{2Bt_hE}\left(2Q_{i+1} - \tau_{max} BL_0 - W_i \sin\eta\right) - \delta_i^T & \text{if} \quad \left(\dfrac{\delta_i + \delta_{i+1}}{2}\right) \le -\delta^* \\ \dfrac{\delta_{i+1}\left(1 + \dfrac{{L_0}^2 k_i}{4t_hE}\right) + \dfrac{L_0}{Bt_hE} Q_{i+1} - \dfrac{L_0 W_i \sin\eta}{2Bt_hE} - \delta_i^T}{1 - \dfrac{{L_0}^2 k_i}{4t_hE}} & \text{if} \quad -\delta^* < \left(\dfrac{\delta_i + \delta_{i+1}}{2}\right) < \delta^* \\ \delta_{i+1} + \dfrac{L_0}{2Bt_hE}\left(2Q_{i+1} + \tau_{max} BL_0 - W_i \sin\eta\right) - \delta_i^T & \text{if} \quad \delta^* \le \left(\dfrac{\delta_i + \delta_{i+1}}{2}\right) \end{cases}. \tag{6.10}$$

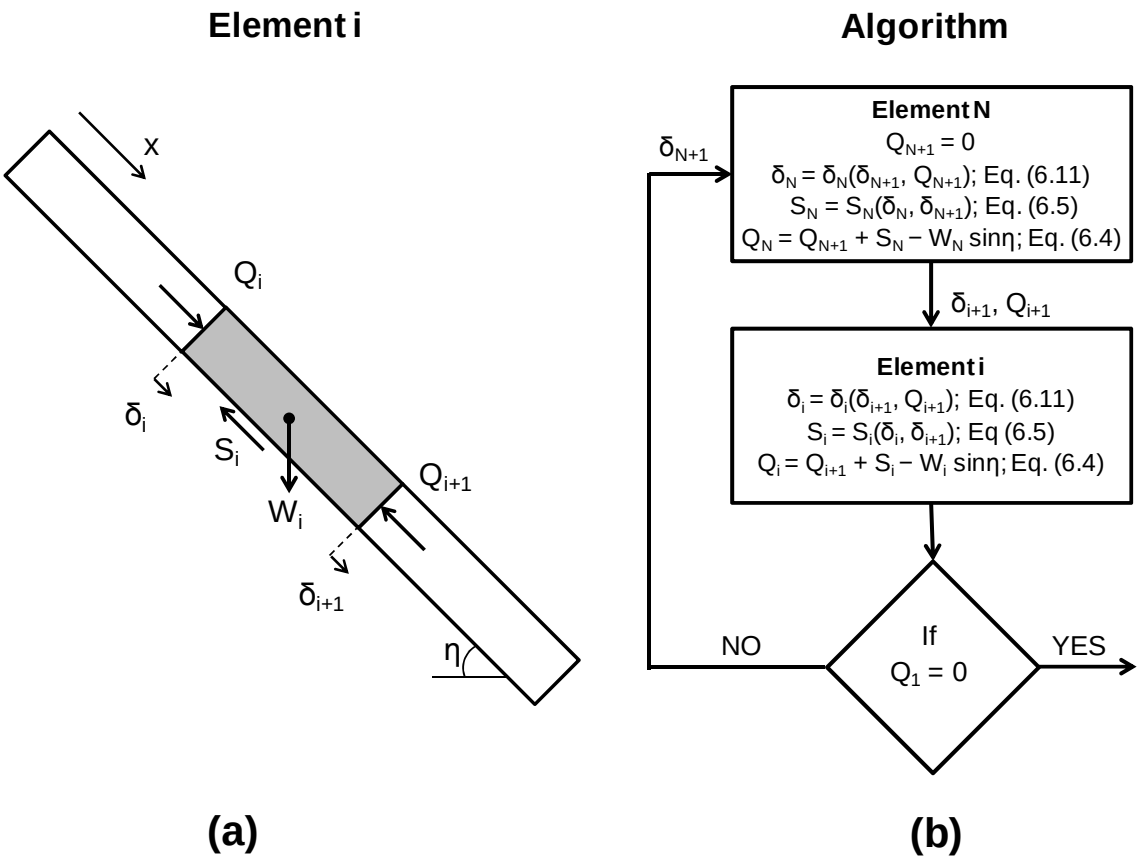

Figure 6.3 Numerical algorithm for a geomembrane subjected to temperature cycles. (a) Longitudinal forces Q, shear force at the interface S, and relative displacements δ in the ith-element. (b) The solution algorithm. The element weight is $W_i = \gamma_m \cdot t_h \cdot L_0 \cdot B$ (parameters in Table 6.1).

6.3.3 Numerical Algorithm

Equations (6.3) to (6.10) allow us to compute the evolution of geomembrane stresses and displacements during thermal cycles. The new equilibrium condition for the geomembrane subjected to a constant temperature change ΔT is calculated from the lowest element edge $i = (N+1)$ to the first edge $i = 1$ at the membrane top. The iterative algorithm follows (Figure 6.3b):

1. Impose a relative displacement at the Nth-element lower edge δ_{N+1} and compute the relative displacement at the Nth-element upper edge δ_N where $Q_{N+1} = 0$ (Eq. 6.10).
2. Calculate the Nth-element shear force S_N (Eqs. 6.4 and 6.5) and axial force acting at its upper edge Q_N (Eq. 6.3).
3. Use the relative displacement δ_N and the axial force Q_N to equilibrate the element $i = (N - 1)$. Then, continue element-by-element to reach the first element $i = 1$.
4. Verify the updated longitudinal force on the first element upper edge Q_1. If $|Q_1| > \varepsilon$, where ε [N] is a preselected tolerance value, repeat the iterative procedure for a different relative displacement value δ_{N+1} in step 1. If $|Q_1| \leq \varepsilon$, the solution has converged.

The initial static condition is obtained using $\delta^T_i = 0$ in Eq. (6.7) and results in zero longitudinal force in the membrane and homogeneous shear stress and relative displacement along the membrane-soil interface (Eq. 6.1).

6.3.4 Numerical Results

This numerical algorithm was used to study the behavior of geomembranes subjected to cyclic temperature changes. Thermal effects can be categorized according to the static factor of safety $FS = \mu/\tan\eta$ and the normalized free thermal displacement δ^T/δ^*, which is the ratio between the unconstrained thermal expansion of the geomembrane $\delta^T = \alpha \cdot \Delta T \cdot L$ and the critical interface displacement δ^*.

Ratcheting Displacement and Number of Cycles

Figure 6.4 shows the membrane upper edge displacement δ_1 as a function of the number of thermal cycles for various factors of safety FS and thermal amplitudes ΔT. The ratcheting displacement (i) evolves linearly with the thermal cycles, (ii) increases as the factor of safety decreases, and (iii) increases with the thermal amplitude.

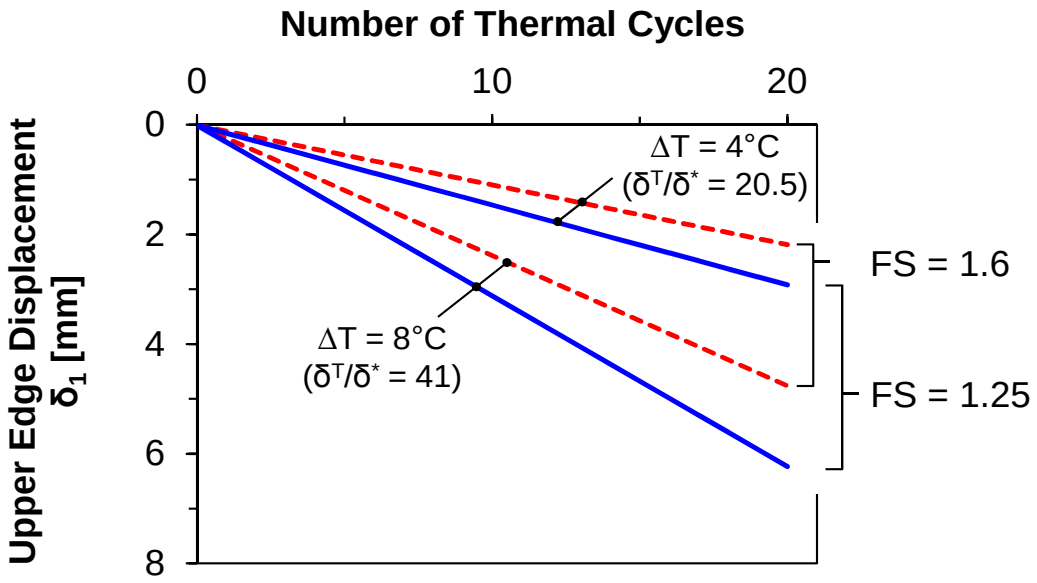

Figure 6.4 Evolution of membrane upper edge displacement δ_1 with the number of thermal cycles for various factors of safety *FS* and temperature change amplitudes ΔT. Note: Geomembrane parameters in Table 6.1.

Load-Transfer Curves

Load-transfer curves for a factor of safety *FS* = 1.6 and various normalized free thermal displacements δ^T/δ^* are shown in Figure 6.5. The low thermal displacement δ^T/δ^* = 0.5 does not cause plastic displacement accumulation because the critical interface displacement is not exceeded anywhere along the geomembrane interface. The intermediate thermal displacement δ^T/δ^* = 2.0 accumulates plastic displacement at a limited rate since the critical interface displacement is overcome in less than half of the membrane length. Finally, the large thermal displacement δ^T/δ^* = 20.5 results in downward membrane ratcheting displacement because the critical interface displacement is exceeded in more than half of the membrane length in both heating and cooling phases. Membrane thermal expansion and contraction cause (1) reversal of relative displacements with respect to the neutral point, (2) translation of the neutral point that does not change

during thermal cycles, and (3) linear accumulation of displacements with the number of thermal cycles. In the three cases, the longitudinal normal stress $\sigma = Q/(t_h \cdot B)$ and shear stress at the interface reverse during a heating-cooling cycle and remain unchanged with subsequent cycles.

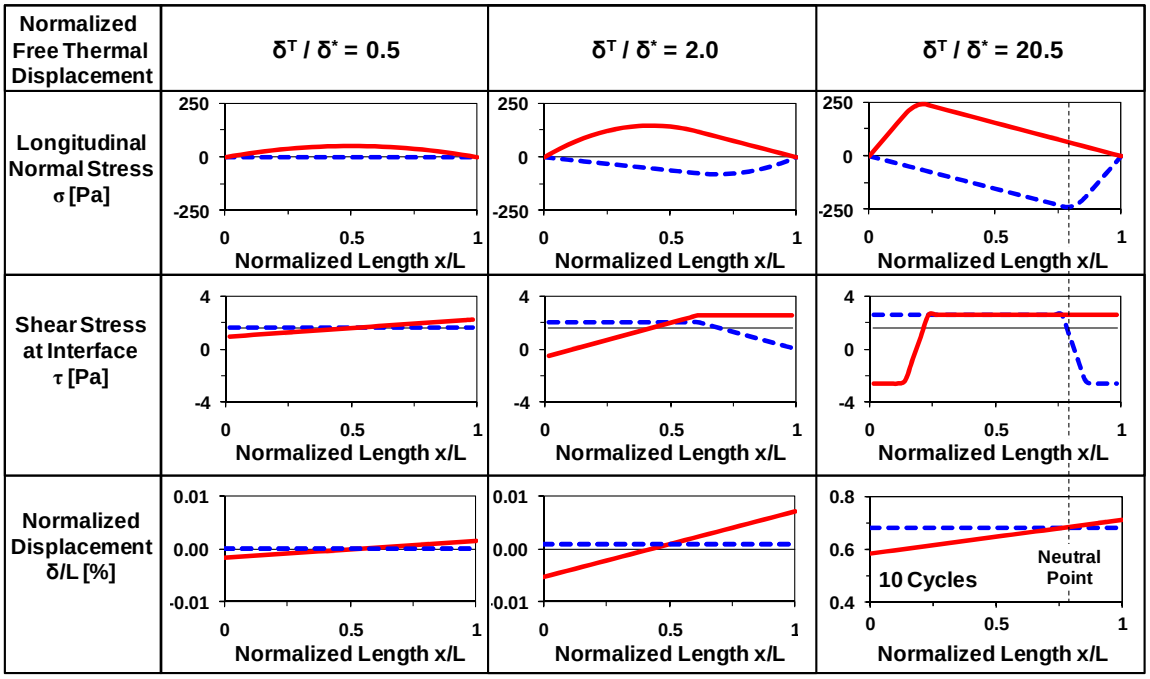

Figure 6.5 Characteristic load-transfer curves for cyclic temperature changes obtained with the numerical algorithm: Longitudinal normal stress σ, shear stress at the interface τ, and normalized interface relative displacement δ/L. Continuous curves correspond to heating phase and dotted lines to cooling phase. Normalized free thermal displacement δ^T/δ^* increases from left to right. Normalized displacement curves δ/L for δ^T/δ^* = 0.5 and 2.0 are independent of the number of thermal cycles. Note: $FS = \mu/\tan\eta$ = 1.6; geomembrane parameters in Table 6.1.

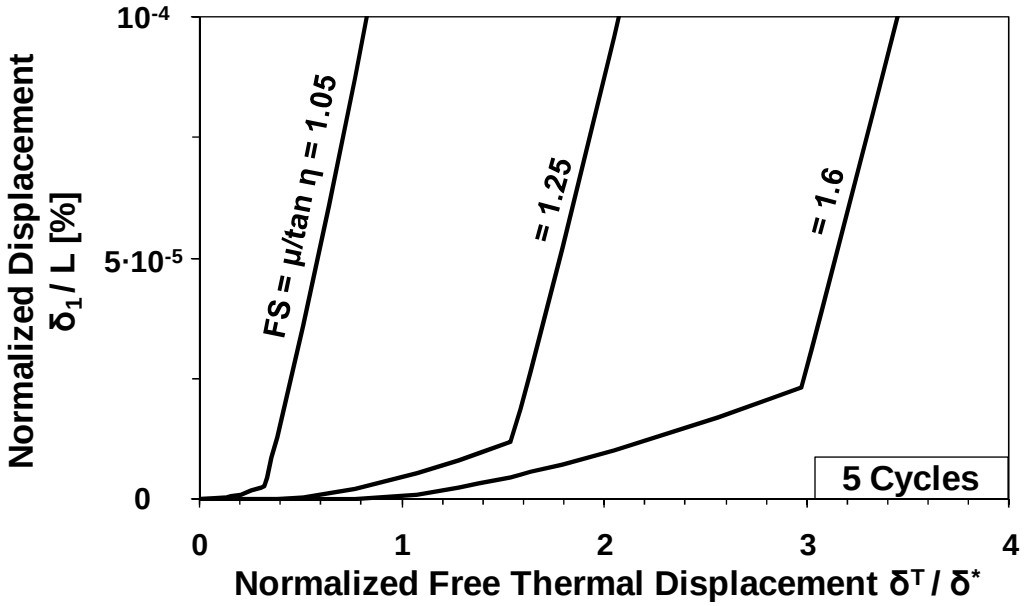

Figure 6.6 Normalized ratcheting displacement of the membrane upper edge δ_1/L after five thermal cycles as a function of the normalized free thermal displacement δ_T/δ^* and various static factors of safety $FS = \mu/\tan\eta$. Note: geomembrane parameters in Table 6.1.

Critical Thermal Displacements

Figure 6.6 summarizes normalized ratcheting displacements of the membrane upper edge δ_1/L after five thermal cycles as a function of the normalized free thermal displacement δ_T/δ^*. Critical displacements that define small, intermediate, and large thermal displacement behaviors are $\delta^T/\delta^* = 0.8$ and $\delta^T/\delta^* = 3.0$ for a factor of safety $FS = 1.6$. Critical values decrease as the factor of safety decreases. In other words, smoother membrane-soil interfaces and steeper base inclinations require lower thermal amplitudes to experience ratcheting displacement.

Displacement Accumulation Rates

Displacement accumulation rates are shown as a function of the factor of safety $FS = \mu/\tan\eta$ and the normalized thermal displacement δ^T/δ^* in Figure 6.7. The figure

shows that ratcheting displacement after 100 thermal cycles increases as the static factor of safety *FS* decreases (i.e., steeper slopes) and the normalized free thermal expansion displacement δ^T/δ^* increases (i.e., high temperature changes ΔT or long membranes). For instance, a membrane on a slope with a factor of safety *FS* = 1.6 subjected to a cyclic thermal amplitude ΔT = 4 °C (i.e., δ^T/δ^* = 20) experiences an accumulated displacement $\Delta\delta_1 = 6.6\%\cdot L$ every 100 thermal cycles.

Other Observations

The parametric study also shows that ratcheting displacement is not affected by the membrane width *B* or thickness t_h (buckling and wrinkle formation are not considered), but it is proportional to the membrane Young's modulus *E*. The evolution of membrane ratcheting displacements depends on the thermal amplitude ΔT and is independent of the first temperature change polarity and the cyclic mean temperature.

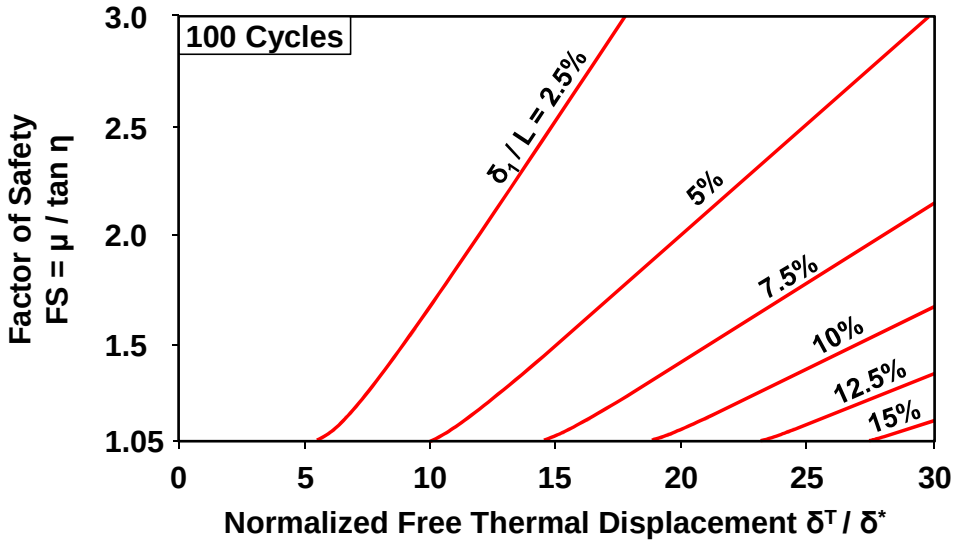

Figure 6.7 Ratcheting displacement of the membrane upper edge δ_1/L after 100 thermal cycles as a function of the static factor of safety $FS = \mu/\tan\eta$ and the normalized free thermal displacement δ_T/δ^*. Note: geomembrane parameters in Table 6.1.

6.4 Discussion: Extension to Field Situations

6.4.1 Large-Scale Geomembranes

Field evidence of thermally induced membrane ratcheting can be found in the literature (Chappel et al. 2008; Rowe 2011). For comparison, consider a high-density polyethylene HDPE geomembrane resting on a 3:1 slope, i.e., $\eta \sim 18°$, (membrane length L = 20m, thickness t_h = 1.5 mm, Young's modulus E = 250 MPa, thermal expansion coefficient $\alpha = 2 \cdot 10^{-4}$ °C^{-1}, interface friction coefficient μ = 0.47, and critical interface displacement δ^* = 5 mm). Numerical results using the algorithm above indicate that the geomembrane accumulates ratcheting displacement at a rate of 45 mm per thermal cycle if the thermal amplitude is ΔT = 20°C.

The longitudinal normal stress increases in the membrane due to constrained thermal expansion, particularly in the lower part (Figure 6.5 – x/L ~ 0.8, δ^T/δ^* = 20.5). High normal stresses favor wrinkle formation towards the membrane lower end, as observed in the field (Chappel et al. 2008; Rowe et al. 2012). The numerical model can be modified to account for wrinkle formation by including a critical longitudinal buckling force (Giroud and Morel 1992).

6.4.2 Natural Rock Slopes

Natural rock slopes subjected to temperature changes experience plastic displacement accumulation (Grøneng et al. 2011; Gunzburger et al. 2005). The proposed thermo-mechanical formulation is used to explore thermally-induced ratcheting displacement in rock slopes. In this case, the thickness involved in thermal expansion is the rock skin depth S_d [m], which is a function of the thermal cycle period T_0 [s], the material thermal conductivity k_T [W/m/K], specific heat c_p [J/kg/K], and mass density ρ [kg/m^3] (Turcotte and Schubert 2002):

$$S_d = \sqrt{\frac{k_T}{\rho \cdot c_p} \frac{T_0}{\pi}} \quad . \tag{6.11}$$

Typical properties for dolomite (k_T = 4 W/m/K, c_p = 900 J/kg/K, and ρ = 2550 kg/m^3 - See Table 5.2) yield S_d = 0.22 m for a daily temperature change (T_0 = 1 day) and S_d = 4.2 m for a seasonal temperature change (T_0 = 365 days).

A rock slab (length L = 5 m, Young's modulus E = 50 GPa, thermal expansion coefficient α = 8·10^{-6} °C^{-1}, interface friction coefficient μ = 0.5, critical interface displacement δ^* = L/2000 = 2.5 mm, and base inclination η = 25°, i.e., FS = μ/tanη = 1.07), may experience ratcheting displacement if it is subjected to a temperature change larger than ΔT = 35°C. This critical temperature increases to ΔT = 135°C if the base inclination decreases to η = 20° (FS = 1.37). These results suggest that thermally-induced displacements can cause ratcheting displacement in natural slopes for typical temperature variations when the base inclination is close to the critical value $\eta \sim \tan\varphi$. Thermally-induced ratcheting displacement can be enhanced by wedging, as described in Chapter 5.

6.5 Conclusions

Exposed geomembranes expand and contract when subjected to cyclic thermal changes. Experimental results show that thermally-induced displacements in exposed geomembranes resting on inclined planes can result in the accumulation of plastic downward displacements. Thermally-induced ratcheting displacement increases with the base inclination angle η and continues accumulating with the number of thermal cycles.

Governing equations are captured in a numerical algorithm that considers the thermo-elastic membrane properties, a constant temperature change amplitude, and a linear elastic-perfectly plastic constitutive model with constant critical displacements for the membrane-soil interface. Numerical results corroborate thermal ratcheting and anticipate conditions for wrinkle formation in situ.

The membrane experiences downward ratcheting displacement when the critical interface displacement δ^* is exceeded in more than half of the membrane length in a heating or cooling phase. The critical thermal displacement δ^T required to overcome the critical interface displacement decreases as the inclination angle increases and the soil-membrane interface friction coefficient decreases. The magnitude of ratcheting displacement increases as the factor of safety decreases and increases with the number and amplitude of thermal cycles.

The application of the numerical algorithm is extended to analyze the behavior of natural rock slopes subjected to thermal cycles. Numerical results show that rock slabs are likely to experience downward ratcheting displacement for typical daily and seasonal temperature changes only if the inclination angle η is close to the critical value $\eta = \tan\varphi$. Wedging can enhance thermally-induced ratcheting displacements, as described in Chapter 5.

CHAPTER 7

THERMALLY-INDUCED LONG-TERM DISPLACEMENT OF ENERGY PILES

7.1 Introduction

Energy piles can reduce fossil fuel consumption for low-grade energy needs, such as air conditioning and water heating in buildings. Energy piles are structural elements equipped with pipe loops connected to a heat pump to exchange heat between a building and the soil mass surrounding the foundation. The thermal inertia of the soil mass absorbs excess heat released from the building during the summer and returns heat to the building during the winter (Brandl 2006).

Repetitive heat absorption-rejection causes thermo-mechanical pile-soil interaction (Amatya et al. 2012; Bourne-Webb et al. 2012; Knellwolf et al. 2011; Laloui et al. 2006; McCartney 2011). Constrained thermal expansion of the pile upon heating, bias shear displacement due to the building static load, and the elasto-plastic nature of the pile-soil interface may result in the accumulation of plastic pile displacements. While the ultimate pile capacity may remain constant, the accumulation of thermally-induced plastic displacements can affect the long-term energy pile performance.

This study analyzes the long-term response of energy piles using a one-dimensional load-transfer formulation, modified to consider thermo-plastic effects. The influence of material parameters, the static load, the ultimate shaft resistance, and the number of thermal cycles are examined for various temperature change amplitudes.

7.2 Numerical Algorithm for Cyclic Thermal Loading

The 1D pile-soil load-transfer method (Coyle and Reese 1966; Poulos and Davis 1980) is modified to account for temperature change (similar to the formulation in Knellwolf et al. 2011).

7.2.1 Element-Level Equilibrium and Compatibility

Consider a pile, length L [m] and diameter D [m], discretized into N elements length $L_0 = L/N$ [m] and (N+1) interfaces. The static axial force applied on the pile head is $Q_1 = Q^{head}$ [N]. The position of the ith-element is defined by the relative displacement of its upper interface δ_i [m] and its lower interface δ_{i+1} [m] (Figure 7.1a). Force equilibrium requires that the axial force on the ith-element upper interface Q_i [N] equals the sum of the axial force on its lower interface Q_{i+1} [N] and the shaft resistance S_i [N]:

$$Q_i = Q_{i+1} + S_i . \tag{7.1}$$

The shaft resistance S_i is the side friction acting on the ith-element s_i [Pa] times the element contact area $A_c = \pi \cdot D \cdot L_0$ [m^2]:

$$S_i = s_i \cdot \pi \cdot D \cdot L_0 . \tag{7.2}$$

The side friction s_i [Pa] is assumed to have a linear-elastic-perfectly-plastic displacement response:

$$s_i = s_i\left(\delta_i, \delta_{i+1}\right) = \begin{cases} -s_i^{ult} & if \quad \left(\dfrac{\delta_i + \delta_{i+1}}{2}\right) \le -\delta_s^* \\ k_i \cdot \left(\dfrac{\delta_i + \delta_{i+1}}{2}\right) & if \quad -\delta^* < \left(\dfrac{\delta_i + \delta_{i+1}}{2}\right) < \delta_s^* \\ s_i^{ult} & if \quad \delta_s^* \le \left(\dfrac{\delta_i + \delta_{i+1}}{2}\right) \end{cases}, \tag{7.3}$$

where $k_i = s_i^{ult} / \delta_s^*$ [Pa/m] is the shaft stiffness and δ_s^* [m] is the critical relative displacement to mobilize the pile-soil shear strength s_i^{ult} [Pa].

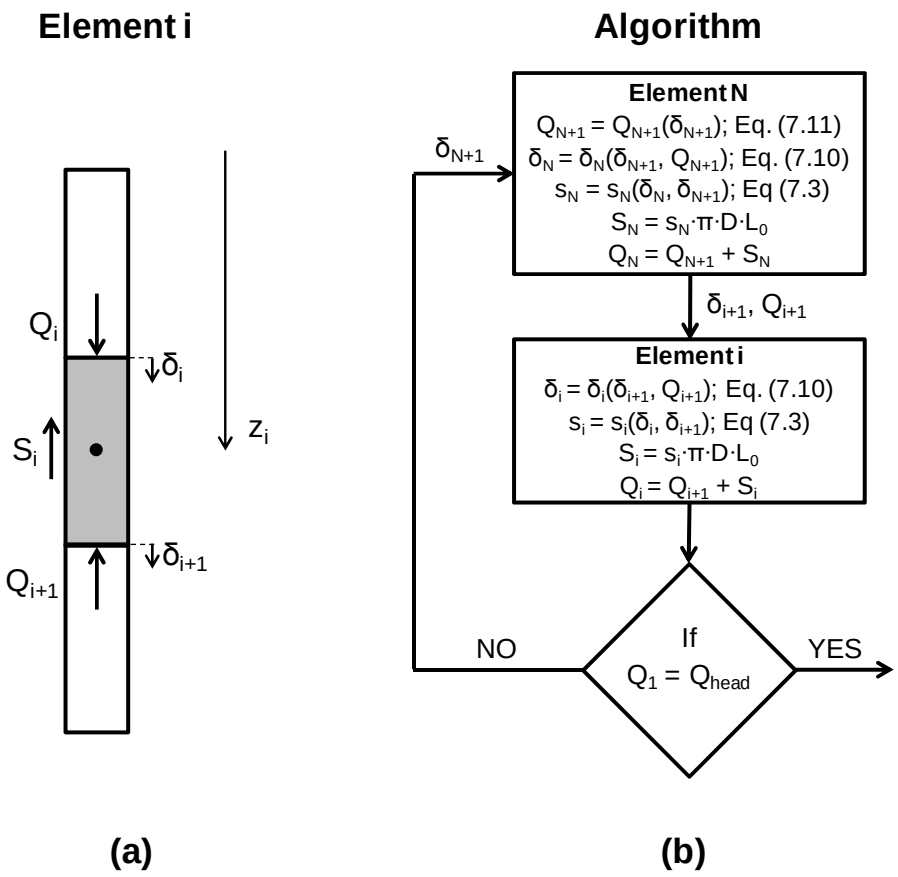

Figure 7.1 Numerical algorithm for a pile subjected to static vertical load and thermal cycles. (a) Axial forces Q and shaft resistance S acting on the ith-element cause interface relative displacements δ. The ith-element middle point is z_i. (b) Solution algorithm.

The pile-soil shear strength at the ith-element s_i^{ult} [Pa] is the horizontal effective stress acting on the element $\sigma'_{hi} = \sigma'_{vi} \cdot K_0$, where σ'_{vi} [Pa] is the vertical effective stress and K_0 [-] is the coefficient of horizontal stress, times the pile-soil interface friction coefficient μ [-]:

$$s_i^{ult} = \sigma'_v \cdot K_0 \cdot \mu \ . \tag{7.4}$$

The vertical effective stress is a function of the soil unit weight γ [N/m^3] and the depth of the ith-element middle point z_i [m] (Figure 7.1a):

$$\sigma'_v = \gamma \cdot z_i \,. \tag{7.5}$$

For bored piles with a rough concrete-soil interface, the coefficient of horizontal stress can be estimated as $K_0 = (1 - \sin\varphi)$ and the pile-soil interfacial friction coefficient as $\mu = \tan\varphi$ with φ the soil friction angle. The ultimate pile shaft resistance S^{ult} [N] is

$$S^{ult} = L_0 \cdot \pi \cdot D \cdot \sum_i^N s_i^{ult} \quad . \tag{7.6}$$

Consider a uniform pile temperature increase. Thermal expansion of the ith-element is constrained by the axial forces acting on the element. Displacement compatibility requires that the total element displacement $\delta^{\Delta}_i = \delta_{i+1} - \delta_i$ [m] is the free thermal expansion displacement δ^T_i [m] minus the elastic contraction δ^{σ}_i [m]:

$$\delta_i^{\Delta} = \delta_{i+1} - \delta_i \; = \delta_i^T - \delta_i^{\sigma} \,. \tag{7.7}$$

The free thermal expansion displacement δ^T_i [m] is computed with the thermal expansion coefficient α [°C^{-1}], the temperature change amplitude ΔT [°C], and the element length L_0 [m]:

$$\delta_i^T = \alpha \cdot \Delta T \cdot L_0 \,. \tag{7.8}$$

The elastic contraction is

$$\delta_{\sigma i} = \frac{Q_i + Q_{i+1}}{2} \frac{L_0}{A \cdot E} \,, \tag{7.9}$$

where A [m^2] is the pile transverse area and E [Pa] is the pile Young's modulus.

Combining equilibrium and compatibility conditions (Eqs. 7.1 and 7.7), the displacement of the ith-element upper interface δ_i is obtained as a function of the ith-element lower interface displacement δ_{i+1} and axial force Q_{i+1}:

$$\delta_i\left(\delta_{i+1},Q_{i+1}\right)=\begin{cases}\delta_{i+1}+\dfrac{L_0}{2AE}\left(2Q_{i+1}-\pi DL_0 s_i^{ult}\right)-\delta_i^T & if \quad \left(\dfrac{\delta_i+\delta_{i+1}}{2}\right)\le -\delta_s^* \\ \dfrac{\delta_{i+1}\left(1+\dfrac{{L_0}^2\pi Dk_i}{4AE}\right)+\dfrac{L_0}{AE}Q_{i+1}-\delta_i^T}{1-\dfrac{{L_0}^2\pi Dk_i}{4AE}} & if \quad -\delta_s^*<\left(\dfrac{\delta_i+\delta_{i+1}}{2}\right)<\delta_s^* \\ \delta_{i+1}+\dfrac{L_0}{2AE}\left(2Q_{i+1}+\pi DL_0 s_i^{ult}\right)-\delta_i^T & if \quad \delta_s^*\le\left(\dfrac{\delta_i+\delta_{i+1}}{2}\right)\end{cases}. \quad (7.10)$$

The pile tip resistance Q_{N+1} [N] is assumed linear-elastic-perfectly-plastic with a constant critical relative displacement δ_b^* [m] to mobilize the ultimate tip resistance Q^{ult}_{N+1} [N]:

$$Q_{N+1}=Q_{N+1}\left(\delta_{N+1}\right)=\begin{cases}\left(\dfrac{Q_{N+1}^{ult}}{\delta_b^*}\right)\delta_{N+1} & if \quad 0<\delta_{N+1}<\delta_b^* \\ Q_{N+1}^{ult} & if \quad \delta_b^*<\delta_{N+1}\end{cases}. \quad (7.11)$$

The ultimate pile capacity Q^{ult} [N] is the sum of the shaft and the tip resistances:

$$Q^{ult}=S^{ult}+Q_{N+1}^{ult}. \quad (7.12)$$

Finally, the static global factor of safety is

$$FS=\frac{Q^{ult}}{Q^{head}}. \quad (7.13)$$

7.2.2 Numerical Algorithm

Equations (7.1) to (7.11) allow tracking the evolution of pile stresses and displacements during thermal cycles. The equilibrium condition for the pile subjected to a constant temperature change ΔT is calculated from the lowest interface at the pile tip i = (N + 1) to the first interface at the pile head i = 1. The iterative algorithm follows:

1. Impose a relative displacement at the Nth-element lower interface δ_{N+1} and compute the corresponding tip resistance Q_{N+1} (Eq. 7.11).

2. Compute the relative displacement at the Nth-element upper interface δ_N (Eq. 7.10).
3. Calculate the Nth-element shaft resistance S_N (Eqs. 7.2 and 7.3) and axial force on its upper interface Q_N (Eq. 7.1).
4. Continue element-by-element to reach the first interface $i = 1$.
5. Compare the computed value of the longitudinal force on the first interface Q_1 with the applied static force Q^{head}. If $|Q_1 - Q^{head}| > \varepsilon$, where ε [N] is a preselected tolerance value, the iterative procedure is repeated for a different relative displacement δ_{N+1} in step 1. If $|Q_1 - Q^{head}| \leq \varepsilon$, the solution has converged.

The load-transfer curves for the static load without heating are obtained using $\delta^T_i = 0$ in Eq. (7.10). The application of thermal cycles is imposed once the static load at the pile head is equilibrated. Thermal cycles consist of a sequence of positive or negative temperature changes using the algorithm described above.

7.3 Numerical Results

The behavior of a pile subjected to cyclic thermal changes is analyzed next. The cyclic temperature change amplitude ΔT is assumed constant along the pile in agreement with results from instrumented piles (Bourne-Webb et al. 2009; Laloui et al. 2006). The analyzed pile represents a bored cast-in-place pile without residual stresses after installation. The selected pile length $L = 20$ m is common among energy piles as the soil temperature remains relatively unaffected by daily and seasonal weather changes at such depths (Brandl 2006).

The ultimate shaft resistance is mobilized at comparatively small relative displacements, ranging from $\delta^* = 0.005 \cdot D$ to $0.02 \cdot D$ (Hirayama 1990; Reese 1978). In contrast, bored cast-in-place piles, or non-displacement piles, require a large tip displacement to mobilize the ultimate base resistance. It is assumed that $\delta_s^* = 0.005 \cdot D$

and $\delta_b^* = 0.1 \cdot D$, so the critical shaft-to-base displacement ratio is $\delta_b^*/\delta_s^* = 20$. The set of parameters used in the numerical simulation are summarized in Table 7.1.

7.3.1 Load-Transfer Curves

Figure 7.2 compares the load-transfer curves after static loading and cyclic thermal loading for a temperature change amplitude ΔT = 40°C, shaft-to-ultimate resistance ratio $S^{ult}/Q^{ult} = 0.5$, and static-to-ultimate load ratio $Q^{head}/Q^{ult} = 0.5$ (i.e., factor of safety FS = 2.0). The pile axial force Q, side friction s, and relative displacement δ evolve with the number of thermal cycles. Heating expands the upper part of the pile upward and the lower part downward. Thermal contraction upon cooling partially reverses this trend. Consequently, plastic displacements accumulate, and the neutral point moves upward with the number of thermal cycles.

Table 7.1 Parameters Used in Numerical Simulations

Parameter	Symbol	Units	Value
Pile diameter [(a)]	D	[m]	1.0
Pile Young's modulus [(b)]	E	[GPa]	30
Pile thermal expansion coefficient	α	[10^{-5}/°C]	1
Critical shaft displacement	δ_s^*	[m]	0.005 D
Critical base displacement	δ_b^*	[m]	0.1 D
Pile length	L	[m]	20
Soil unit weight	γ	[kN/m^3]	18

Notes: (a) Not smaller than 0.6m to allow space for the heat exchanger tubing (McCartney 2011)
(b) Equivalent to reinforced concrete (Laloui et al. 2006)

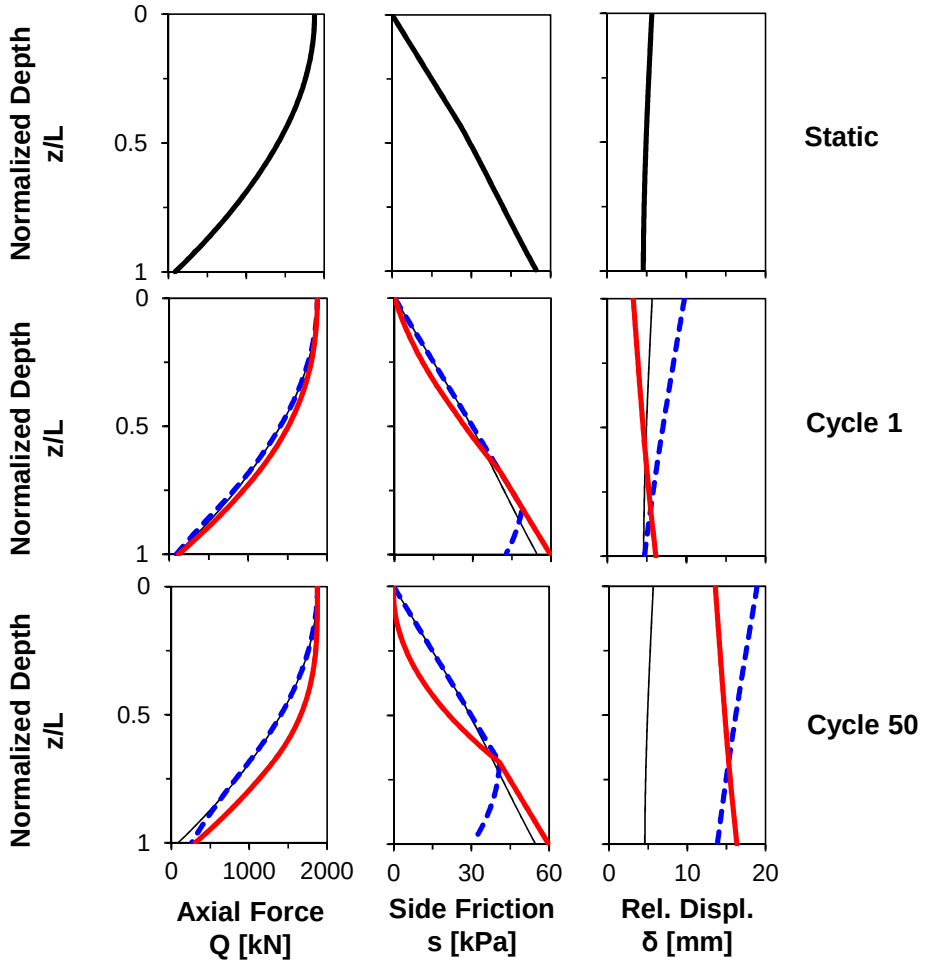

Figure 7.2 Load-transfer curves after static loading and thermal cycling. Axial force Q, side friction s, and relative displacement δ were calculated as a function of the normalized depth z/L for ΔT = 40°C, Q^{ult} = 3,750 kN, S^{ult}/Q^{ult} = 0.5, and Q^{head}/Q^{ult} = 0.5 (i.e., FS = 2.0). Continuous curves correspond to heating phase and dotted lines to cooling phase. Note: Pile parameters in Table 7.1; pile segments N = 100.

7.3.2 Shaft- and End-Bearing Piles

The evolution of pile head displacement with the number of thermal cycles in both end-bearing (S^{ult}/Q^{ult} = 0.2) and shaft-bearing piles (S^{ult}/Q^{ult} = 0.7) are compared in Figure 7.3a. Pile head displacements are normalized by the critical relative displacement required to mobilize the pile-soil interface shear strength δ_s^* = 5 mm. This value is

almost twice as small as the free thermal displacement of the unconstrained pile $\delta^T = \alpha \cdot \Delta T \cdot L$ = 8 mm when the temperature change amplitude is ΔT = 40°C. The end- and shaft-bearing piles with normalized head load Q^{head}/Q^{ult} = 0.2 (i.e., factor of safety FS = 5) do not accumulate permanent displacements after the static load is applied. However, piles with Q^{head}/Q^{ult} = 0.8 (FS = 1.25) accumulate displacements with the number of thermal cycles until reaching asymptotic displacements $\delta_1|_{Nc\to\infty}$. The end-bearing pile settles less than the shaft-bearing pile and reaches the asymptotic displacement at fewer cycles for similar normalized head loads. The evolution of pile head displacements is independent of the first temperature change if the cyclic mean temperature is zero.

Asymptotic pile head displacements $\delta_1|_{Nc\to\infty}$ as a function of the normalized head load $Q^{head}/Q^{ult} = FS^{-1}$ are compared with static load-displacement curves in Figure 7.3b. If a critical static load is exceeded ($Q^{head}/Q^{ult} \sim 0.2$ for an end-bearing pile and $Q^{head}/Q^{ult} \sim 0.6$ for a shaft-bearing pile), thermal cycles induce asymptotic pile settlements. The asymptotic load-displacement curves are parallel to the static curves, and the shifts are linearly proportional to the temperature change amplitude ΔT.

7.3.3 Pile Displacement with Thermal Cycles

The pile head displacement after N_c thermal cycles $\delta_1|_{Nc}$ can be fitted with an exponential function in terms of the head displacement for the static load $\delta_1|_{Nc=1}$ and the asymptotic head displacement $\delta_1|_{Nc\to\infty}$:

$$\delta_1\big|_{Nc} = \delta_1\big|_{Nc\to\infty} + \left(\delta_1\big|_{Nc=1} - \delta_1\big|_{Nc\to\infty}\right)\exp\left(-\alpha \cdot N_c\right). \tag{7.14}$$

The exponent α captures the convergence rate towards the asymptotic pile head displacement and decreases as the shaft-to-ultimate resistance ratio S^{ult}/Q^{ult} increases (Figure 7.4). The critical number of cycles N^* required to achieve 63% of the pile settlement from the initial static displacement to the asymptotic displacement ($\delta_1|_{Nc\to\infty} - \delta_1|_{Nc=1}$) can be obtained from Eq. (7.14) as $N^* = 1/\alpha$. For example, an end-bearing pile (S^{ult}/Q^{ult} = 0.2) with a normalized head load Q^{head}/Q^{ult} = 0.8 (FS = 1.25) has an exponent

α = 0.675 and a critical number of cycles $N^* \sim 2$, whereas a shaft-bearing pile (S^{ult}/Q^{ult} = 0.7) with identical head load has an exponent α = 0.103 and $N^* \sim 10$. Note that this exponential asymptotic trend only applies to piles with high head loads Q^{head}/Q^{ult} that reach a shakedown condition with thermal cycles.

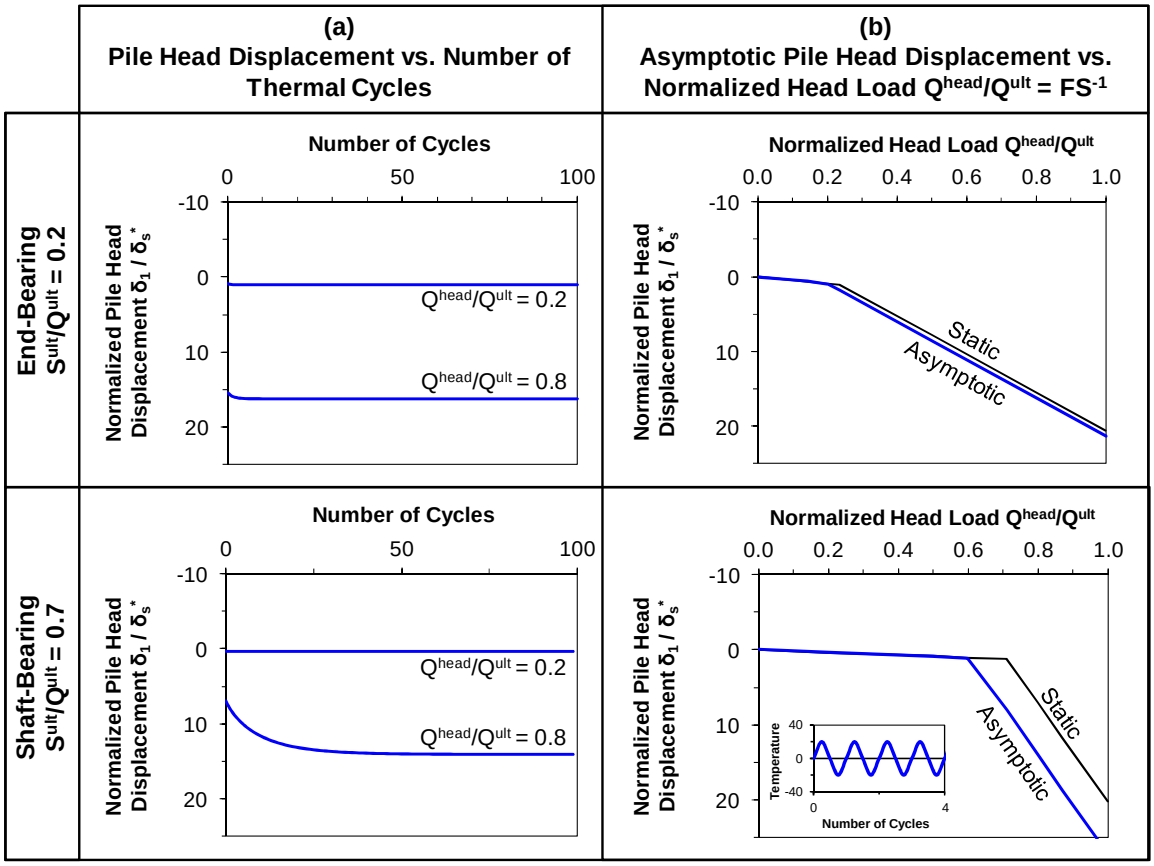

Figure 7.3 Evolution of pile head displacements and asymptotic values for end- and shaft-bearing piles subjected to unbiased thermal cycles. The temperature change amplitude is ΔT = 40°C and the ultimate pile capacity is Q^{ult} = 3,750 kN. Note: Pile parameters are found in Table 7.1. The ultimate tip resistance is $Q^{ult}_{N+1} = Q^{ult} - S^{ult}$.

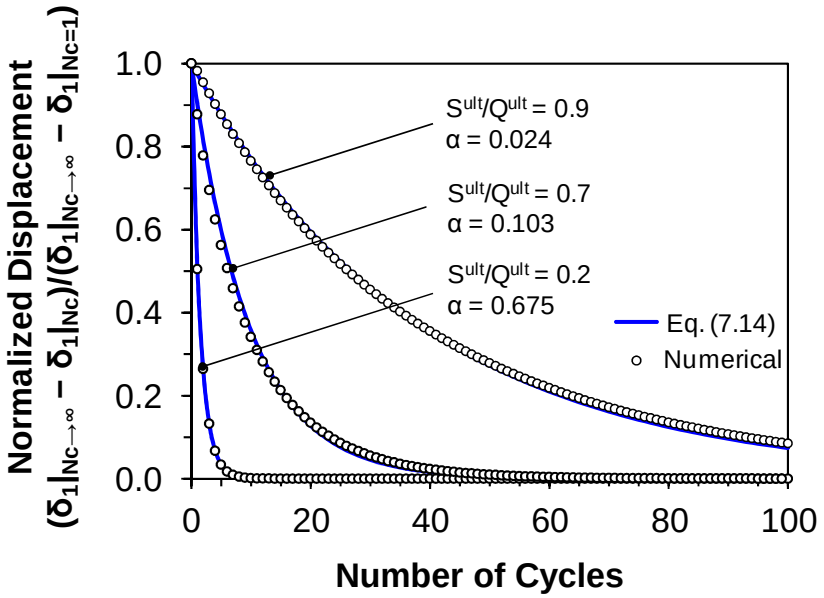

Figure 7.4 Evolution of the normalized pile head displacement with the number of thermal cycles for various shaft-to-ultimate resistance ratios S^{ult}/Q^{ult}. The exponent α is defined in Eq. (7.14).

7.3.4 Biased Thermal Cycles

Figure 7.5 compares the evolution of pile head displacement with the number of thermal cycles in both end-bearing (S^{ult}/Q^{ult} = 0.2) and shaft-bearing (S^{ult}/Q^{ult} = 0.7) piles subjected to thermal cycles with either positive or negative mean values. End- and shaft-bearing piles with a low head load (Q^{head}/Q^{ult} = 0.2) experience upward ratcheting displacement when subjected to thermal cycles with positive mean and downward ratcheting displacement when subjected to thermal cycles with negative mean. End- and shaft-bearing piles with a high head load (Q^{head}/Q^{ult} = 0.8) reach asymptotic displacements when subjected to thermal cycles with positive mean and experience downward ratcheting displacement when subjected to thermal cycles with negative mean. For clarity, a negatively-biased thermal change may occur during initial pile operation in the winter season.

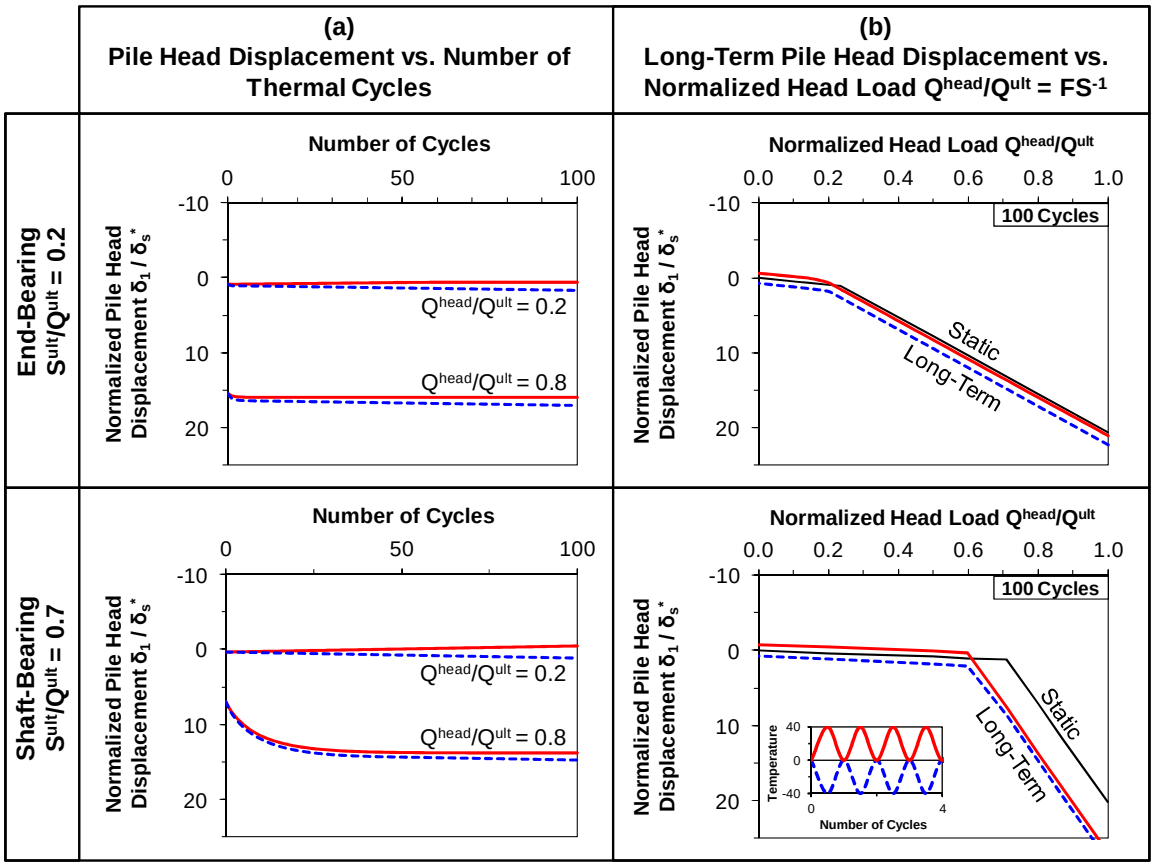

Figure 7.5 Evolution of pile head displacements and long-term values for end- and shaft-bearing piles subjected to biased thermal cycles. The temperature change amplitude is ΔT = 40°C and the ultimate pile capacity is Q^{ult} = 3,750 kN. Note: Pile parameters are found in Table 7.1; the ultimate tip resistance is $Q^{ult}_{N+1} = Q^{ult} - S^{ult}$.

Figure 7.5b shows long-term load displacement curves of piles subjected to thermal cycles with positive and negative mean values after N_c = 100 cycles. Both curves remain parallel to the static load-displacement curve, yet displacement accumulation increases with the number and amplitude of the thermal cycles for a negative thermal bias.

7.3.5 Ratcheting and Shakedown Behavior – Summary

The long-term response of energy piles subjected to thermal cycles is summarized in Figure 7.6. A pile response depends on the mean and the amplitude of thermal cycles

(Figure 7.6a), the static head load Q^{head} (Figure 7.6b), and the shaft-to-ultimate resistance ratio S^{ult}/Q^{ult} (Figures 7.6b and 7.6c). Unbiased thermal cycles always cause shakedown settlement, and the asymptotic displacements increase with the temperature change amplitude. In contrast, thermal cycles with negative mean values always cause downward ratcheting displacements, which increase with the number and amplitude of the thermal cycles. Finally, thermal cycles with positive mean values can cause both upward ratcheting and shakedown depending on the static head load Q^{head} and the shaft-to-ultimate resistance ratio S^{ult}/Q^{ult}. The boundary between both behaviors moves to the left as the amplitude of thermal cycles increases. Although small thermal amplitudes promote upward ratcheting behavior, the effect is hindered by the small rate of displacement accumulation.

7.3.6 General Observations

Additional parametric studies were conducted to explore a wide range of conditions. Observations from these studies include:

- Purely shaft-bearing piles ($S^{ult}/Q^{ult} = 1$) subjected to thermal cycles with zero mean and purely end-bearing piles ($S^{ult}/Q^{ult} = 0$) deform elastically with thermal cycles.
- Thermal effects are exacerbated if the critical displacement δ^* required to mobilize the pile-soil interface shear strength is small.
- Large-diameter piles are less susceptible to thermal effects due to the large critical displacement δ^* required to mobilize shaft and base capacities.
- The numerical algorithm does not account for soil thermal consolidation and changes in horizontal effective stress that may develop around the pile.

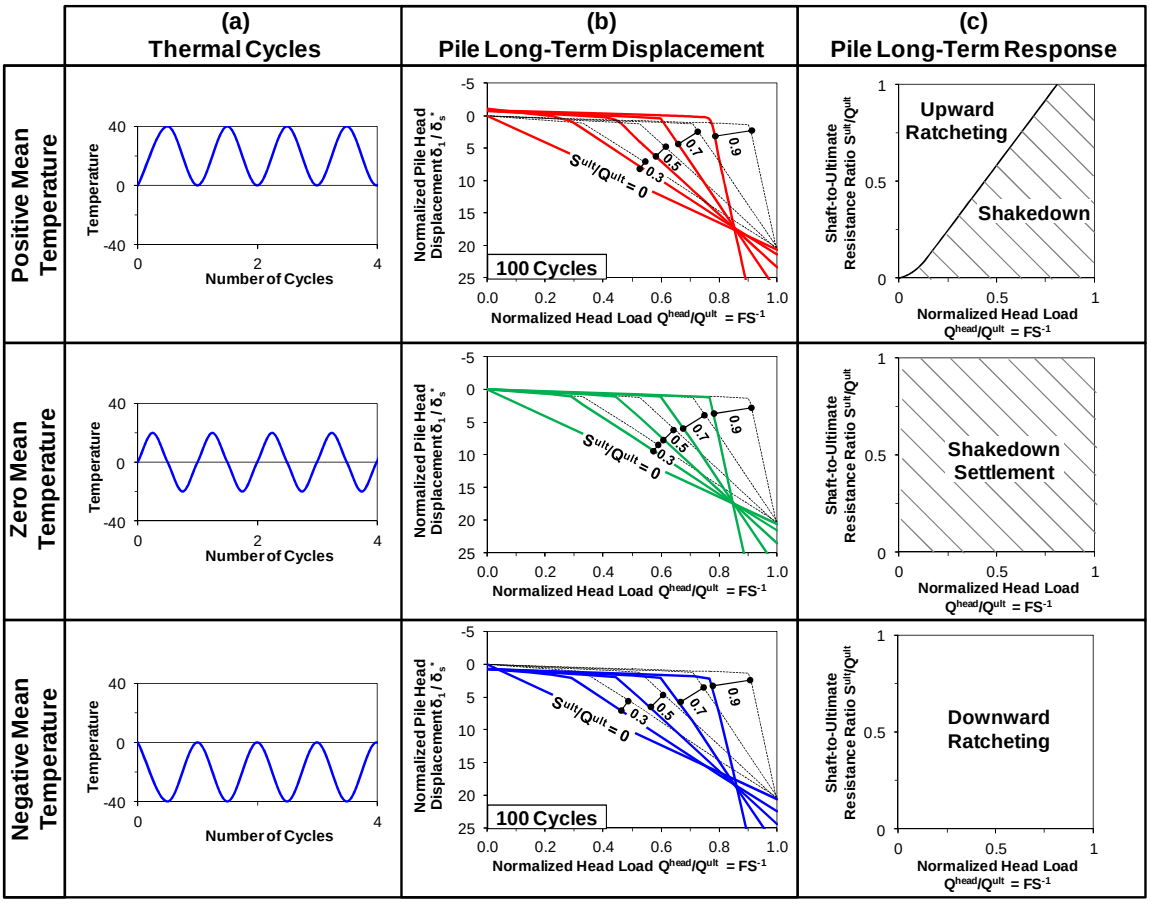

Figure 7.6 Long-term responses of energy piles subjected to thermal cycles. The temperature change amplitude is ΔT = 40°C and the ultimate pile capacity is Q^{ult} = 3,750 kN. Note: Pile parameters in Table 7.1.

7.4 Conclusions

Numerical results for the long-term response of energy piles subjected to thermal cycles show that thermally-induced pile displacements can result in the accumulation of plastic displacements with the number of thermal cycles. Cumulative plastic displacements approach shakedown conditions with asymptotic displacements that are proportional to the temperature change amplitude when the mean value of the thermal cycles is zero. On the other hand, thermal cycles with negative mean values cause

downward ratcheting displacement, while thermal cycles with positive mean values can cause either upward ratcheting or shakedown.

In cases prone to shakedown, the evolution of the pile head displacement during thermal cycles can be estimated using an exponential function in terms of the number of thermal cycles. Moreover, most of the thermally-induced plastic displacements accumulate in the first few cycles (typically less than 10 to 20 cycles for standard applications). Shaft-bearing piles develop larger settlements at higher number of cycles whereas end-bearing piles reach smaller asymptotic displacements at fewer thermal cycles. In the limit, an end-bearing pile without shaft resistance is not affected by thermal cycles.

CHAPTER 8

CONCLUSIONS AND RECOMMENDATIONS

The scope of this research included a detailed analysis of global energy demands due to population growth and improvements in quality of life, identification of geotechnical challenges in the implementation of energy geo-storage, and the development of analytical solutions and a stable numerical scheme to study the long-term response of geotechnical systems subjected to repetitive mechanical and thermal loading. Field examples analyzed in this thesis include compressed air energy storage; repetitive loading on wind turbine foundations; and thermally-induced ratcheting displacements of rock masses, geomembranes resting on slopes, and energy piles.

8.1 Conclusions

The most relevant conclusions of this thesis are presented separately for each study.

Energy and Quality of Life

- Future energy demands will reflect the coupling between energy consumption, quality of life, population growth, social inequality, and governments' energy-for-life efficiency. Following current trends, the global energy consumption will increase by 50 % by the year 2040 compared to the 2010 level.
- The impact of restricted population growth on energy consumption is not significant unless the five-year population growth rate is limited to 5% worldwide, which is the current population growth rate in the USA.
- Stimulating growth in the developing world to attain a minimum energy consumption rate per capita of 1 kW/person increases the global energy

consumption by only 7% above a status-quo scenario and has a profound effect on global quality of life.

- Energy consumption rates in excess of ~5 kW/person do not lead to higher quality of life. Limiting consumption to 3.7 kW/person would keep 2040 energy consumption at 2010 levels.

Energy-Geostorage – Analysis and Geomechanical Implications

- Energy geo-storage enhances both power generation/distribution and the use of renewable energy sources. Energy geo-storage must be considered as an integral component of a sustainable energy strategy.
- Compressed air and pumped hydro energy storage are suitable for large scale power systems since they have lower levelized annual costs for high discharge times compared to batteries, flywheels, and electric storage systems.
- A compressed air energy storage system uses less volume than an equivalent pumped hydro storage system due to the higher energy density of compressed air compared to that of elevated water under typical conditions.
- Thermal energy storage either as sensible or latent heat is recommended when the available surplus energy is heat. Under volume restrictions, latent heat systems are preferred because of their higher energy densities for a given temperature range.
- Energy geo-storage involve cyclic changes in effective stress, temperature (including freeze-thaw), and moisture that affect the long-term performance of geo-materials.

Modeling the Long-Term Behavior of Granular Materials

- The long-term behavior of geotechnical systems subjected to a large number of mechanical load cycles can be studied with a hybrid numerical scheme that

involves a mechanical constitutive model to analyze the static load and the first load cycle, and empirical strain accumulation functions to track the deformation accumulation during repetitive loading.

- The empirical strain accumulation functions predict volumetric and shear strain accumulation as a function of the plastic strain during the first load cycle, the obliquity and amplitude of the cyclic load, and the number of load cycles.
- The numerical scheme satisfies initial conditions and asymptotic trends of the strain evolution, such as terminal density and ratcheting.
- A shallow foundation subjected to vertical and horizontal static loads and repetitive vertical load experiences accumulation of vertical and horizontal displacements, and stress redistribution as the number of load cycles increases.
- A rigid foundation subjected to repetitive eccentric load experiences cumulative settlement and rotation. Both settlement and rotation are more pronounced as the factor of safety decreases and the cyclic load amplitude increases.

Thermally-Induced Wedging and Ratcheting Displacement

- Thermally-induced plastic displacement along joints can combine with wedging effects to cause the gradual accumulation of rock block displacements. Repeated heating and cooling cycles can cause block ratcheting displacement.
- Results from a one-dimensional analytical model shows the non-linear effect of relative wedge-to-block size and the importance of exposure time on the temperature required to cause permanent displacement.
- Most rock slope systems are likely to experience thermo-mechanical wedging and ratcheting displacement in environments with seasonal temperature fluctuations higher than $\Delta T = 20\ ^{o}C$. Dolomite rocks are more sensitive to this mechanism than granite and basaltic rocks because of their higher thermal diffusivity.

- Experimental results validate the analytical model, which can explain the ratcheting behavior observed at the Masada massif.

Thermally-Induced Geomembrane Ratcheting Displacement

- Thermally-induced displacements in exposed geomembranes resting on inclined planes and subjected to thermal cycles can result in the accumulation of downward ratcheting displacements.
- Ratcheting displacement is caused by the high thermal expansion of the membrane, the weight-induced biased shear displacement, and the elasto-plastic nature of the membrane-soil interface.
- Numerical results confirm that thermally-induced ratcheting displacement increases with the number of thermal cycles as the static factor of safety decreases and the ratio between the unconstrained thermal expansion of the geomembrane and the critical interface displacement increases.
- The application of the numerical algorithm to analyze the behavior of natural rock slopes subjected to thermal cycles shows that rock slabs are likely to experience downward ratcheting displacement for typical daily and seasonal temperature changes only if the inclination angle η is close to the critical value $\eta = \tan\varphi$.

Thermally-Induced Long-Term Displacement of Energy Piles

- Thermally-induced displacements in energy piles subjected to thermal changes can result in the accumulation of plastic displacements with the number of thermal cycles.
- Cumulative plastic displacements approach asymptotic values that are proportional to the temperature change amplitude if the mean value of the thermal cycles is zero.

- Thermal cycles with negative mean values cause downward ratcheting displacement, while thermal cycles with positive mean values can cause either upward ratcheting or shakedown under typical operational loads.
- Shaft-bearing piles develop larger settlements at higher number of cycles whereas end-bearing piles reach smaller asymptotic displacements at fewer thermal cycles.
- In cases prone to shakedown, the evolution of the pile head displacement during thermal cycles can be estimated using an exponential function in terms of the number of thermal cycles.
- Most of the thermally-induced plastic displacements accumulate in the first few cycles (typically less than 10 to 20 cycles for standard applications).

8.2 Recommendations for Future Work

Research documented in this thesis can be readily extended to address other important related issues and phenomena. Salient pending questions and studies follow:

- Consider disaggregated quality-of-life-related data to quantify the impact of inequality reduction on quality of life improvements.
- Include propagation of uncertainties in energy consumption scenarios.
- Quantify the impact of energy geo-systems on global quality of life.
- Investigate distributed energy geo-storage systems (e.g., compressed air in foundations).
- Determine terminal density as a function of variables, such as mean stress, cyclic stress amplitude, and initial void ratio.
- Study bearing capacity changes after repetitive loading.
- Determine the magnitude of critical displacement to mobilize the ultimate interface resistance (e.g., jointed rocks, membrane-soil interface, and pile-soil interface), considering interface strength mobilization as a progressive failure mechanism.

- Consider three-dimensional effects on thermally-induced wedging using numerical tools, such as the distinct element method and block theory.
- Study thermo-mechanical amplification due to serial thermally-induced wedging.
- Incorporate wrinkle formation, tensile failure, and equivalent stiffness for large deformations in the study of geomembranes resting on slopes subjected to thermal changes;
- Consider soil consolidation and changes in horizontal stress in the long-term behavior of energy piles subjected to thermal cycles.

REFERENCES

Abuel-Naga, H. M., Bergado, D. T., and Bouazza, A. (2007). "Thermally induced volume change and excess pore water pressure of soft Bangkok clay." *Engineering Geology*, 89(1-2), 144 -154.

Albrecht, B. A., and Benson, C. H. (2001). "Effect of desiccation on compacted natural clays." *Journal of Geotechnical and Geoenvironmental Engineering*, 127(1), 67-75.

Allen, R. D., Doherty, T. J., Erikson, R. L., and Wiles, L. E. (1983). "Factors affecting storage of compressed air in porous-rock reservoirs." *PNL-4707*, Pacific Northwest Laboratory, Richland, WA.

Allen, R. D., Doherty, T. J., and Fossum, A. F. (1982a). "Geotechnical issues and guidelines for storage of compressed air in excavated hard rock caverns." *PNL-4180*, Pacific Northwest Laboratory, Richland, WA.

Allen, R. D., Doherty, T. J., and Kannberg, L. D. (1985). "Summary of selected compressed air energy storage studies." *PNL-5091*, Pacific Northwest Laboratory, Richland, WA.

Allen, R. D., Doherty, T. J., and Thoms, R. L. (1982b). "Geotechnical factors and guidelines for storage of compressed air in solution-mined salt cavities." *PNL-4242*, Pacific Northwest Laboratory, Richland, WA.

Alonso-Marroquin, F., and Herrmann, H. J. (2004). "Ratcheting of granular materials." *Physical Review Letters*, 92(5), 054301-1.

Amatya, B. L., Soga, K., Bourne-Webb, P. J., Amis, T., and Laloui, L. (2012). "Thermo-mechanical behaviour of energy piles." *Géotechnique*, 62(6), 503-519.

Arent, D. J., Wise, A., and Gelman, R. (2011). "The status and prospects of renewable energy for combating global warming." *Energy Economics*, 33(4), 584-593.

Bandis, S. C., Lumsden, A. C., and Barton, N. R. (1983). "Fundamentals of rock joint deformation." *Int. J. Rock Mech. Min.*, 20(6), 249-268.

Barksdale, R. D. (1972). "Laboratory evaluation of rutting in basecourse materials." Third International Conference on Structural Design of Asphalt Pavements, London, England, 161-174.

Barro, R., and Lee, J.-W. (2010). "A New Data Set of Educational Attainment in the World, 1950-2010." National Bureau of Economic Research.

Barton, N., and Choubey, V. (1977). "The shear strength of rock joints in theory and practice." *Rock Mech. Rock Eng.*, 10(1), 1-54.

Bary, A., Crotogino, F., Prevedel, B., Berger, H., Brown, K., Frantz, J., Sawyer, W., Henzell, M., Mohmeyer, K., and Ren, N. (2002). "Storing natural gas underground." *Oilfield Review*, 14(2), 2-17.

Beckwith, and Associates. (1983). "Review of environmental studies and issues on compressed air energy storage." *PNL-4460*, Pacific Northwest Laboratory, Richland, WA.

Bentley, R. W., Mannan, S. A., and Wheeler, S. J. (2007). "Assessing the date of the global oil peak: The need to use 2P reserves." *Energy Policy*, 35(12), 6364-6382.

Bérest, P., and Brouard, B. (2003). "Safety of salt caverns used for underground storage blow out; mechanical instability; seepage; cavern abandonment " *Oil & Gas Science and Technology - Rev. IFP*, 58(3), 361-384.

Bérest, P., Brouard, B., Karimi-Jafari, M., and Van Sambeek, L. (2007). "Transient behavior of salt caverns - Interpretation of mechanical integrity tests." *International Journal of Rock Mechanics and Mining Sciences*, 44(5), 767-786.

Blight, G. E. (1987). "Measurements on full size silos part 1: Temperatures and strains." *Bulk Solids Handling*, 7(6), 781-786.

Boardman, B. T., and Daniel, D. E. (1996). "Hydraulic conductivity of desiccated geosynthetic clay liners." *Journal of Geotechnical Engineering*, 122(3), 204-208.

Borja, R. I., and Lee, S. R. (1990). "Cam-Clay plasticity, Part 1: Implicit integration of elasto-plastic constitutive relations." *Computer Methods in Applied Mechanics and Engineering*, 78(1), 49-72.

Bouckovalas, G., Whitman, R. V., and Marr, W. A. (1984). "Permanent displacement of sand with cyclic loading." *Journal of geotechnical engineering*, 110(11), 1606-1623.

Bourne-Webb, P. J., Amatya, B., and Soga, K. (2012). "A framework for understanding energy pile behaviour." *Proceedings of the ICE - Geotechnical Engineering*.

Bourne-Webb, P. J., Amatya, B., Soga, K., Amis, T., Davidson, C., and Payne, P. (2009). "Energy pile test at Lambeth College, London: geotechnical and thermodynamic aspects of pile response to heat cycles." *Géotechnique*, 59(3), 237-248.

Bradbury, K. (2010). "Energy storage technology review." Duke University, Durham, N.C.

Brandl, H. (2006). "Energy foundations and other thermo-active ground structures." *Geotechnique*, 56(2), 81-122.

Brown, S. F. (1974). "Repeated load testing of a granular material." *Journal of the Geotechnical Engineering Division, ASCE*, 100(GT7), 825-841.

Bullough, C., Gatzen, C., Jakiel, C., Koller, M., Nowi, A., and Zunft, S. (2004). "Advanced adiabatic compressed air energy storage for the integration of wind energy." European Wind Energy Conference, EWEC 2004, 22-25 November 2004, London, U.K.

Byrne, B. W., and Houlsby, G. T. "Assessing novel foundation options for offshore wind turbines." *World Maritime Technology Conference, London*.

Campanella, R. G., and Mitchell, J. K. (1968). "Influence of temperature variations on soil behavior." *American Society of Civil Engineers Proceedings, Journal of the Soil Mechanics and Foundations Division*, 94(SM3), 709-734.

Carslaw, H. S., and Jaeger, J. C. (1986). *Conduction of Heat in Solids*, Oxford University Press, New York, NY.

Carson, J. W. (2000). "Silo failures: Case histories and lessons learned " Third Israeli Conference for Conveying and Handling of Particulate Solids, Dead Sea, Israel.

Carson, J. W., and Holmes, T. (2003). "Silo failures: Why do they happen?" *TASK Quarterly*, 7(4), 499-512.

Cavallo, A. (2007). "Controllable and affordable utility-scale electricity from intermittent wind resources and compressed air energy storage (CAES)." *Energy*, 32(2), 120-127.

Cengel, Y. A., and Boles, M. A. (2001). *Thermodynamics: An engineering approach*, McGraw-Hill, New York.

Chadbourn, B. A., Luoma, J. A., Newcomb, D. E., and Voller, V. R. (1996). "Consideration of hot-mix asphalt thermal properties during compaction." Quality Management of Hot-Mix Asphalt, ASTM STP 1299, D. S. Decker, ed., American Society for Testing and Materials.

Chan, K. S., Bodner, S. R., and Munson, D. E. (2000). "Application of isochronous healing curves in predicting damage evolution in a salt structure." *International Journal of Damage Mechanics*, 9(2), 130 - 153.

Chang, C. S., and Whitman, R. V. (1988). "Drained permanent deformation of sand due to cyclic loading." *Journal of geotechnical engineering*, 114(10), 1164-1180.

Chappel, M. (2012). "A field scale evaluation of wrinkles in exposed HDPE geomembranes," Queen's University, Kingston, Ontario.

Chappel, M. J., Take, W. A., Brachman, R. W. I., and Rowe, R. K. (2008). "A case study of wrinkles in a textured HDPE geomembrane on a slope." The First Pan American Geosynthetics Conference & Exhibition, Cancun, Mexico.

Chen, K., Cole, J., Conger, C., Draskovic, J., Lohr, M., Klein, K., Scheidemantel, T., and Schiffer, P. (2006). "Granular materials: Packing grains by thermal cycling." *Nature*, 442(7100), 257-257.

CIA. (2011). "The world factbook." Central Intelligence Agency, McLean, Virginia.

Clauser, C., and Huenges, E. (1995). "Thermal conductivity of rocks and minerals." Rock Physics and Phase Relations: A Handbook of Physical Constants, T. J. Ahrens, ed., American Geophysical Union, 105-126.

Colgan, J. D. (2010). "Oil and Revolutionary Governments: Fuel for International Conflict." *International Organization*, 64(4), 661-694.

Coyle, H. M., and Reese, L. C. (1966). "Load transfer for axially loaded piles in clay." *Journal of Soil Mechanics & Foundations Div*, 92(2), 1-26.

Crotogino, F., Mohmeyer, K. U., and Scharf, R. (2001). "Huntorf CAES: More than 20 years of successful operation." Solution Mining Research Institute Meeting 23–25 April, Orlando, FL.

Dafalias, Y. F., and Herrmann, L. R. (1986). "Bounding Surface Plasticity. II: Application to Isotropic Cohesive Soils." *Journal of Engineering Mechanics*, 112(12), 1263-1291.

Davies, M. C. R., Hamza, O., and Harris, C. (2001). "The effect of rise in mean annual temperature on the stability of rock slopes containing ice-filled discontinuities." *Permafrost Periglac.*, 12(1), 137-144.

Deane, J. P., Ó Gallachóir, B. P., and McKeogh, E. J. (2010). "Techno-economic review of existing and new pumped hydro energy storage plant." *Renewable and Sustainable Energy Reviews*, 14(4), 1293-1302.

Demars, K. R., and Charles, R. D. (1982). "Soil volume changes induced by temperature cycling." *Canadian Geotechnical Journal*, 19(2), 188-194.

Denholm, P., and Margolis, R. M. (2007). "Evaluating the limits of solar photovoltaics (PV) in traditional electric power systems." *Energy Policy*, 35(5), 2852-2861.

Dincer, I., and Rosen, M. A. (2011). *Thermal energy storage - Systems and applications*, John Wiley & Sons Ltd, Chichester, West Sussex, U.K.

Diyaljee, V. A., and Raymond, G. P. (1982). "Repetitive load deformation of cohesionless soil." *Journal of the Geotechnical Engineering Division, ASCE*, 108(GT10), 1215-1229.

DM. (2011). "Household electrification rate." DataMarket, Iceland.

Dobry, R., and Swiger, W. F. (1979). "Threshold strain and cyclic behavior of cohesionless soils." Third ASCE/EMDE Specialty Conference, 17-19 September, Austin, TX, 521-525.

Drbal, L. F., Boston, P. G., Westra, K. L., and Erickson, R. B. (1996). *Power plant engineering by Black & Veatch*, Springer Science+Business Media, Inc, New York, N.Y.

EIA. (2010). "International Energy Outlook 2010." U.S. Energy Information Administration, Washington, DC.

EIA. (2011). "Population." Population. http://www.eia.gov/cfapps/ipdbproject. U.S. Energy Information Administration.

Eigenbrod, K. D. (1996). "Effects of cyclic freezing and thawing on volume changes and permeabilities of soft fine-grained soils." *Canadian Geotechnical Journal*, 33(4), 529-537.

EIU. (2007). "The Economist Intelligence Unit's quality-of-life index." *The Economist Intelligence Unit's quality-of-life index. The Economist*.

El-Dessouky, H., and Al-Juwayhel, F. (1997). "Effectiveness of a thermal energy storage system using phase-change materials." *Energy Conversion and Management*, 38(6), 601-617.

Elvidge, C. D., Baugh, K. E., Sutton, P. C., Bhaduri, B., Tuttle, B. T., Ghosh, T., Ziskin, D., and Erwin, E. H. (2011). "Who's in the Dark—Satellite Based Estimates of Electrification Rates." Urban Remote Sensing: Monitoring, Synthesis, and Modeling in the Urban Environment, John Wiley & Sons, Ltd, 211-224.

EPA. (2009). "Municipal solid waste generation, recycling, and disposal in the United States: Facts and figures for 2008." *EPA-530-F-009-021*, United States Environmental Protection Agency, Washington, DC.

EPRI-DOE. (2003). "EPRI-DOE Handbook of energy storage for transmission and distribution applications." EPRI, Palo Alto, CA, and the U.S. Department of Energy, Washington, D.C.

EPRI-DOE. (2004). "Energy storage for grid connected wind generation applications." EPRI, Palo Alto, CA, and the U.S. Department of Energy, Washington, D.C.

Farid, M. M., Khudhair, A. M., Razack, S. A. K., and Al-Hallaj, S. (2004). "A review on phase change energy storage: materials and applications." *Energy Conversion and Management*, 45(9-10), 1597-1615.

Farulla, C. A., Ferrari, A., and Romero, E. (2007). "Mechanical behaviour of compacted scaly clay during cyclic controlled-suction testing." Experimental Unsaturated Soil Mechanics, T. Shanz, ed., 345-354.

Fortner, B. (2008). "Air compressed with wind power to provide energy in Iowa." *Civil Engineering*, 78(1), 34-35.

Fossan, N. E. V. (1979). "Mechanisms of product leakage from solution caverns." Fifth International Sysmposium on Salt, Hamburg, Germany, 213-230.

François, S., Karg, C., Haegeman, W., and Degrande, G. (2010). "A numerical model for foundation settlements due to deformation accumulation in granular soils under repeated small amplitude dynamic loading." *International Journal for Numerical and Analytical Methods in Geomechanics*, 34(3), 273-296.

Franklin, J. A., and Dusseault, M. B. (1989). *Rock Engineering*, McGraw-Hill, New York, NY.

Fuenkajorn, K. (2006). "Healing of fractures in rock salt." *Suranaree Journal of Science and Technology*, 13(4), 307-316.

Fuenkajorn, K., and Phueakphum, D. (2010). "Effects of cyclic loading on mechanical properties of Maha Sarakham salt." *Engineering Geology*, 112(1-4), 43-52.

Gajo, A., and Muir Wood, D. (1999). "Severn-Trent sand: A kinematic-hardening constitutive model: The q-p formulation." *Geotechnique*, 49(5), 595-614.

Garcia-Rojo, R., and Herrmann, H. J. (2005). "Shakedown of unbound granular material." *Granular Matter*, 7(2-3), 109-118.

Garg, H. P., Mullick, S. C., and Bhargava, A. K. (1985). *Solar thermal energy storage*, D. Reidel Publishing Company, Dordrecht, Holland.

Gidel, G., Hornych, P., Chauvin, J. J., Breysse, D., and Denis, A. (2001). "A new approach for investigating the permanent deformation behaviour of unbound granular material using the repeated load triaxial apparatus." *Bulletin des Laboratoires des Ponts et Chaussées*, 233(4), 5-21.

Giramonti, A. J., Lessard, R. D., Blecher, W. A., and Smith, E. B. (1978). "Conceptual design of compressed air energy storage electric power systems." *Applied Energy*, 4(4), 231-249.

Giroud, J. P., and Morel, N. (1992). "Analysis of geomembrane wrinkles." *Geotextiles and Geomembranes*, 11(3), 255-276.

Glamheden, R., and Lindblom, U. (2002). "Thermal and mechanical behaviour of refrigerated caverns in hard rock." *Tunnelling and Underground Space Technology*, 17(4), 341-353.

Glaser, A. (2011). "After Fukushima: Preparing for a More Uncertain Future of Nuclear Power." *The Electricity Journal*, 24(6), 27-35.

Goodman, R. E. (1989). *Introduction to Rock Mechanics*, Wiley, New York, NY.

Graham, J., and Au, V. C. S. (1985). "Effects of freeze-thaw and softening on a natural clay at low stresses." *Canadian Geotechnical Journal*, 22(1), 69-78.

Grøneng, G., Christiansen, H., Nilsen, B., and Blikra, L. (2011). "Meteorological effects on seasonal displacements of the Åknes rockslide, western Norway." *Landslides*, 8(1), 1-15.

Gruber, S., and Haeberli, W. (2007). "Permafrost in steep bedrock slopes and its temperature-related destabilization following climate change." *J. Geophys. Res.*, 112(F2), F02S18.

Gunzburger, Y., Merrien-Soukatchoff, V., and Guglielmi, Y. (2005). "Influence of daily surface temperature fluctuations on rock slope stability: case study of the Rochers de Valabres slope (France)." *Int. J. Rock Mech. Min.*, 42(3), 331-349.

Hadley, K. (1976). "The effect of cyclic stress on dilatancy: Another look." *Journal of Geophysical Research*, 81(14), 2471-2474.

Haimson, B. C. (1978). "Effect of cyclic loading on rock." Dynamic geotechnical testing: a symposium, ASTM Special Technical Publication, D. A. Tiedemann, ed., ASTM, Denver, CO, USA, 228-245.

Hall, C., Tharakan, P., Hallock, J., Cleveland, C., and Jefferson, M. (2003). "Hydrocarbons and the evolution of human culture." *Nature*, 426(6964), 318-322.

Handin, J. (1969). "On the Coulomb-Mohr failure criterion." *J. Geophys. Res.*, 74(22), 5343-5348.

Harper, T. R., Appel, G., Pendleton, M. W., Szymanski, J. S., and Taylor, R. K. (1979). "Swelling strain development in sedimentary rock in Northern New York." *International Journal of Rock Mechanics and Mining Sciences & Geomechanics Abstracts*, 16(5), 271-292.

Hatzor, Y. H. (2003). "Keyblock stability in seismically active rock slopes - Snake Path Cliff, Masada." *J. Geotech. Geoenviron.*, 129(8), 697-710.

Hatzor, Y. H., Arzi, A. A., Zaslavsky, Y., and Shapira, A. (2004). "Dynamic stability analysis of jointed rock slopes using the DDA method: King Herod's Palace, Masada, Israel." *Int. J. Rock Mech. Min.*, 41(5), 813-832.

Hatzor, Y. H., and Palchik, V. (1997). "The influence of grain size and porosity on crack initiation stress and critical flaw length in dolomites." *Int. J. Rock Mech. Min.*, 34(5), 805-816.

He, B., and Setterwall, F. (2002). "Technical grade paraffin waxes as phase change materials for cool thermal storage and cool storage systems capital cost estimation." *Energy Conversion and Management*, 43(13), 1709-1723.

Heiken, G. H., Vaniman, D. T., and French, B. M. (1991). *Lunar Sourcebook: A User's Guide to the Moon*, Cambridge University Press, New York, NY.

Hepbasli, A. (2004). "Ground-source heat pumps." Encyclopedia of Energy, J. C. Cutler, ed., Elsevier, New York, 97-106.

Herrera, M. C., Lizcano, A., and Santamarina, J. C. (2007). "Colombian volcanic ash soils." Characterization and engineering properties of natural soils, T. S. Tan, et al., ed., National University of Singapore, Singapore, 2385-2409.

Herring, H. (2006). "Energy efficiency — A critical view." *Energy*, 31(1), 10-20.

Heuze, F. E. (1983). "High-temperature mechanical, physical, and thermal properties of granitic rocks - A review." *International Journal of Rock Mechanics and Mining Sciences & Geomechanics Abstracts*, 20(1), 3-10.

Hinkebein, T., Bauer, S., Ehgartner, B., Linn, J., Neal, J., Todd, J., Kuhlman, P., Gniady, C., and Giles, H. (1995). "Gas intrusion into SPR caverns." Sandia National Laboratories, Albuquerque, N.M.

Hirayama, H. (1990). "Load-settlement analysis for bored piles using hyperbolic transfer functions." *Soils and Foundations*, 30(1), 55-64.

Höök, M., Sivertsson, A., and Aleklett, K. (2010). "Validity of the Fossil Fuel Production Outlooks in the IPCC Emission Scenarios." *Natural Resources Research*, 19(2), 63-81.

Ibrahim, H., Ilinca, A., and Perron, J. (2008). "Energy storage systems - Characteristics and comparisons." *Renewable and Sustainable Energy Reviews*, 12(5), 1221-1250.

IEA. (2009). "World Energy Outlook 2009." International Energy Agency, Paris.

IEA. (2010). "World energy outlook." International Energy Agency, Paris.

IPCC. (2007). "Climate Change 2007: Synthesis Report. Contribution of Working Groups I, II, and III to the Fourth Assessment Report of the Intergovernmental Panel on Climate Change." IPCC, Geneva, Switzerland.

Jaeger, J. C., Cook, N. G. W., and Zimmerman, R. W. (2007). *Fundamentals of Rock Mechanics*, Blackwell Publishing, Malden, MA.

Kaggwa, W. S., Booker, J. R., and Carter, J. P. (1991). "Residual Strains in Calcareous Sand due to Irregular Cyclic Loading." *Journal of geotechnical engineering*, 117(2), 201-218.

Katz, D. (1973). "Outlook for underground storage." Fourth International Symposium on Salt, Northern Ohio Geological Society, Houston, TX., 253 - 258.

Katz, D. L., and Lady, E. R. (1976). *Compressed air storage for electric power generation*, Ulrich's Books, Ann Arbor, MI.

Knellwolf, C., Peron, H., and Laloui, L. (2011). "Geotechnical analysis of heat exchanger piles." *Journal of Geotechnical and Geoenvironmental Engineering*, 137(10), 890-902.

Kobayashi, M., Kuriki, Y., Watanabe, K., Chen, Y., Kusuda, H., and Mabuchi, M. (2009). "Microcrack growth patterns in Westerly granite specimens subjected to uniaxial cyclic loading." *International Journal of the JCRM*, 5(2), 103-110.

Koiter, W. (1960). "General theorems for elastic-plastic solids." Progress in solid mechanics, I. N. Sneddon and R. Hill, eds., Amsterdam, The Netherlands, 167-221.

Lackenby, J. (2006). "Triaxial behaviour of the ballast and the role of confining pressure under cyclic loading," University of Wollongong.

Laloui, L., Nuth, M., and Vulliet, L. (2006). "Experimental and numerical investigations of the behaviour of a heat exchanger pile." *International Journal for Numerical and Analytical Methods in Geomechanics*, 30(8), 763-781.

Landsbaum, E. M., Dodds, W. S., and Stutzman, L. F. (1955). "Humidity of compressed air " *Industrial and Engineering Chemistry*, 47(1), 101-103.

Lapko, A., and Prusiel, J. (1997). "Stress analysis of silo wall subjected to grain pressure and thermal actions." *Engenharia Civil*, 6, 3-16.

Lee, R. (2011). "The Outlook for Population Growth." *Science*, 333(6042), 569-573.

Lekarp, F., and Dawson, A. (1998). "Modelling permanent deformation behaviour of unbound granular materials." *Construction and Building Materials*, 12(1), 9-18.

Lentz, R. W., and Baladi, G. Y. (1980). "Simplified procedure to characterize permanent strain in sand subjected to cyclic loading." International Symposium on Soils under Cyclic and Transient Loading, Swansea, 89-95.

Lentz, R. W., and Baladi, G. Y. (1981). "Constitutive equation for permanent strain of sand subjected to cyclic loading." *Transportation Research Record*, 50-54.

Leroueil, S., Tardif, J., Roy, M., La Rochelle, P., and Konrad, J. M. (1991). "Effects of frost on the mechanical behaviour of Champlain Sea clays." *Canadian Geotechnical Journal*, 28(5), 690-697.

Lide, D. R. (2010). *CRC Handbook of Chemistry and Physics*, CRC Press/Taylor and Francis, Boca Raton, FL.

Lin, L. C., and Benson, C. H. (2000). "Effect of wet-dry cycling on swelling and hydraulic conductivity of GCLs." *Journal of Geotechnical and Geoenvironmental Engineering*, 126(1), 40-49.

Machado, G., Schaeffer, R., and Worrell, E. (2001). "Energy and carbon embodied in the international trade of Brazil: an input-output approach." *Ecological Economics*, 39(3), 409-424.

Manbeck, H. B. (1984). "Predicting thermally induced pressures in grain bins." *Transactions of the American Society of Agricultural Engineers*, 27(2), 482-486.

Marr, W. A., and Christian, J. T. (1981). "Permanent displacements due to cyclic wave loading." *Journal of the Geotechnical Engineering Division*, 107(8), 1129-1149.

Marsal, R. J. (1967). "Large scale testing of rockfill materials." *J. Soil Mech. Found. Div.*, 93(2), 27-43.

Mason, J., Fthenakis, V., Zweibel, K., Hansen, T., and Nikolakakis, T. (2008). "Coupling PV and CAES power plants to transform intermittent PV electricity into a dispatchable electricity source." *Progress in Photovoltaics: Research and Applications*, 16(8), 649-668.

Masters, G. M., and Wiley, J. (2004). *Renewable and efficient electric power systems*, John Wiley & Sons, Inc., Hoboken, N.J.

Matsuoka, N. (2001). "Direct observation of frost wedging in alpine bedrock." *Earth Surf. Proc. Land.*, 26(6), 601-614.

McCartney, J. (2011). "Engineering performance of energy foundations." Pan-Am CGS Geotechnical Conference, Toronto, Canada.

McKay, C. P., Molaro, J. L., and Marinova, M. M. (2009). "High-frequency rock temperature data from hyper-arid desert environments in the Atacama and the Antarctic Dry Valleys and implications for rock weathering." *Geomorphology*, 110(3-4), 182-187.

McLarnon, F. R., and Cairns, E. J. (1989). "Energy storage." *Annual Review of Energy*, 14, 241-271.

Meadows, D. H., Randers, J., and Meadows, D. L. (2004). *Limits to Growth: The 30-Year Update*, Chelsea Green Publishing Company, White River Junction, VT.

Melan, E. (1938). "Zur plastizität des räumlichen kontinuums." *Ing. Arch.*, 9, 116-126.

Mróz, Z. (1967). "On the description of anisotropic workhardening." *Journal of the Mechanics and Physics of Solids*, 15(3), 163-175.

Muir Wood, D. (1990). *Soil behaviour and critical state soil mechanics*, Cambridge University Press, Cambridge [England] ; New York.

Munson, D. E., Chan, K. S., and Fossum, A. F. (1999). "Fracture and healing of rock salt related to salt caverns." Meeting paper Las Vegas, NV, April 14-16, 1999, Solution Mining Research Institute, Encinitas, CA.

Munson, D. E., and Myers, R. E. (2000). "Relative evaluation of storage cavern volume measurements." Solution Mining Research Institute, Encinitas, CA.

Musso, G., Romero Morales, E., Gens, A., and Castellanos, E. (2003). "The role of structure in the chemically induced deformations of FEBEX bentonite." *Applied Clay Science*, 23(1-4), 229-237.

Najjar, Y. S. H., and Jubeh, N. M. (2006). "Comparison of performance of compressed air energy storage plant with compressed air storage with humidification " *Proceedings of the Institution of Mechanical Engineers, Part A: Journal of Power and Energy*, 220(6), 581-588.

Narsilio, G. A., and Santamarina, J. C. (2008). "Terminal densities." *Geotechnique*, 58(8), 669-674.

Niemunis, A., Wichtmann, T., and Triantafyllidis, T. (2004). "Explicit accumulation model for cyclic loading." International Conference on Cyclic Behaviour of Soils and Liquefaction Phenomena, Bochum, Germany, 65-76.

Niemunis, A., Wichtmann, T., and Triantafyllidis, T. (2005). "A high-cycle accumulation model for sand." *Computers and Geotechnics*, 32(4), 245-63.

Novo, A. V., Bayon, J. R., Castro-Fresno, D., and Rodriguez-Hernandez, J. (2010). "Review of seasonal heat storage in large basins: Water tanks and gravel-water pits." *Applied Energy*, 87(2), 390-397.

Oldecop, L. A., and Alonso, E. E. (2007). "Theoretical investigation of the time-dependent behaviour of rockfill." *Géotechnique*, 57(3), 289-301.

Omer, A. M. (2008). "Ground-source heat pumps systems and applications." *Renewable and Sustainable Energy Reviews*, 12(2), 344-371.

Osipov, V. I., Bik, N. N., and Rumjantseva, N. A. (1987). "Cyclic swelling of clays." *Applied Clay Science*, 2(4), 363-374.

Pejon, O. J., and Zuquette, L. V. (2002). "Analysis of cyclic swelling of mudrocks." *Engineering Geology*, 67(1-2), 97-108.

Peters, G. P., and Hertwich, E. G. (2008). "CO2 Embodied in International Trade with Implications for Global Climate Policy." *Environmental Science & Technology*, 42(5), 1401-1407.

Poulos, H. G., and Davis, E. H. (1980). *Pile foundation analysis and design*, Wiley & Sons, New York.

Prost, G. L. (1988). "Jointing at rock contacts in cyclic loading." *International Journal of Rock Mechanics and Mining Sciences & Geomechanics Abstracts*, 25(5), 263-272.

Qi, J., Vermeer, P. A., and Cheng, G. (2006). "A review of the influence of freeze-thaw cycles on soil geotechnical properties." *Permafrost and Periglacial Processes*, 17(3), 245-252.

Reese, L. C. (1978). "Design and construction of drilled shafts." *Journal of the Geotechnical Engineering Division*, 104(1), 91-116.

REN21. (2011). "Renewables 2011 Global Status Report." Renewable Energy Policy Network for the 21st Century, Paris.

Resch, G., Held, A., Faber, T., Panzer, C., Toro, F., and Haas, R. (2008). "Potentials and prospects for renewable energies at global scale." *Energy Policy*, 36(11), 4048-4056.

Richardson, G. (2000). "Exposed geomembrane covers: Part 1 - Geomembrane stresses." *GFR Magazine*, 18(7).

Rowe, R. K. (2005). "Long-term performance of contaminant barrier systems." *Géotechnique*, 55(9), 631-678.

Rowe, R. K. (2011). "Short- and long-term leakage through composite liners. The 7th Arthur Casagrande Lecture." *Canadian Geotechnical Journal*, 49(2), 141-169.

Rowe, R. K., Yang, P., Chappel, M. J., Brachman, R. W. I., and Take, W. A. (2012). "Wrinkling of a geomembrane on a compacted clay liner on a slope." *Geotechnical Engineering Journal of the SEAGS & AGSSEA*, 43(3), 11-18.

Ryan, M. P., and Sammis, C. G. (1981). "The glass transition in basalt." *J. Geophys. Res.*, 86(B10), 9519-9535.

Sagy, A., Reches, Z. e., and Agnon, A. (2003). "Hierarchic three-dimensional structure and slip partitioning in the western Dead Sea pull-apart." *Tectonics*, 22(1), 1004.

Sanner, B., Karytsas, C., Mendrinos, D., and Rybach, L. (2003). "Current status of ground source heat pumps and underground thermal energy storage in Europe." *Geothermics*, 32(4-6), 579-588.

Santamarina, J. C., Klein, K. A., and Fam, M. A. (2001). *Soils and Waves*, John Wiley & Sons, New York.

Sawicki, A., and Swidzinski, W. (1989). "Mechanics of a sandy subsoil subjected to cyclic loadings." *International Journal for Numerical and Analytical Methods in Geomechanics*, 13(5), 511-529.

Sawicki, A., and Swidzinski, W. (1995). "Cyclic compaction of soils, grains and powders." *Powder Technology*, 85(2), 97-104.

Schoenung, S. M. (2001). "Characteristics and technologies for long- versus short-term energy storage: A study by the DOE Energy Storage Systems Program." *SAND2001-0765*, Sandia National Laboratories, Albuquerque, N.M.

Schoenung, S. M., and Eyer, J. (2008). "Benefit/cost framework for evaluating modular energy storage." *SAND2008-0978*, Sandia National Laboratories, Albuquerque, N.M.

Schoenung, S. M., and Hassenzahi, W. V. (2003). "Long- vs. short-term energy storage technologies analysis. A Life-Cycle Cost Study." *SAND2003-2783*, Sandia National Laboratories, Albuquerque, N.M.

Scholz, C. H., and Koczynski, T. A. (1979). "Dilatancy anisotropy and the response of rock to large cyclic loads." *Journal of Geophysical Research*, 84(B10), 5525-5534.

Sharma, A., Tyagi, V. V., Chen, C. R., and Buddhi, D. (2009). "Review on thermal energy storage with phase change materials and applications." *Renewable and Sustainable Energy Reviews*, 13(2), 318-345.

Sharp, R. W., and Booker, J. R. (1984). "Shakedown of pavements under moving surface loads." *Journal of Transportation Engineering*, 110(1), 1-14.

Simonsen, E., Janoo, V. C., and Isacsson, U. (2002). "Resilient properties of unbound road materials during seasonal frost conditions." *Journal of Cold Regions Engineering*, 16(1), 28-50.

Succar, S., and Williams, R. H. (2008). "Compressed air energy storage: Theory, resources, and applications for wind power." Princeton Environmental Institute, Princeton University, Princeton, N.J.

Suiker, A. S. J., and de Borst, R. (2003). "A numerical model for the cyclic deterioration of railway tracks." *International Journal for Numerical Methods in Engineering*, 57(4), 441-470.

Suiker, A. S. J., Selig, E. T., and Frenkel, R. (2005). "Static and cyclic triaxial testing of ballast and subballast." *Journal of Geotechnical and Geoenvironmental Engineering*, 131(6), 771-782.

Sweere, G. T. H. (1990). "Unbound granular bases for roads," Delft University of Technology.

Take, W., Watson, E., Brachman, R., and Rowe, R. (2012). "Thermal Expansion and Contraction of Geomembrane Liners Subjected to Solar Exposure and Backfilling." *Journal of Geotechnical and Geoenvironmental Engineering*, 0(ja), 430.

Take, W. A., Chappel, M. J., Brachman, R. W. I., and Rowe, R. K. (2007). "Quantifying geomembrane wrinkles using aerial photography and digital image processing." *Geosynthetics International*, 14(4), 219-227.

Tamppari, L. K., Bass, D., Cantor, B., Daubar, I., Dickinson, C., Fisher, D., Fujii, K., Gunnlauggson, H. P., Hudson, T. L., Kass, D., Kleinböhl, A., Komguem, L., Lemmon, M. T., Mellon, M., Moores, J., Pankine, A., Pathak, J., Searls, M., Seelos, F., Smith, M. D., Smrekar, S., Taylor, P., Holstein-Rathlou, C., Weng, W., Whiteway, J., and Wolff, M. (2010). "Phoenix and MRO coordinated atmospheric measurements." *J. Geophys. Res.*, 115, E00E17.

Ter-Gazarian, A. (1994). *Energy storage for power systems*, Institution of Engineering and Technology, London, U.K.

Tharp, T. M. (1987). "Conditions for crack propagation by frost wedging." *Geol. Soc. Am. Bull.*, 99(1), 94-102.

Thirumalai, K., and Demou, S. G. (1974). "Thermal expansion behavior of intact and thermally fractured mine rocks." *AIP Conference Proceedings*, 17(1), 60-71.

Thoms, R. L., and Gehle, R. M. (2000). "A brief history of salt cavern use." Eighth World Salt Symposium, The Hague, The Netherlands, 7-11.

Thoms, R. L., and Martinez, J. D. (1978). "Long-term stability criteria for compressed air energy storage caverns in salt domes." 1978 CAES Technology Symposium, Asilomar, CA, 369-383.

Tien, Y. M., Lee, D. H., and Juang, C. H. (1990). "Strain, pore pressure and fatigue characteristics of sandstone under various load conditions." *International Journal of Rock Mechanics and Mining Sciences & Geomechanics Abstracts*, 27(4), 283-289.

Towhata, I., Kuntiwattanaku, P., Seko, I., and Ohishi, K. (1993). "Volume change of clays induced by heating as observed in consolidation tests." *Soils and Foundations*, 33(4), 170-183.

Tripathy, S., and Subba Rao, K. S. (2009). "Cyclic swell-shrink behaviour of a compacted expansive soil." *Geotechnical and Geological Engineering*, 27(1), 89-103.

Tripathy, S., Subba Rao, K. S., and Fredlund, D. G. (2002). "Water content - void ratio swell-shrink paths of compacted expansive soils." *Canadian Geotechnical Journal*, 39(4), 938-959.

Tseng, K.-H., and Lytton, R. L. (1989). "Prediction of permanent deformation in flexible pavement materials." *Implication of Aggregates in the Design, Construction, and Performance of Flexible Pavements, ASTM* (STP 1016), 154-154.

Tullis, J., and Yund, R. A. (1977). "Experimental deformation of dry Westerly granite." *Journal of Geophysical Research*, 82(36), 5705-5718.

Turcotte, D. L., and Schubert, G. (2002). *Geodynamics*, Cambridge University Press, New York, NY.

Uddin, N., and Asce, M. (2003). "Preliminary design of an underground reservoir for pumped storage." *Geotechnical and Geological Engineering*, 21(4), 331-355.

UN. (2011a). "Gross National Income per Capita ", Gross National Income per Capita. http://hdr.undp.org/en/data/trends. Human Development Reports. The United Nations.

UN. (2011b). "Mean Years of Schooling (Adults Aged 25 Years and Above)." Mean Years of Schooling (Adults Aged 25 Years and Above). http://hdr.undp.org/en/data/trends. Human Development Reports. The United Nations.

UN. (2011c). "Proportion of the Population Using Improved Drinking Water Sources, Total." Proportion of the Population Using Improved Drinking Water Sources, Total. http://data.un.org. The United Nations.

UN. (2011d). "World population prospects, the 2010 revision." United Nations, Department of Economic and Social Affairs, New York.

UNDP. (2010). "Human Development Report 2010. 20th Anniversary Edition. The Real Wealth of Nations: Pathways to Human Development." United Nations Development Programme, New York.

USCB. (2011). "International data base." U.S. Census Bureau, Suitland, Maryland.

USDOE. (2004a). "Determining electric motor load and efficiency." U.S. Department of Energy.

USDOE. (2004b). *Fuel cell handbook*, U.S. Department of Energy, Morgantown, WV.

van der Linden, S. (2006). "Bulk energy storage potential in the USA, current developments and future prospects." *Energy*, 31(15), 3446-3457.

Viklander, P. (1998a). "Laboratory study of stone heave in till exposed to freezing and thawing." *Cold Regions Science and Technology*, 27(2), 141-152.

Viklander, P. (1998b). "Permeability and volume changes in till due to cyclic freeze/thaw." *Canadian Geotechnical Journal*, 35(3), 471-477.

Viklander, P., and Eigenbrod, D. (2000). "Stone movements and permeability changes in till caused by freezing and thawing." *Cold Regions Science and Technology*, 31(2), 151-162.

Vlcko, J., Greif, V., Grof, V., Jezny, M., Petro, L., and Brcek, M. (2009). "Rock displacement and thermal expansion study at historic heritage sites in Slovakia." *Environ. Geol.*, 58(8), 1727-1740.

Vosteen, H.-D., and Schellschmidt, R. (2003). "Influence of temperature on thermal conductivity, thermal capacity and thermal diffusivity for different types of rock." *Phys. Chem. Earth*, 28(9-11), 499-509.

Vucetic, M. (1994). "Cyclic threshold shear strains in soils." *Journal of Geotechnical Engineering*, 120(12), 2208-2228.

Vucetic, M., and Dobry, R. (1991). "Effect of soil plasticity on cyclic response." *Journal of Geotechnical Engineering*, 117(1), 89-107.

Wang, W., Chou, Y., and Lee, S. (1998). "Chemical stresses induced by grain-boundary diffusion." *Metallurgical and Materials Transactions A*, 29(8), 2121-2125.

Waples, D., and Waples, J. (2004). "A review and evaluation of specific heat capacities of rocks, minerals, and subsurface fluids. Part 1: Minerals and nonporous rocks." *Nat. Res. Res.*, 13(2), 97-122.

Watson, A. D., Moore, D. P., and Stewart, T. W. "Temperature influence on rock slope movements at Checkerboard Creek." *Ninth International Symposium on Landslides*, Rio de Janeiro, Brazil, 1293-1298.

WB. (2011a). "Gini Index." Gini Index. http://data.worldbank.org. The World Bank.

WB. (2011b). "IIASA/VID Projection: Mean Years of Schooling, Age 25+, Total." IIASA/VID Projection: Mean Years of Schooling, Age 25+. http://data.worldbank.org. The World Bank.

WB. (2011c). "Life Expectancy at Birth, Total (years)." Life Expectancy at Birth, Total. http://data.worldbank.org. The World Bank.

WB. (2011d). "Mortality Rate, Infant (per 1,000 Live Births)." Infant Mortality Rate. http://data.worldbank.org. The World Bank.

Wichtmann, T. (2005). "Explicit accumulation model for non-cohesive soils under cyclic loading," Ph.D. thesis, Ruhr Universitat Bochum, Bochum, Germany.

Wichtmann, T., Niemunis, A., and Triantafyllidis, T. (2006). "Experimental evidence of a unique flow rule of non-cohesive soils under high-cyclic loading." *Acta Geotechnica*, 1(1), 59-73.

Wichtmann, T., Rondon, H. A., Niemunis, A., Triantafyllidis, T., and Lizcano, A. (2009). "Prediction of permanent deformations in pavements using a high-cycle accumulation model." *Journal of Geotechnical and Geoenvironmental Engineering*.

Wierczeyko, E. (1983). "Determination of the Change in Shape and Volume of Salt Cavities During Storage Operation." Sixth International Symposium on Salt, Toronto, Canada, 65 - 68.

Wilkinson, R. G. (2006). "The impact of inequality." *Social Research: An International Quarterly*, 73(2), 711 - 732.

Williams, R. (2007). "Biofuels from municipal wastes - Background discussion paper." University of California at Davis and California Biomass Initiative.

Williams, R., Jenkins, B., and Nguyen, D. (2003). "Solid waste conversion: A review and database of current and emerging technologies.", California Integrated Waste Management Board. Interagency Agreement - IWM-C0172, Davis, CA.

Wong, T.-F. (1982). "Effects of temperature and pressure on failure and post-failure behavior of Westerly granite." *Mechanics of Materials*, 1(1), 3-17.

Xiao, J.-Q., Ding, D.-X., Jiang, F.-L., and Xu, G. (2010). "Fatigue damage variable and evolution of rock subjected to cyclic loading." *International Journal of Rock Mechanics and Mining Sciences*, 47(3), 461-468.

Yang, C.-J., and Jackson, R. B. (2011). "Opportunities and barriers to pumped-hydro energy storage in the United States." *Renewable and Sustainable Energy Reviews*, 15(1), 839-844.

Zalba, B., Marin, J., Cabeza, L., and Mehling, H. (2003). "Review on thermal energy storage with phase change: Materials, heat transfer analysis, and applications." *Applied Thermal Engineering*, 23(3), 251-283.

Zaloudek, F. R., and Reilly, R. W. (1982). "An assessment of second-generation compressed air energy storage concepts." *PNL-3978*, Pacific Northwest Laboratory, Richland, WA.

Zekkos, D. P. (2005). "Evaluation of static and dynamic properties of municipal solid waste," Ph.D. thesis, University of California, Berkeley, U.S.

Zhang, H. W., Heeres, O. M., Borst, R. d., and Schrefler, B. A. (2001). "Implicit integration of a generalized plasticity constitutive model for partially saturated soil." *Engineering Computations*, 18(2), 314-336.

Zoback, M., and Byerlee, J. (1975). "The effect of cyclic differential stress on dilatancy in Westerly Granite under uniaxial and triaxial conditions." *Journal of Geophysical Research*, 80(11), 1526-1530.